NOVEL SOUND ABSORBING MATERIALS MADE FROM ELASTOMERIC WASTE

COMPOUNDING AND STRUCTURING OF ELASTOMERIC WASTE CRUMB AND FIBERS WITH BINDERS INTO INNOVATIVE NOISE INSULATION MATERIALS

Naeem A. AL-HILO

Submitted for the degree of

Doctor of Philosophy

Faculty of Engineering and Informatics

Chemical Engineering Department

University of Bradford

2018

Abstract

Naeem Abdulmohsin Ismael Al-Hilo

Novel Sound Absorbing Materials Made From Elastomeric Waste

Compounding And Structuring Of Elastomeric Waste Crumb And Fibers With Binders Into Innovative Noise Insulation Materials

Keywords: Sustainable, Stratified structure, Waste multilayer, Elastomer vacuum, Bio binders, Laser signal, Sound absorption modeling

Elastomeric wastes plague our time, polluting our environment and requiring urgent upcycling solutions. This research contributes to this agenda using an important source of waste, car tyre shred fibre residue (TSFR). It is demonstrated how using binders, non-foaming (SBR) and foaming (PU), we can transform these TSFR into structured porous acoustic-thermal insulation materials, suitable as underlay, cavity wall and pipe insulation. These structures were fabricated in purpose designed moulds and characterised for their porosity, tortuosity, flow resistivity and density. Their acoustic absorption performance was measured using industrial standards and the measurement underpinned with the Johnson-Champoux-Allard (JCA) model. With the under-layer materials, thermal insulation was also measured.

The results were as follows: (i) 40%/60% SBR/TSFR was an optimal composition for the underlay with the addition of 15% w/w bumper crumb of size > 1mm enhancing both impact sound and thermal insulation, (ii) PU was found to

produce well performing wall cavity insulation, particularly when vacuum pressure was applied, allowing micro and macro pores to be formed; (iii) PU applied with controlled amount of water to control foaming CO_2 formation produced super-performing (compared with Armacell System B) stratified pipe cladding insulation, optimal at porosity stratification of 90%, 83%, and 70%; (iv) Very good agreement was observed with predictions using JCA model, allowing further research to be carried out with these now well characterised sound insulations.

In addition to the developing materials, a novel technique for measuring sound absorption of pipe cladding was developed that could replace the expensive standard using a reverberation chamber.

Acknowledgements

I would like to thank my supervisors, Prof. Hadj Benkreira and Dr. Amir Khan for their supervision and invaluable guidance provided to accomplish the project.

I would also like to express my deep thanks and appreciation to the Iraqi government represented by the Ministry of Higher Education and Scientific Research for their financial support and granting the opportunity to do my PhD at the University of Bradford.

Finally, I would like to thank my parents and whole my family for their never ending support, patience and prayers.

Naeem

Table of Contents

Table of Figures

List of Tables

List of nomenclature

α	Sound absorption coefficient
E_i	Incident energy
E_r	Reflected energy
E_α	Sound Energy
Z_c	Characteristic impedance
P_s	Acoustic pressure
U_s	Particle velocity
Z_s	Surface acoustic impedance
k_b	Wavenumber
ω	Angular frequency
D_s	Stiffness
C_s	Sound speed
C_p	Specific heat capacity
P_m	Medium density
R	Sound pressure reflection coefficient
M	Mass
ρ_b	Density of binder
r_n	Radius of rubber grain
ρ_{mix}	Density of the mixture
ρ_{gra}	Density of the granulate
Ω	Porosity
Ω_0	Porosity of the loose granular mixture
Q	Heat flux
λ	Thermal conductivity
a	Thermal diffusivity
α_∞	Tortuosity
σ	Flow resistivity
σ_e	Effective flow resistivity
f_r	Resonant frequency
TL_n	Octave band transmission loss
$\widetilde{\rho}$	Complex effective density
$\widetilde{K}$	Complex effective bulk modulus

Λ	Characteristic viscous length
C'	Pore shape
η	Air viscosity
Λ'	Thermal characteristic length

CHAPTER ONE

INTRODUCTION

1.1 Introduction

Since their discovery, elastomeric materials progressively turned their innovative merit into environmental issues with the irresponsible disposal of their end of use products. We are only too familiar with the deplorable sight of littered plastic waste and used tyres. Now, the elastomeric waste accumulation problem has become a global issue and there is an urgent issue to upcycle this waste; that use it as a raw material and turn it into useful products.

This is precisely the aim of this research-transform tyre shred fibre and rubber residue into advanced noise and thermal insulation material. By advanced, it is meant engineer material structures with designed porosity that can compete or even outperform current commercial noise and thermal insulation materials to be used in buildings (under-layer and cavity wall insulations), domestic goods, automotive and cladding of oil and gas pipelines. By doing so, this research will contribute to the world sustainability and environmental protection mission.

1.2 Elastomeric waste

Elastomeric waste is defined as the elastomeric remnant of products such as tyres, automotive dashboards, bumpers, upholstery and trims, rubber tiles and polymer-based carpet that cannot be recycled. Growing public concern for the

environment and increased landfill taxation have led to a huge stockpile of such waste, a potential raw material ready to be transformed into useful products. This abundant waste usually is processed into rubber crumb leaving behind an elastomeric residue (dust) made up of tiny rubber particles trapped with polymeric fibre (see Figure 1.1 and 1.2).

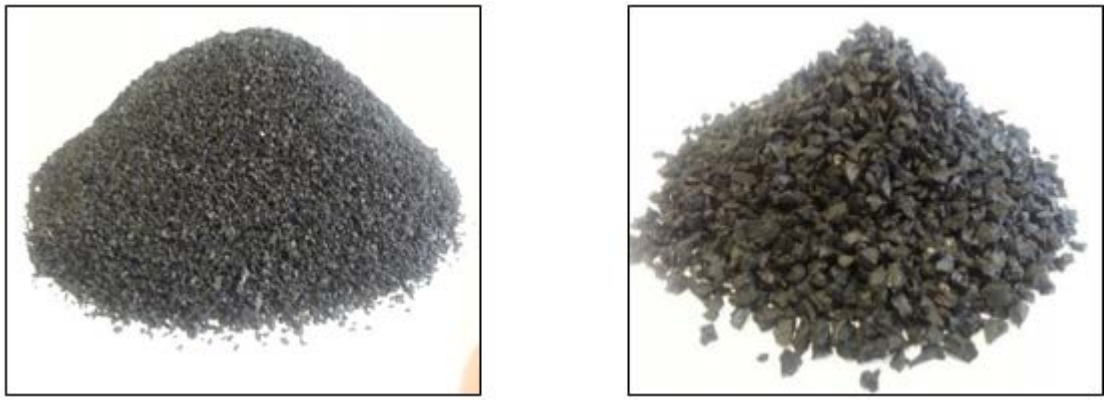

Figure 1.1. Tire and bumper crumb rubber.

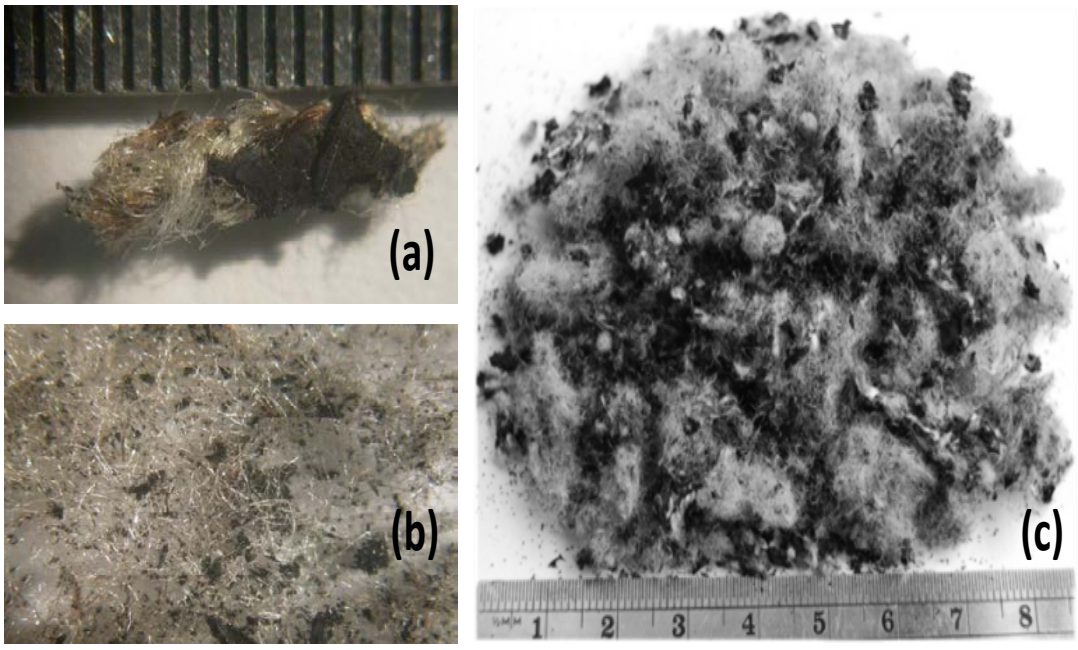

Figure 1.2. Tire share residue (rayon fibre).

This raw material is not only very cheap to purchase (a surplus of it naturally exists), it is often offered free to unburden companies forced to look into alternative uses for their waste output. This waste has become an international issue, sipping not only on land but also in the seas and requiring urgent attention. The annual global production of tyres is some 1.4 billion units, which corresponds to an estimated 17 million tonnes of used tyres each year (Sienkiewicz et al. 2012). In the U.K. alone, polymeric waste from manufacturing operations is estimated to be around 10.5 million m^3 or 70 Thousand tons per year (A. Khan 2007), the majority of which is land-filled and the remainder is incinerated. The situation is much the same in European countries of similar economic activity. In the USA, China, Russia and India with their larger usage of elastomers, the picture is worse. The numbers in Figure 1.3 show the extent of this waste problem In Europe countries.

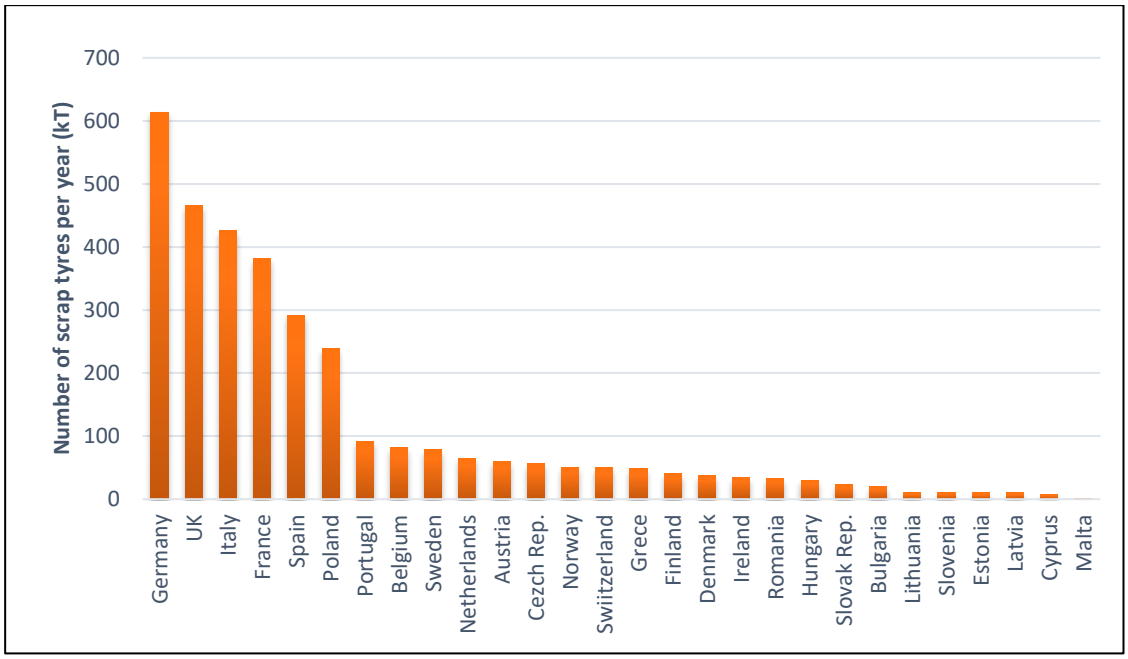

Figure 1.3. Number of scrap tyres in EU countries 2013 in thousands of tonnes.

With tougher environmental regulations and international commitments, there is increased incentive to use this waste as a raw material to compete with, if not replace, products traditionally made from virgin materials. This research fits precisely with this mission.

In this research, both rubber crumb and elastomeric residue are used as the base materials to develop acoustic and thermal insulation materials such as under-layer, cavity wall and pipe cladding insulations. It has been already shown that such rubber crumb and elastomeric residue can be successfully reused (see discussion in the literature review) to create porous materials with excellent vibroacoustic performance in noise control applications (Maderuelo-Sanz et al. 2012), (Jimenez-Espadafor et al. 2011), (Maderuelo-Sanz et al. 2011), (Maderuelo-Sanz et al. 2013), (Ghofrani et al. 2016), (Tiuc et al. 2016). This research aims to go a step further in this perspective by developing structures that have **stratified pore sizes** or **multi-size pores** (see Figure 1.4 and Figure 1.5) which are in principle conducive to superior acoustic performance. We shall explain why in the following chapter. In addition, these structures will be tested for their heat insulating property.

Figure 1.4. A cross-section of a stratified pore structure made in this research.

Figure 1.5. A cross-section of a multi-size- pore structure made in this research.

1.3 Aim and Objectives

As just explained, the main aim of this study is producing low-cost materials for vibroacoustic application by using scrap elastomeric products. To achieve this aim, rubber crumb and elastomeric residue will be compounded together with binders into structures that have either pores of stratified sizes or of multi-sizes so that the acoustic properties are enhanced in comparison with structures with (nearly) single size pores. To produce such tailored porous structure, experiment will be done with a series of fabrication strategies such as the application of vacuum, layering of the structure and the control of the particle size of the solid particulates and the binder foaming potential taking into consideration the results of previous work, both theoretical and experimental to guide us through the research. Thus the objectives of the research are as follows:

(1) A thorough review of prior experimental and theoretical research with direct relevance to the study.

(2) The development of experimental techniques to produce (i) stratified pores structures and (ii) multi-size pores structures for applications as under-layer, cavity wall and pipe cladding insulations.

(3) The measurement of the acoustic and thermal insulation properties of the samples produced using established methods but also improving on these if possible. These properties, porosity, tortuosity and flow resistivity are fundamental.

(4) The theoretical underpinning of the measurement made using established acoustic and thermal insulation models to check the accuracy of the measurements by comparing predicted and measured porosity, tortuosity

and flow resistivity but also to extract the important properties of viscous and thermal lengths.

(5) Finally, a related objective is that of developing a simple technique for measuring noise absorption of pipe cladding. Currently, the standard technique is expensive and involved the use of a reverberation chamber and a long pipeline.

The thesis presented here follows a classical format and is composed of this introductory chapter followed by a literature review of previous work, an experimental method chapter describing the various materials used, the structure fabrication and the measurement techniques, a result chapter detailing the data on the structures developed and their measured acoustic and thermal properties, a theoretical chapter underpinning the experimental findings and finally a conclusion chapter bringing together all the findings of the research and identifying further follow-on work.

CHAPTER TWO

LITERATURE REVIEW

2.1 Introduction

As the world becomes more populated, the need for sustainable noise reduction and control methods become ever more important to maintain individual comfort and quality of life. The problem of unwanted noise is increasingly becoming a source of complaint and of growing interest to all with responsibility for the built environment. Investigations reveal that poor sound insulation is the most commonly cited defect in houses(Langdon 1982). In a survey of the subjective response of the occupants of conversion flats, Oseland and Raw (1991) have found that noise from the flat above through the separating floor was particularly disturbing due to the component of impact noise and its unpredictable nature. The reduction of this type of noise is, therefore, an important part in alleviating a problem which has steadily increased over the last couple of decades.

Highly porous, fibrous materials play an important role in the control of sound. Such materials are used in a wide variety of forms and configurations for special purposes. Some fibrous materials such as glass fibres are synthetic and are spun together to form a flexible blanket while others appear as open-cell elastic foams. Others consist of natural fibres such as wool or hair felt. Most are available in a range of porosities and densities.

This chapter begins by explaining acoustic materials in general and some of the mechanisms of sound absorption. It points out that although there are acceptable alternatives to the use of recycled porous materials for vibro-acoustic

applications there is little-published information on their dynamic properties. The reasons for the development of porous materials from waste tyre shred residue (TSR) are summarised and the distinct interest in the use of TSR in this thesis is justified.

2.2 Principles of vibro-acoustic insulation

A sound wave is a longitudinal wave where particles of the medium are temporarily displaced in a direction parallel to energy traveling and then return to their original position. The vibration in a medium produces alternative waves of relatively dense and sparse particles which are termed as compression and rarefaction respectively. The resultant variation to normal ambient pressure is received by the ear and perceived as sound e.g. reducing sound level through a wall is caused by reflecting a part of a sound wave by the wall and absorbing another part (Diamant 1965). The reflecting sound wave occurs when the reflecting plane has a large area with respect to the sound wavelength and the wall is plain. The reflection occurs according to the optical laws, which means both incidence and reflecting angles are equal (see Figure 2.1).

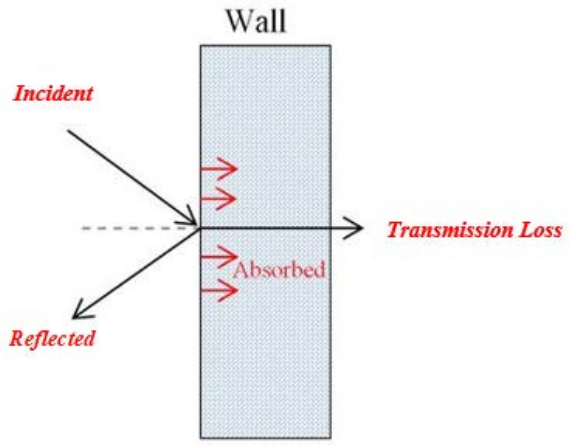

Figure 2.1. Diagram showing sound absorption and reflection.

Noise can be categorized into two main categories:

- Air-borne noise.
- Structure-borne noise.

Airborne sound travels through the air in the form of compressional pressure variations that are picked up by the ear and interpreted as sound whereas structure-borne noise travels through solid materials in the form of vibration that is later re-radiated as airborne sound at another location, (see Figure 2.2)

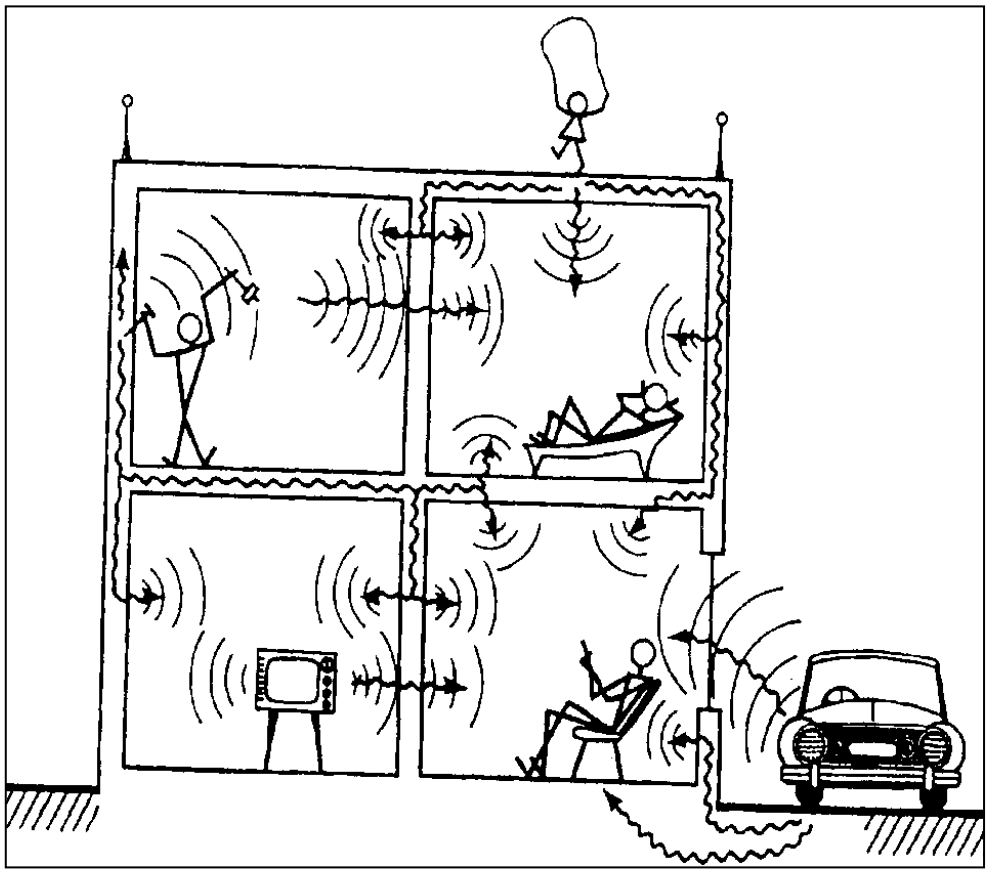

Figure 2.2. Illustration to demonstrate noise transmission mechanisms

A vast range of vibro-acoustic materials can be used to control both structure-borne and Air-borne noise. These materials can be split into four main categories:

- Sound Absorption (Absorbers)
- Sound Transmission Loss (Barriers)
- Vibration Isolation (De-Couplers - Isolators)
- Vibration Damping (Dampers**)**

Primarily, absorption and transmission loss (barrier) materials control air-borne noise whilst damping and isolation materials control structure-borne noise, as shown in Figure 2.3.

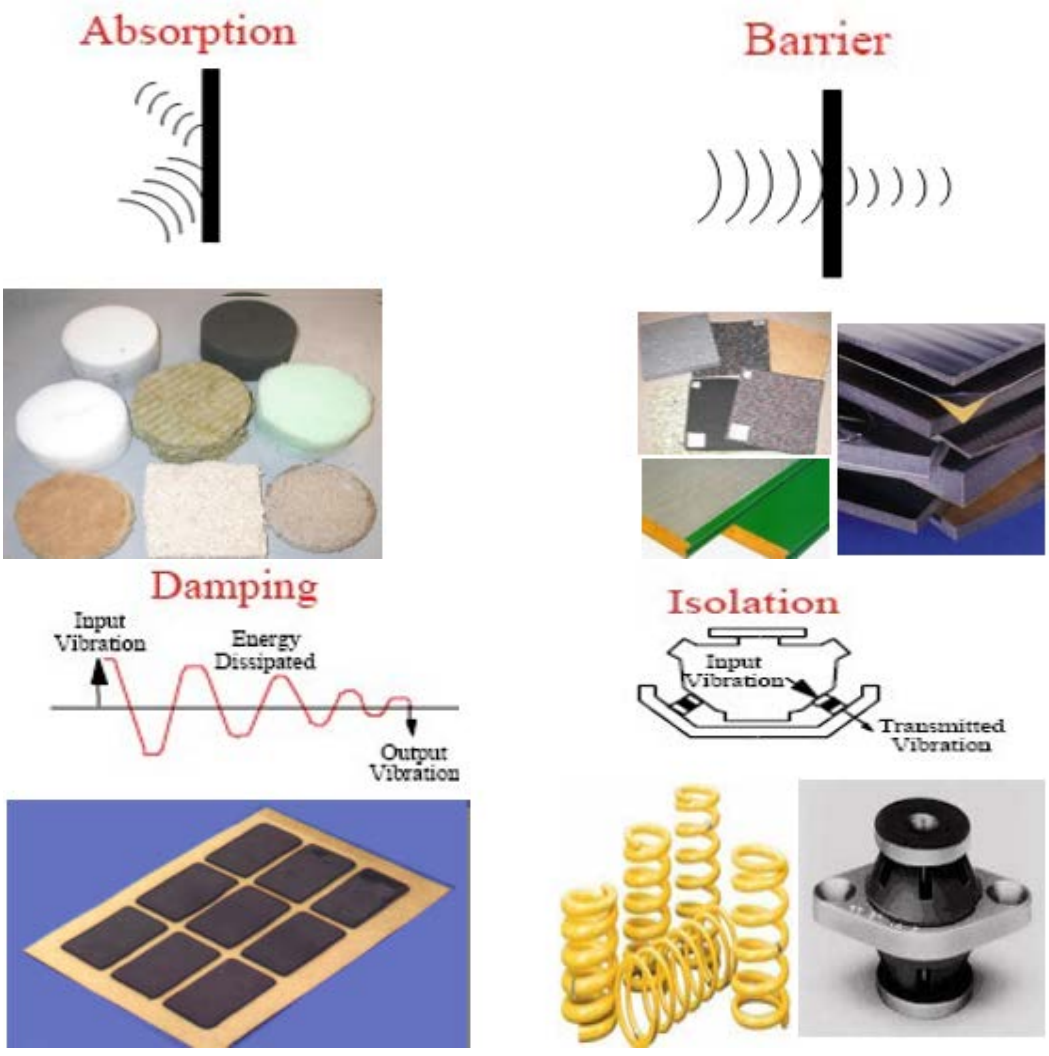

Figure 2.3. Various vibro-acoustic materials.

2.2.1 Absorption mechanism in porous materials.

Sound absorption is one of the fundamental properties of porous media. It is defined as the proportion of sound energy E_α which is absorbed or transmitted by the porous material when a sound wave with the energy E_i is incident on the material surface. So, the sound absorption coefficient is a real number given by the following ratio:

$$\alpha = \frac{E_\alpha}{E_i} = \frac{E_i - E_r}{E_i} \tag{2.1}$$

where; E_r is energy reflected from the material surface.

Another fundamental acoustic property of porous media is the characteristic impedance, which is defined as the ratio of the acoustic pressure (p_s) to the particle velocity (u_s) in a plane wave traveling in a bulk material, i.e.:

$$Z_c = \frac{p}{u} = \rho_b c_b \tag{2.2}$$

where; ρ_b is the bulk density of the medium and c_b is the sound speed.

In general, the sound speed and medium density can be complex in which case the characteristic impedance ($Z_c = Z_c^R + iZ_c^I$) can have the active (Z_c^I) (the real part), and reactive (Z_c^R) components (the imaginary part).

In the case when a sound wave is reflected by a layer of porous material, the surface acoustic impedance is used to denote the ratio of the acoustic pressure (p_s) to the particle velocity (u_s) at the layer interface:

$$Z_s = \frac{p_s}{u_s} \tag{2.3}$$

In a particular case, when a material layer of thickness *d* is placed against an acoustically rigid wall, the surface acoustic impedance is given by:

$$Z_s = \rho_b c_b \coth(-ik_b d) \tag{2.4}$$

where; $k_b = \frac{\omega}{c_b}$ is the wavenumber in the material and $\omega = 2\pi f$ is the angular frequency. This is a most practical method of acoustic porous media application.

The sound speed (c_s) is related to the bulk modulus (stiffness) (D_s) and the density of medium (ρ_m) as:

$$c_s = \sqrt{\frac{D_s}{\rho_m}} \tag{2.5}$$

The sound speed in air is affected by the temperature (T) and can be calculated as:

$$C_o = 332 + 0.6T \tag{2.6}$$

In the case when the sound waves propagate from medium 1 to medium 2, the following velocity continuity equation is observed:

$$\frac{P_i}{Z_{c1}} - \frac{P_r}{Z_{c1}} = \frac{P_\alpha}{Z_{c2}} \tag{2.7}$$

where; Z_{c1} and Z_{c2} are the characteristic impedance in medium 1 and medium 2 respectively. The sound pressure reflection coefficient R is the ratio of the sound pressure in the reflected wave to that of the incident wave so that:

$$|R|^2 = \frac{|P_r|^2}{|P_i|^2} = \left|\frac{Z_{c2} - Z_{c1}}{Z_{c2} + Z_{c1}}\right|^2 \tag{2.8}$$

In terms of the energy absorption coefficient:

$$\alpha = 1 - |R|^2 = 1 - \left|\frac{Z_{c2} - Z_{c1}}{Z_{c2} + Z_{c1}}\right|^2 \tag{2.9}$$

In the case when medium 1 is air and medium 2 is a semi-infinite layer of a porous material with surface impedance, the sound absorption coefficient is given by:

$$\alpha = 1 - \left|\frac{z_s - 1}{z_s + 1}\right|^2 \tag{2.10}$$

where; $z_s = \frac{Z_s}{\rho_c}$ is the normalised surface impedance of the semi-infinite absorber.

2.2.2 Recycling technology and recycled material properties

A majority of vibro-acoustic materials which are currently on the market are not recycled materials. These products are mainly developed from virgin raw resources such as oil, gas, and coal. Recycling process provides a cheap and

efficient method of creating materials with inherently good vibro-acoustic performance and high sustainability. This is mainly due to the fact that a considerable amount of industrial waste is granulated before being landfilled or incinerated. The granulation results in materials which are composed of loose and in many cases, micro-porous grains with a high proportion of open, interconnected pores (e.g. see Figure 2.4).

Figure 2.4. Microscopic photograph showing the porous structure of granulated, loose TSR.

These structures, if consolidated, can possess the acoustic absorption performance which is equal or even superior to existing (non-recycled) acoustic products. In many cases, the use of elastic binding agent results in materials with low elastic modulus and high values of damping which exhibit excellent vibration insulation performance.

There are four basic types of recycling technology: primary recycling, secondary recycling, tertiary recycling and quaternary recycling. These have been classified by Leidner (Leidner 1981). Primary recycling is when a scrap polymer waste product is manufactured through a standard processing method and the properties of the product are similar to the original raw material. Secondary recycling uses one or a combination of processing methods to generate the products having better performance than that observed in the original material. The primary recycling is mainly adopted by the industrial sector. However, the secondary recycling is used both by the industrial and consumer sectors. The chemicals and fuels are produced from the scrap waste of polymeric substances through the tertiary recycling process. The tertiary recycling of production of acrylics and thermosetting plastics are always accompanied by other chemicals in the industrial sector. Quaternary recycling is the process technology which relies upon the incineration for recovering energy from scrap polymer waste. This type of recycling is adopted when it is not possible to recycle material waste through any other method under normal circumstances.

2.3 Review of acoustical materials from recycled polymeric waste

In the past, there have been several attempts to develop acoustic materials from recycled granulated waste and the number of commercially available recycled materials for acoustic applications continue to increase. Some early attempts have been reported in the work by Vitamvasova et al (1996). These researchers developed a new range of recycled products from vulcanized

waste rubber crumb and vulcanized scraps of tyre production with textile or wire cord. Samples of these materials were prepared by adding a binder and compacting the mixture under heavy compaction pressure. As a result, new recycled media were produced with sound insulating properties up to 10 dB better than those found in commonly used building materials. These researchers noted in their paper that the same process can be used to develop materials for other applications including materials with low heat conductivity and with dynamic stiffness suitable for good impact sound insulation applications. Vitamvasova et al (1996) also found that the insertion loss of the recycled materials was more than 7 times better compared with that measured in some building materials at the high critical frequency. In the same research, another type of material was produced from a mixture of rubber, plastic crumb and wood fines with melted polymer crumb as the binder. The mechanical properties were shown to meet the requirement for application in building elements used for noise and vibration insulation. By adding synthetic fibres, another new type of material was produced. Comparing with special sound absorptive fibrous materials, the acoustical reduction factor of the recycled product was not as good as Itaver12 and Itaver24 in the medium and low-frequency range, however, the thickness of the recycled sample was 25% less than Itaver12 and Itaver24.

Pfretzschner and Rodriguez (1999) developed recycled rubber products from rubber crumb to form acoustic absorbent materials. The reutilized rubber was used in the pavement as modified asphalt to increase the elasticity, strength and noise reduction. Pfretzschner and Rodriguez (1999) studied the flow resistivity and the acoustic absorption coefficient as functions of the mean size of the rubber crumb in the granular mix. They found that the acoustic absorption

coefficient of the samples made from grains sizing around 1.4 - 3 mm can provide high values of the absorption coefficient comparable to that found in fibreglass. In another application, rubber crumb was used in the construction of noise barriers along highways and it had good performance in broadband acoustic absorption.

Comparison between unconsolidated rubber crumb and crumb consolidated with different size grains and material thickness were made by Swift (1998). To increase the durability and structural strength, a high acoustic absorption consolidated sample was produced. The studies show that the absorption of the adhesive material sample was affected by the grain sizes, binder quantity, and loading pressure. The rubber crumbs were granulated from car tyres of density 1050 kg/m^3. The grain size was in highly irregular shape and ranging from 0.35-5.00 mm. The assumption for the quantity of the polymer-based binder is based on the following equation:

$$M_b = M_r \frac{\rho_b}{\rho_r}[(1+\frac{x}{r_n})^3 - 1] \tag{2.11}$$

where; M_b and M_r are the mass, ρ_b, and ρ_r are the density of rubber crumb and binder, x is the thickness of material and r_n is the radius of rubber grain.

Swift et al. (1998) also showed that the pressure loading applied for compaction during the binding process can help to maximize the porosity without affecting significantly the overall strength and elasticity of the material. The acoustic performance of the produced material has been investigated using an impedance tube apparatus. It was shown that the acoustic absorption increases as the grain size decreases resulting in the higher values of the flow resistivity

Sobral and Samagaio (2003) investigated the elastic and acoustic absorption behavior of rubber granulates as a function of grain size, the chemical composition of rubber, curing temperature and the binder content. They presented their results in the form of stress-strain relations and frequency-dependent acoustic absorption coefficient which was determined for a range of material samples. The work showed that the best results for the flexural strength and acoustic absorption were obtained using finer rubber granulates sized 0.5-1.5 mm consolidated with 20% binder which contained 70:30 proportion of Vert Oxide resin and Buche-pore resin, respectively. Generally, the measured modulus of elasticity for the investigated samples was low and in the range of 140 – 500 kPa. The paper did not specify the thickness of the material samples used in the acoustic experiments.

The effect of consolidation on the acoustic properties of loose rubber granulates was investigated by Horoshenkov and Swift (2000). The results demonstrated that non-spherical granular mixtures in different states of consolidation could be produced to have a good degree of acoustic performance comparable to that found in some commercial absorbing materials. In this work, the non-acoustic parameters of the pore size distribution, porosity, tortuosity, and flow resistivity were related to the median grain size in the mix, the compaction ratio, and the binder content. The acoustic and related non-acoustic performance of materials made from four different grain sizes of 0.71-1.0, 1.0-1.4, 1.4-2.0 and above 2.0 mm had been investigated. These materials were consolidated in the form of a 20 mm thick porous plate. Samples of these plates were cut in order to measure median pore size, <*b*>, the standard deviation of the pore size, σ, flow resistivity, R_f, porosity, Ω, tortuosity, q, characteristic impedance, z_b, and surface

impedance, z_s, propagation constant, k_b, and the absorption coefficient, α. The median pore size and standard deviation of the consolidated sample were measured by the water suction method (Bies and Hansen, 2009). The porosity of loose granular mixes was calculated by:

$$\Omega_o = 1 - \frac{\rho_{mix}}{\rho_{gra}} \quad (2.12)$$

where; $\frac{\rho_{mix}}{\rho_{gra}}$ are the density of the mix and density of the granulate. The flow resistivity of loose and consolidated samples was measured by the method described by Allard (1993). The acoustic properties were measured using the impedance tube BK 4260 in the frequency range 100-6500 Hz. The experimental data were used to relate the porosity of the sample to the binder concentration and the compaction state for a sample of a constant thickness. The experimental results showed that the porosity reduces with increased compaction and is slightly affected by the particle size in the material. The observed porosity variation of these materials was less than 3%. It was proposed that the porosity of the consolidated samples for a constant binder concentration and variable compaction ratio can be predicted by the following formula:

$$\Omega_c = (\Omega_0 - v)(1 - v)^{-1} \quad (2.13)$$

where; Ω_o is the porosity of the loose granular mix, $v = \Delta V / V_0$, ΔV is the volume reduction of the sample due to compaction and V_o is the original volume of the sample without compaction.

This formula suggests that the porosity of consolidated granular material decreases by more than 50% of its original value when the compactions were greater than 40%. This data was also confirmed experimentally (Swift et al. 1999). The experimental results for the porosity at a fixed compaction ratio of 25% with variable binder concentration showed that the relationship between porosity and binder concentration is close to linear. The theoretical result can be predicted by:

$$\Omega_c = \Omega_0 - \beta X (1 - \Omega_0) \tag{2.14}$$

where; Ω_0 is the porosity of the loose mix in a chosen compaction ratio, $X = \frac{\rho_r}{\rho_b}$, $\beta = \frac{m_b}{m_r}$ (the binder concentration), and m_b and m_r are the masses of the binder and rubber granules in the sample.

In this research, Horoshenkov and Swift (2000) showed that the mean pore size is linked to the flow resistivity of the sample material. It is known that the flow resistivity is proportional to the internal surface area and inversely proportional to the square of the grain size. The result of this work demonstrated that the flow resistivity for a given median particle size increased almost linearly when the compaction ratio was greater than 15%. As a result, an empirical expression for the flow resistivity was derived and linked to the median grain size, g (mm), and compaction ratio, v:

$$\log_{10} R = 4.04 + 3.815(v - 0.15) - 1.399 \log_{10} g \tag{2.15}$$

where; $0.71 < g < 2.0$ mm ; $0.15 \le v \le 0.35$ and $\beta = 0.15$

This work also showed that the flow resistivity increases with the increase in binder concentration at constant compaction ratio. The following expression for the flow resistivity of a consolidated mixture with the grain size in the range 0-6 mm was proposed:

$$\log_{10} R = 3.074\beta + 3.794 \tag{2.16}$$

where; β is the mass binder concentration, $0 \leq \beta \leq 0.3$.

This experimental result suggests that the tortuosity of the loose grain mixes is independent of the mean grain size. The value of the tortuosity determines the high-frequency behavior of the characteristic impedance and propagation constant of a porous medium.

The normal incidence acoustic absorption coefficient was calculated from the following expression:

$$\alpha = 1 - \left| \frac{z_s - 1}{z_s + 1} \right|^2 \tag{2.17}$$

where; Z_s is the normalised acoustic surface impedance.

The acoustic absorption coefficient of smaller grain sizes (0.71 - 1.0mm) progressively reduced in the higher frequency range between 2000 and 6000 Hz. The results showed a slight reduction of the value of the absorption coefficient with the compaction ratio of 15% compared with that measured in the case of the loose grain mix. The binder concentration in this sample was fixed at 15%.

This difference in the absorption coefficient between the small grain mixtures increased with the increased compaction ratio. The effect of the compaction ratio is more complex in the case of the medium grain mixture (1.0-1.41 mm). The peak in the absorption coefficient for the medium grain mix with variable compaction ratio (15%, 25%, and 35%) occurred in the frequency range 2000-3000 Hz. The difference in the absorption coefficient between the compacted samples and loose mix increased as the compaction ratio increased in the medium frequency range of 1000-3000 Hz. In the higher frequency range of 3000-5000 Hz, this difference between the medium grain mixture and the corresponding loose mix is inversely proportional to the compaction ratio.

A similar behavior of the absorption coefficient for the large granular mixture (1.41 - 2.0 mm) was shown and compared against that for the medium granular mixture. However, a larger difference in the absorption coefficient between the compacted large sample and loose grain was found in the medium frequency range of 1000-3000 Hz. The results for the acoustic absorption coefficient for mixes with all grain sizes (< 6 mm) at a fixed compaction ratio (*CR* = 25%) and variable binder concentration were also obtained.

They showed the lower value of the absorption coefficient as the binder concentration increased. It was due to the reduction of the porosity and increasing in tortuosity values of the mixture. The result also showed a non-equal reduction in the absorption coefficient for a proportional increase in the binder concentration.

The real and imaginary parts of the surface impedance for the consolidated mixture with the grain size 0.71-1.0 mm were not affected

significantly when the compaction ratio was below 15%. The maximum of the real part of the surface impedance was shifted towards the lower frequency range and the value of the amplitude was reduced when the compaction ratio increased. For the consolidated mixture with a larger grain size of 1.0-1.4 mm, it showed that the real part of the surface impedance was not affected significantly for the compaction ratios above 25%. The maximum value of the real part of the surface impedance increased above 5000 Hz when the compaction ratio was below 15% in the case of the consolidated larger grain (1.0-1.4 mm) sample. The maximum value of the real part of the surface impedance of the large grain (1.41-2.0 mm) mixture increased and shifted toward to low-frequency range when the compaction ratio increased.

Horoshenkov and Swift (2001) have concluded that the acoustic properties of the consolidated mixture from rubber grains were affected by the particle range of the mixture, consolidated pressure (compaction ratio) and binder concentration. The porosity of the sample was reduced and the flow resistivity and tortuosity were increased as compaction ratio and binder concentration increased. The best acoustic performance was shown in the result of 0.71 - 2.0 mm mixture at 15% of compaction ratio.

The acoustic performance of natural fibres such as jute, wool, and cotton, synthetic fibres polyester and polypropylene was investigated by Seddeq et, al. (2013) in the frequency range 100 to 6300 Hz. Trials were carried out on mixes of fibres with agricultural wastes such as rice straw and sawdust, the results showed an improvement in insulation performance.

Moreover, it was found that adding an air space behind these systems improves the sound absorption coefficient for low and mid frequencies. Also, increasing insulation thickness improves sound insulation property over all the frequency range.

2.3.1 Acoustical materials from elastomeric waste

The abundance of scrap tyres has led many researchers to think about reusing them as a raw material to produce new products that are environmentally friendly, sustainable and low cost.

The fluff of scrap tyres has been used to produce sound insulation material and the product has been compared with some popular commercial sound insulation products by Maderuelo (2012). The results showed the new insulation material to have a better performance than that of most commercial insulation products. The process used to produce the insulation is dependent on high pressure with acrylic resin.

Tyre fluff has been used by Jimenez-Espadafor (2011), acoustical materials were produced by mixing the fluff with a hot melt adhesive. Best results were achieved by mixing 1:1 ratio of the fluff with hot molten adhesive and a 5 mm trituration mesh which produced a product with a density of 180 Kg/m^3.

Another kind of sound insulation material was produced using crumb rubber, urea-formaldehyde and polymeric methylene diphenyl diisocyanate (PMDI) as an adhesive by Zhao et al. (2010). They produced acoustic materials using this method that was better than many commercial materials such as wood-based particleboard and compound wooden floorboard. The parameter which

affected the performance of sound insulation was the amounts of crumb rubber and PMDI adhesive used.

Scrap tyre crumb rubber was used to produce another kind of sound insulation material as an underlay by Maderuelo-Sanz et al. (2011) and (2014). The results of these studies show that by using an airless gun with a special tip give better results than covering all the floor without the tip.

2.4 Thermal insulation materials

2.4.1 Introduction

Over the last two decades, fossil fuel prices have increased rapidly, which has led to increasing the operational cost of manufacturing processes, transportations and many other fields that consume fossil fuels. Houses and buildings can be considered as one of the largest consumers of energy for heating and cooling, a developed country like the USA consumes 40% of energy in buildings that are other than industry or transportation (Chen 2008). This consumption is not constant during the whole year, it could reach 42% in winter and maybe 29% in summer (Bond et al. 2013). Therefore, European countries have legislated a new regulation which considers a high standard of thermal protection for houses and buildings, this legislation was dependent on all European countries which set the required thermal conductivity values (U values) for building and houses to drop sharply (Turgut and Yesilata 2008). Clearly, developing effective thermal insulation, preferably cheaply and in a sustained manner is a desirable aim, hence the research in this area.

2.4.2 Thermal insulation properties

The basic parameter in material thermodynamics is the specific heat capacity (C_p). The heat capacity of a material is the amount of energy required to change the temperature of a body by 1°C. A unit of the heat capacity is J. K^{-1}. However, the specific heat capacity (C_p) is a more popular and practical characteristic. It is defined as the amount of energy required to change the temperature of 1kg body by 1°C, for which the unit is J. K^{-1} .kg^{-1}. The quantity of heat, Q in J, is determined by,

$$Q = mC_p\Delta T \tag{2.18}$$

where; m is the mass of the body (in the unit of *kg*), ΔT is the change in temperature (*K*).

The properties of heat conduction, i.e. the ability of materials to conduct heat, are determined by the thermal conductivity (λ), and thermal diffusivity (a). The heat flux (Q) is defined as the quantity of the heat flowing across a unit area per unit time ($J.m^{-2}.s^{-1}$). According to the Fourier's law,

$$\tilde{Q} = -\lambda\nabla T \tag{2.19}$$

where; ∇T is the temperature gradient.

The thermal diffusivity (a) is the rate of the heat flow through a medium. The equation defining the thermal diffusivity is

$$a = \frac{\lambda}{\rho C_p} \tag{2.20}$$

where; the ρ is the material density and C_p is the specific heat capacity.

Pores can be divided into three main types: closed pores, open pores, and partially connected pores. These three types of pores have a diverse effect on the materials acoustic absorption and thermal performance. The percentage of closed pores improve the thermal insulation, moreover, materials with a high percent of open pores contribute to the acoustic absorption performance. Whereas materials with partially closed pores are multifunctional materials and have good performance in terms of acoustic absorption and thermal insulation (see Figure 2.5). Hence, producing multifunctional materials with open and close pores will be one of the objectives of this study.

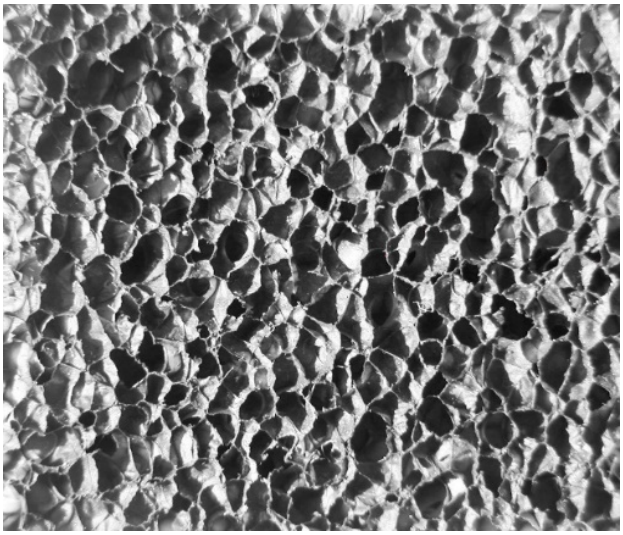

Figure 2.5 A microscopic picture of insulation materials with open and closed pores.

Thermal insulation materials were produced by Kymalainen and Sjoberg (2008) from natural resources. They used flax and hemp and investigated the effects of humidity causing mold, and the ability of microbial and other contaminants to grow inside this natural insulation.

The thermal effects of jute, flax, and hemp were investigated by Azra Korjenic et. al, (2011). They carried out a comparison study with commercial

fibrous insulation materials such as glass wool, Xianjun et.al. (2010) produced porous insulation material form rice straw. They used six different size of rice straw with two kinds of binders. They found rice straw particle size distribution to be the most important parameter for thermal insulation performance.

Sustainable insulation materials were produced by Xiao-yan Zhou et, al. (2010), by using a high-frequency hot press for pressing cotton stalk fibres without any chemical additives and binders. In this study, factors such as board density, moisture content and pressing time have been studied and the effects on thermal conductivity and mechanical properties of the insulation were investigated. One of the most important factors which has been studied is density, where boards with density of 150 Kg/m^3 – 450 Kg/m^3 has a linear relationship with thermal conductivity and the performance is between 0.0585 and 0.0815 W/m.K. There was no significant effect of moisture content and pressing time on thermal conductivity values.

Coal fly ash was used by Zhang et al. (2014) to produce a thermal insulation material by mixing it with 0.3 wt% foaming agent. The process used was foaming and slip casting method. They tested many variables such as solid loading wt %, different foaming agent additive levels, sample casting under different sintering temperatures between 850^oC and 1000^oC and the effect of both sintering temperature and solid loading on porosity to get the optimum properties.

The effects of crumb rubber on thermal conductivity was investigated by Joon Kye Lee and Julie Q. Shang (2013). They found that adding the tyre crumb rubber to mine tailings improved the thermal insulation performance.

An investigation into rubber particles as a filler with unsaturated polyester was carried out by Basim Abu-Judail (2016). It was found that insulation material

produced using the rubber filler had better performance than that without the rubber filler. Furthermore, the thermal conductivity of the insulation decrease with increasing the filler content as shown in Figure 2.6.

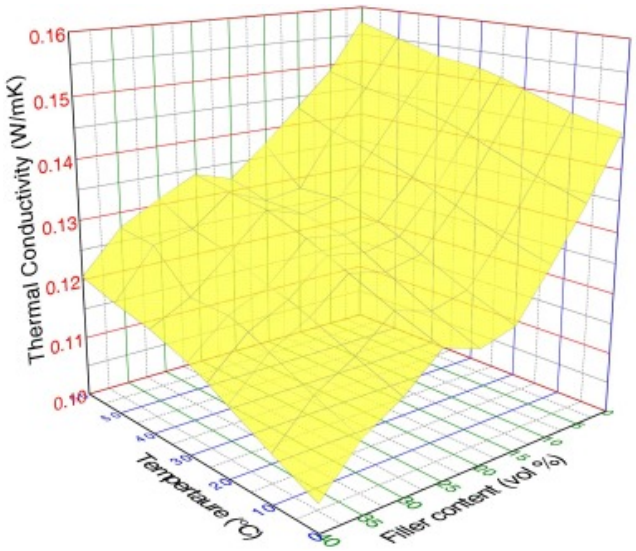

Figure 2.6. Surface plot linking thermal performance with filler content.

One of the main objectives of this research was to produce thermal insulation materials using elastomeric waste. One of the most important parameters which affects material's thermal performance is the percentage of closed pores (Benkreira et al. 2011; Jimenez-Espadafor et al. 2011). Therefore, increasing the crumb rubber amount as a filler will increase the porosity of the product because of the irreguler shape of this additives.

2.5 Modeling of materials for acoustic applications

Porous noise control materials have two phases: the solid, usually a fibrous component referred to as the frame, and the interstitial fluid contained within the pores formed by the frame. Owing to their relatively low density, porous

materials are not generally used as barriers, but they are frequently used as efficient sound absorbing materials, in which they convert organized acoustical motion into heat. Sound absorbing materials dissipate acoustical energy largely by the interaction of their solid and fluid phases. In particular they convert acoustical energy into heat by viscous means (associated with oscillatory shearing of the fluid in the vicinity of the surface of the fiber); thermal means (irreversible heat flow from the interstitial fluid to the fibres forming the frame); and by structural means (irreversible losses associated with flexure of the fibres comprising the frame).

Porous materials such as glass fibre, mineral wool, and open or partially open-cell foams have many applications in automotive noise control in particular: e.g., as headliners, seats, under carpets, trim lining, dash mat lining, cavity interiors, parcel self-lining, panel damping, etc. And of course, they are widely used in applying noise control, aircraft applications and in buildings. The objective of this section is not to discuss all possible applications of porous materials, but rather to introduce fundamental terminology and concepts related to porous materials, and especially elastic porous materials such as foams, to facilitate later discussion related to applications.

Most porous material theories are formulated in terms of the macroscopically measurable physical properties of the frame and the fluid: e.g., flow resistivity. The advantage of such an approach is that it enables the influence of the various directly measurable physical properties of the porous material to be identified; thus a particular set of physical parameters can be specified that will result in a porous material having a specified level of acoustical performance. In addition, easy-to-use approximate models derived by neglecting the physical

parameters that are judged to be least significant in a particular situation (e.g., the bulk elastic properties in the case of a nearly rigid porous material exposed to airborne incident sound) may be used in preliminary analyses.

It should be noted that there is a direct link between the microscopic structure of a porous material (e.g., fibre radius, fibre shape, fibre orientation, fibre material density, the number of fibres per unit material volume, grain size etc.) and its macroscopic properties.

Many mathematical models have been developed in order to optimise porous material properties. These models can be classified according to how many non-acoustical parameters these models depend on to predict the other acoustical properties.

2.5.1 One Parameter Model (Delany and Bazley Model)

This model is an empirical model and can predict accurately the acoustic characteristic impedance and propagation constant in highly porous fibrous materials and foams (Bazley 1970). The attractive feature of the widely cited work by Delany and Bazley is that, unlike many other models, it requires a knowledge of only one macro-structural material characteristic which is the static flow resistivity (σ). In the case of a homogeneous material with a high proportion of open, interconnected pores the flow resistivity is the most fundamental non-acoustic property which relates directly to its acoustical performance.

The Delany and Bazley model (1970) was originally designed for modeling fibrous media. One has to admit that the model is capable of predicting satisfactorily the acoustic impedance of high resistivity, low porosity outdoor porous surfaces (Embleton 1983). So far we have demonstrated that the Delany

and Bazley model (1970) can provide extremely accurate predictions to the acoustic performance of high-porosity materials and satisfactory predictions of the acoustic performance of porous soils with high flow resistivity and low porosity.

Unfortunately, the model suffers from three fundamental limitations, the model was originally developed to predict the acoustic properties of fibreglass and therefore it does not capture the acoustical phenomena taking place in loose granular media with limited porosity, e.g. in soils; It is important to realise that this model has a poor causal behaviour so that its applications in time-domain calculations should be avoided. It was also noted that the application of the Delany and Bazley model for the prediction of the impedance of soils with moisture is rather limited. The acoustic behavior of typical soils is very sensitive to the amount of moisture and this behavior cannot be captured by the Delany and Bazley formulae in their original form. Such a poor performance is of major concern as it is now a part of the future European standard prediction method for outdoor sound propagation, (Harmonoise 2003).

2.5.2 Two-Parameter Models (Attenborough Model)

An alternative practical method for the prediction of the acoustic properties of highly-resistant, low porosity soils is to use the 2-parameter model proposed by Attenborough (1992). This model was theoretically founded and requires a knowledge of the effective flow resistivity (σ_e) and the effective rate of change in the porosity with the layer depth (α_e). The root mean square error between the measurement and prediction was estimated to be 6%, which is an improvement

to the Delany and Bazley model (1970). This accuracy is fully adequate for modeling of realistic ground conditions and outdoor sound fields.

There are classes of porous materials for which acoustical properties cannot be predicted accurately by either the one or two parameter models presented so far. The materials in question are relatively uniform porous structures composed of loose or consolidated grains and/or fibres. These materials are characterized by medium flow resistivity (5 –100 K Pa s m^{-2}) and porosity values (30-80%). Accurate modeling of the characteristic impedance and complex wavenumber of these structures requires some additional parameters as well as the data on the material thickness. The main applications of this model are in outdoor sound propagation and surface impedance characterization of soils.

This model requires measured or deduced data on the effective flow resistivity of the porous soil and the rate of porosity change with the depth. The latter is a semi-empirical parameter the value and sign of which can be adjusted to improve the fit between the predicted and measured of the surface impedance. This model is capable of providing much more accurate predictions of the acoustic impedance of porous soils with variable moisture content (Mohamed 2005). Two particular models which are presented in this section are:

- The empirical Miki model (Miki 1990); The Miki model introduces modifications to the Delany and Bazley expressions. The purpose of these modifications was to include the porosity and tortuosity data and to improve the causal behavior of the new empirical expressions via a more careful choice of the polynomial coefficients and powers.

- Brennan and To engineering model: The purpose of the Brennan and the work was to present a new, practical but, physically-based engineering model which is able to “bridge the gap between the simple and the complicated theories, which can facilitate physical insight into the acoustical behaviour of rigid-frame porous materials”(Brennan and To 2001).

2.5.3 Multiple Parameter Models

These models are based on three or more non-acoustic macroscopic characteristics such as porosity (α), pore tortuosity (Ω) and air flow resistivity (σ). They are able to provide satisfactory predictions of the fundamental acoustic properties of granular and complex fibrous media. The idea of basing a model on the above characteristics is very sensible because these are directly measurable quantities fundamental to the low and high-frequency behavior of rigid-frame porous media.

In the last 10-20 years several models have been developed which require data on the probability density function (PDF) for the pore size distribution (e.g.(Yamamoto 1988),(Attenborough 1993) and (Horoshenkov 1998)). It can be argued that for many practical applications the pore size distribution data provides the most practical foundation for accurate predictions of the vicious and thermal processes in the porous medium at different scales. Unlike some other non-acoustical parameters which are needed to model the acoustical properties of heterogeneous porous media, e.g. the viscous and thermal characteristic lengths used by Allard (1993), Only and Boutin (2003) and Sgard et al (2005), the pore size distribution is a directly measurable property. For this purpose, a simple

method of measuring the pore size distribution based on the water suction experiment can be adopted (e.g.(P. Leclaire 1998)).

2.6 Summary of literature review

The abundance, high elasticity, irregular shape of scrap tyres shred residue make it one of the best raw materials for producing vibro-acoustic materials. In this study tyre shred residue has been used as a raw material to produce vibro-acoustic and thermal insulation products with performance comparable to or higher than commercial products. In conclusion, elastomeric waste from scrap tyres can be a very effective waste stream for noise reduction showing huge potential if utilized to produce materials for vibro-acoustic applications.

CHAPTER THREE

EXPERIMENTAL METHOD

3.1 Introduction

This chapter describes the materials and methods used in the undertaking of this research. Firstly the elastomeric waste materials and binders used to compound them into final acoustic and thermal products are introduced; followed by a comprehensive description of the procedures adopted for the production of samples and the testing of their properties. As stated in the introductory chapter, the aim of the research was to develop using elastomeric wastes and appropriate binders new acoustic material structures for the well-established applications in cavity walls, flooring under-layer and “noisy pipe” cladding.

The novelty resides in producing in the experimental programme porous structures with:

(i) Distributed open cells (large and small randomly distributed).

(ii) Stratified open cells, characterizing these structures and measuring their acoustic properties.

In addition, the heat insulation properties of these structures will also be measured in an attempt to assess the potential for the double benefit- acoustic and heat insulation. It is anticipated on physical principles that the open cell nature of the acoustic material is not conducive to good thermal insulation which requires in principle closed pore cells.

Another important aspect of the research was, concurrent with developing pipe cladding insulation, develop a new simpler technique to measure sound

absorption of pipe cladding without using the expensive reverberation chamber method. The method is also explained in this chapter.

3.2 Waste Material and Binder System

The materials used in this study can be categorized into the following two groups: the elastomeric waste particulates and the binders. The elastomeric particulates were car bumper crumb, car tyre crumb rubber and fibrous tyre shred residue as depicted in Figure 3.1. These waste were supplied by Credential Tyre Recycled Ltd (Rochdale, UK) who produces some 25 tonnes/day of the material out of a European total of 12.7 million tonnes (Fan et al. 2005). The difference between the two types of waste is that the crumb rubber consists wholly of rubber and the tyre shred residue is made of very fine rubber grains trapped in long nylon fibres. A size analysis Figure 3.2 of these materials showed the rubber crumb particles to lie in the range 4 to 7mm and the tyre shred residue rubber grains to less than 1mm enrobed in long 3 to 10mm fibres with the ratio rubber to fibre being 40/60 g/g.

Figure 3.1. Rubber crumb and tyre shred residue.

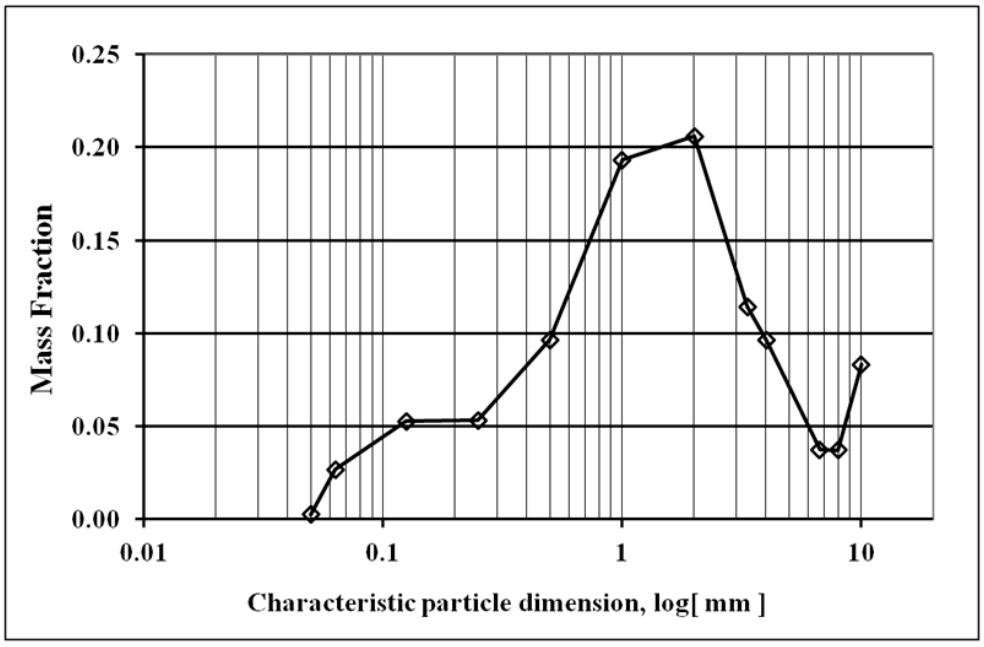

Figure 3.2. Weight distribution of the particle size for tyre share residue.

Table 3-1 Weight fraction of the particle/fibre size for tyre shard residue.

Sieve aperture (mm)	Average weight fraction
10.00	**0.083**
8.00	**0.037**
6.70	**0.037**
4.00	**0.097**
3.35	**0.115**
2.00	**0.206**
1.00	**0.193**
0.50	**0.096**
0.25	**0.053**
0.15	**0.053**
0.063	**0.027**
<0.063	**0.003**

As for the binders, two types were used; one a polyurethane (PU) based and a second, bio-based, styrene butadiene rubber (SBR). The consideration of SBR falls in the sustainability dimension of this research but also because of its high elasticity (lower Young modulus) compared with PU. In this research, the

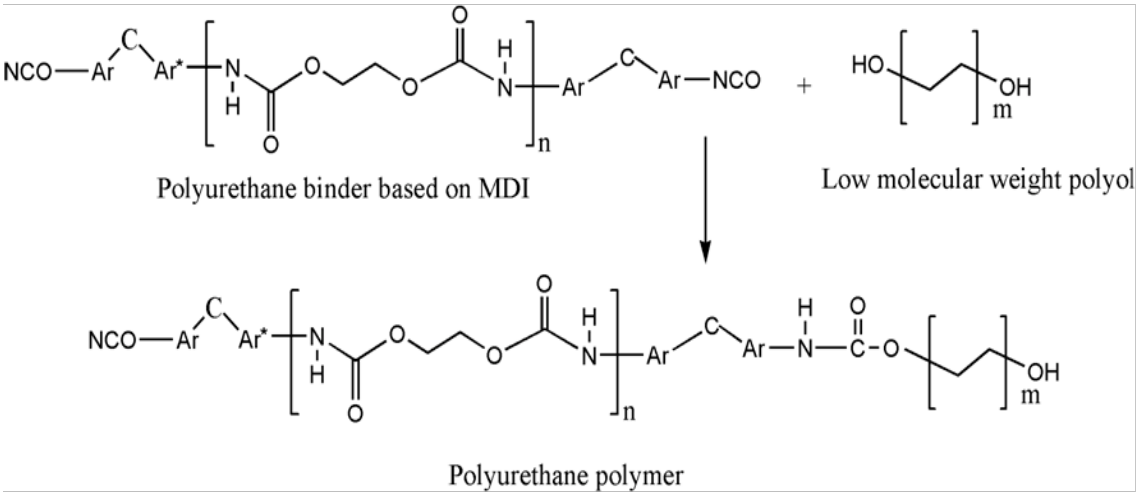

PU used was made up of a polyol (Flexilon 1117) supplied by Rosehill Plymers Ltd and an aromatic isocyanate, diphenylmethane di-isocyanate (MDI) as it leads to a flexible polyurethane foam which allows the formation of a high proportion of open cells. The reaction scheme between the polyol and MDI is given as:

The elasticity of the PU binder so formed depends critically on the molecular weight and functionality of the polyol. High molecular weight polyol leads to a flexible PU whereas low molecular weight polyol reacts faster with the MDI and produce more rigid PU. Now when in contact with water added to merely wet the waste particulates, the PU reacts to produce CO_2 gas, the foaming agent. Clearly, a flexible PU will facilitate the flow of CO_2 thus leading to large open pores whereas a rigid PU will hinder the flow of CO_2 and will lead to a closed small pore structure. Therefore, tailoring the elasticity and porous structure is key to producing material that is good for acoustic (open pores) or thermal (closed pores) insulation. This tailoring requires the control of the PU elasticity (molecular weight of the polyol) and of the amount of CO_2 gas produced. The kinetics of the reaction $MDI+H_2O \rightarrow CO_2$ have been measured (see Figure 3.3) and showed several characteristics:

- The reaction is slow, taking 30 minutes to complete.
- The reaction yield is low (20 to 30%) but can be increased if the initial MDI is low, allowing all the NCO groups to convert into CO_2.

In conclusion, the chemistry of the binder reacting system is key to acoustic/thermal insulation performance and will need to be optimized in the

experimental programme by controlling the effect of the molecular weight of the polyol and the amount of MDI and H_2O added. The increasing in water content in reactant materials will increase the rate of reaction as shown in figure 3.3 series 1 below.

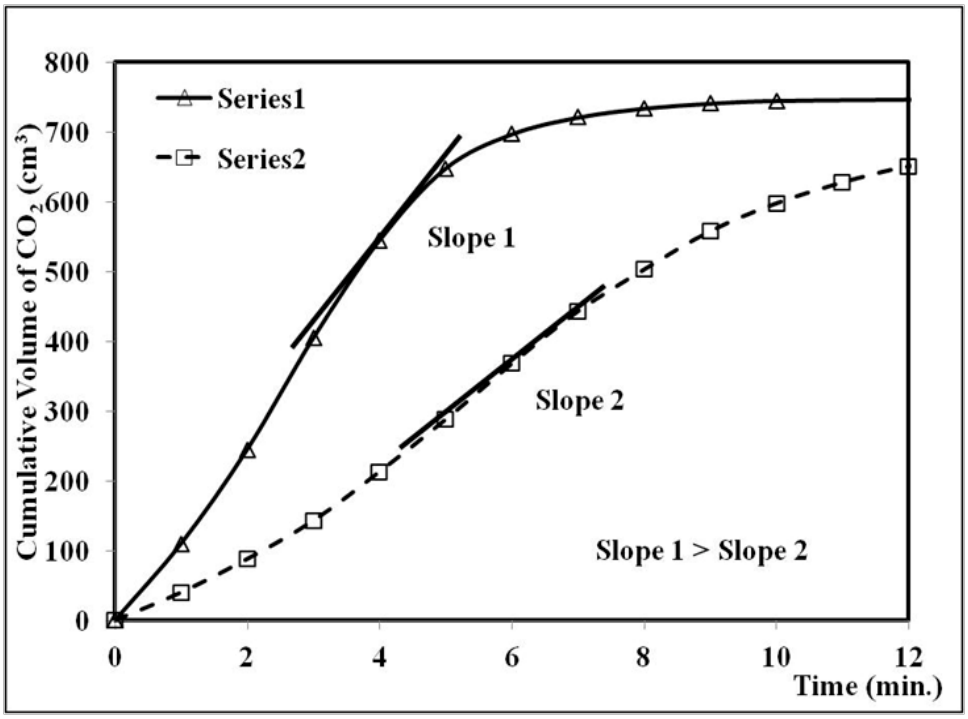

Figure 3.3. Illustration of finding the rate of polyurethane polymerization from slope of the cumulative volume CO_2 curves.

3.3 Compounding and molding apparatus

As explained in the introductory chapter cavity wall, under-layer and pipe cladding acoustic insulation materials were formed in this research in order to assess comprehensively the potential for application. In all cases, mixing of the particulates and the binder systems was required and this was achieved using manual mixing when the quantities were very small, a 2L kitchen food processor or an industrial type mixer when the quantities required increased. The food processor type mixer was fitted with an “egg beater” type impeller and the industrial mixer with an anchor type impeller. The geometry and dimensions of

these impellers and holding vessels are shown in Figure 3.4. The procedure for manual mixing of small quantities (less than 500g) is given in Table 3.2 and it was adhered to in all cases when manual mixing was performed.

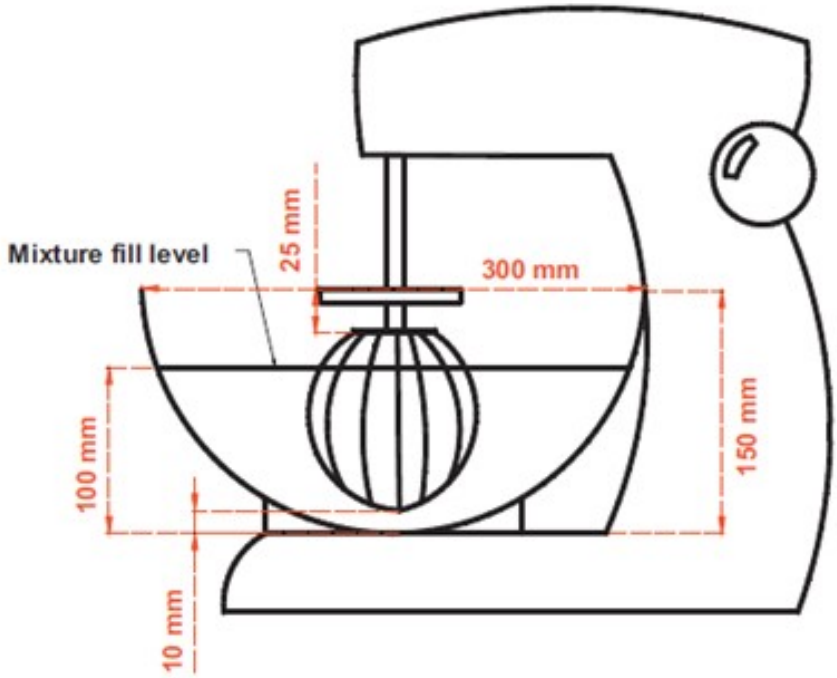

Figure 3.4. Schematic illustration of the compounding apparatus.

Table 3-2. Composition of the material mix.

Binder : TSR (%)	Weight of bio-binder (g)	Weight of TSR (g)	Density (kg/m^3)
0:100	0	500	164
10:90	50	450	187
20:80	100	400	277
30:70	150	350	346
40:60	200	300	380
50:50	250	250	427
60:40	300	200	482

With regard to molding, again this was dependent on the size of the sample produced and the molding conditions. Remember that the important objective of the research was to create:

(i) Randomly size cells.

(ii) Stratified pores structure.

To achieve a random, multi-size cells structure in one single layer, two methods were investigated. The first approach was the application of vacuum to a foaming fibre-rubber crumb-PU system and this required a transparent molding cylinder fitted appropriately with valves that controlled the application and release of pressures. Figure 3.5 and 3.6 give a schematic and the actual components of the set-up. An analysis of this structuring approach will be given later in the result section. It is sufficient to understand that the application of a vacuum will create a larger pressure drop compared to expansion against atmospheric pressure. Closer to the top of the sample, there will be a propensity for the production of larger cells formation compared to regions deep below. Clearly, for the vacuum to be effective, it must be applied whilst the foaming reaction is proceeding so that the expansion of the foaming gas is controlled whilst the gas is being produced. The transparency of the molding allows this to be observed and monitored. This method of structuring may be referred to as “physical” in the sense that control of structure was made by the application of vacuum.

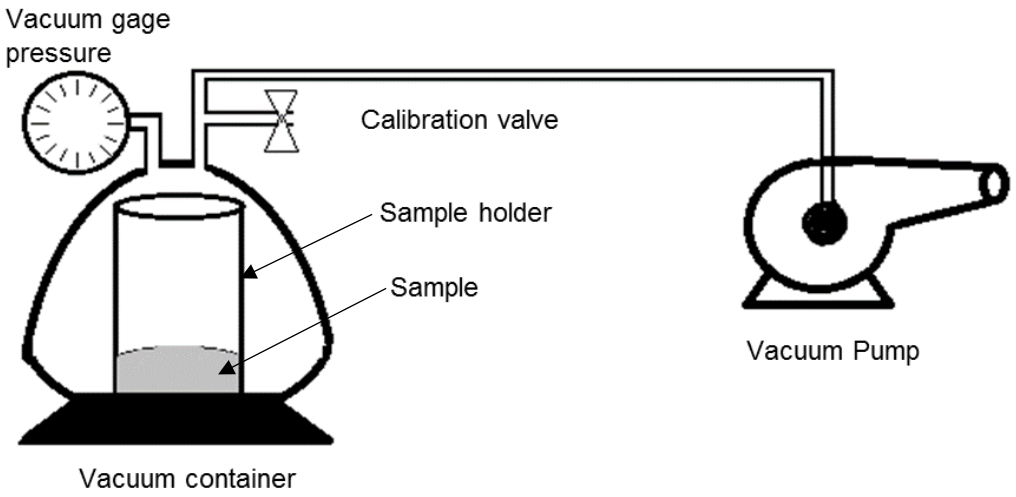

Figure 3.5. Schematic of the instrument for polyurethane production under vacuum pressure.

Figure 3.6. *(a)* Vacuum container with pressure gage, valve and solid mould. (b) Improved vacuum container with a manual valve, vacuum gage pressure and clear mould.

As the control of the vacuum is critical, gauges of different scales and sensitivities were used and these are shown in Figure 3.7 together with the vacuum pump Figure 3.8.

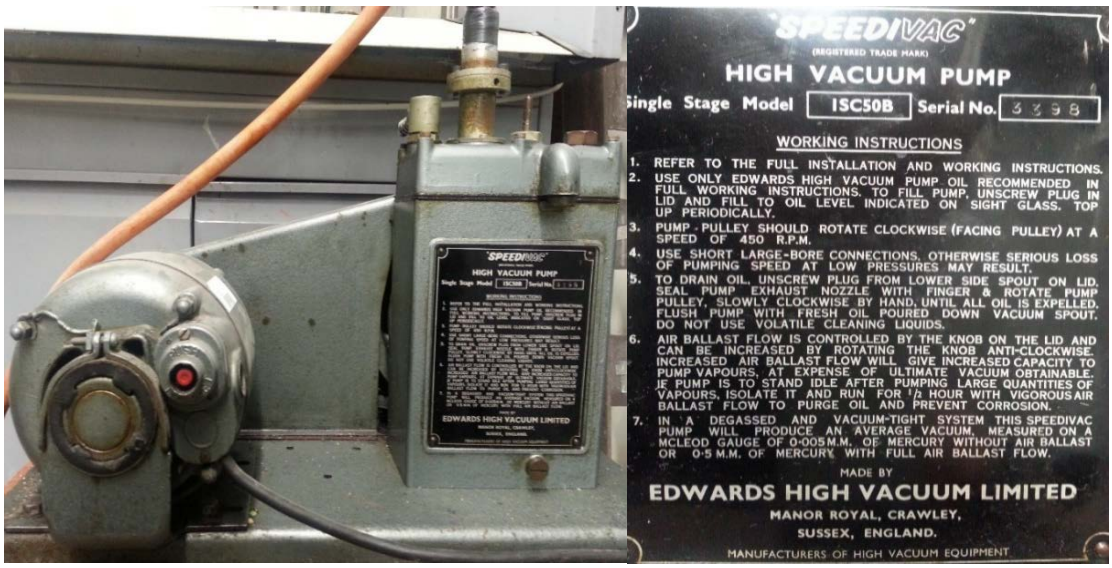

Figure 3.7. Photograph of vacuum pump pressure.

Figure 3.8. Two different types of vacuum pressure gages with different sensitivities.

The second method of producing random multi-size cells relied on controlling the size distribution of a non-foaming fibre-rubber crumb particulate system using SBR as the binder. The main raw material used was tyre shred residue from granulated tyres with fibre length ranging from 1mm to 60mm and fibre diameter in the range of 20–30μm. A rationale for the random pore distribution is the variety of porous structures possible when varying the amount and size of particulate and the quantity of binder. A merit of such method is that the end product is fully recyclable as the SBR used is water based and fully soluble in water. Again, as there is no chemical reaction occurring, we may describe this approach as being purely “physical”. Figure 3.9 shows six different formulas of random multi-size porous materials which are produced by using SBR water base binder.

Figure 3.9. Multi size porous materials which are produced under different formulas.

To achieve a stratified pore structure, a multilayer (3-layer system) approach was used, each layer producing one pore size, using a rectangular box base and rectangular frames that stacked on top of each other. Pore size in each of the three layers was controlled by an appropriate choice of waste material particle size, foaming PU binder formulation and the extent of foaming (thickness of the layers). The first layer was put in the base and its foam expansion constrained to a height by a lid fastened on the top. Once the first layer structure was deemed to have formed, the lead was opened and a frame placed on top to hold the second batch of foaming material forming the second layer, it too constrained to a height by a lid fastened on the top. Once the second layer structure was deemed to have formed, the lead was opened and a frame placed on top to hold the third batch and the same procedure repeated. Note that in order to prevent the mixed compound from sticking to the base and the lids, these were covered with a Teflon layer. Figure 3.10 shows the arrangements and the appropriate dimensions of this type of mold.

Figure 3.10. Photograph of the wood mould of the stratified insulation material.

Table 3-3 classifies the control parameters in the production of the prototypes made and the corresponding mixers and molds.

Table 3-3. Layers raw materials weights and flow resistivity.

Layer No.	TSR/ g	MDI/ g	Polyol/ g	H_2O/ g	Flow resistivity σ
Layer1	75	60	15	15	89,930
Layer2	75	60	15	10	127,463
Layer3	75	60	15	5	120,736

3.4 Porous Structures Properties Measurements Method

Having produced the samples, the next step of the programme was to characterize the structures made in terms of their total porosity, porosity distribution, air flow resistivity, tortuosity and dynamic elastic modulus using standard methods.

3.4.1 Porosity

Porosity is at the heart of this research and within a material, it can exist as:

(i) Open pores which allow liquids or gases to flow through.

(ii) Closed pores trapped within a material and not interconnected thus do not allow flow through the structure.

(iii) Blind pores, open interconnected pores that terminate inside a structure, effectively “closed open pores”.

In a real system, it is likely that no structure falls within one of these 3 categories, rather they will be a preponderance for one type more than another, i.e. say a structure may be 90% open pore and defined simply as an open pore.

In addition, pores in a material are variable of different size, so a porous material will generally exhibit a pore size distribution.

Hence and in order to fully characterize the structures developed in this study, the total porosity, open porosity, closed porosity and pore size distribution were measured.

3.4.1.1 Open cell porosity

In principle, this is the easiest property to measure and can be found by simply measuring the bulk density of a sample of the material and the density of the solid forming it:

$$\Omega_{total} = 1 - \left(\frac{\rho_{bulk}}{\rho_{solid}}\right) \quad (3.1)$$

In our research, the materials formed are mixtures of particulates and binder and determining accurately a “solid” density is difficult. And as the structures developed in this research are essentially open cells, a fluid pore flow method is appropriate (Leclaire et al. 2003). This method uses the set up described in Figure 3.11 which consists of two 60ml chambers and a U-tube water manometer connecting them both. The pressure/volume in the two chambers and in the manometer chambers is controlled by glass syringes suitably calibrated and graduated for accurate readings. Once calibrated the set up gives a direct measure of the open cell porosity.

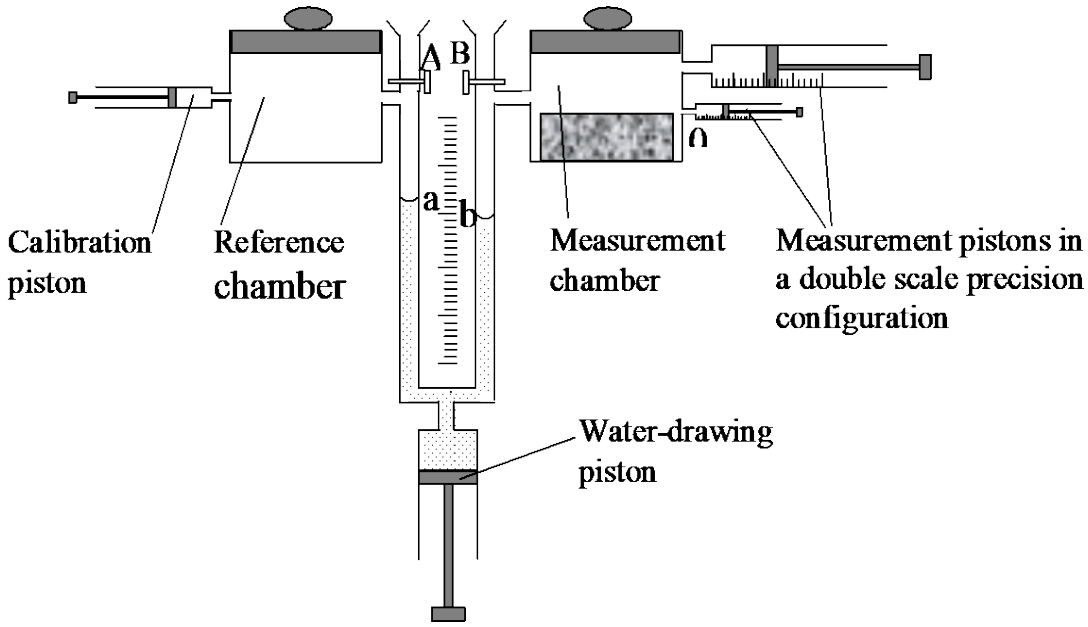

Figure 3.11. Schematic diagram of the porosity test instrument

The porosity measurement procedure starts with calibration to equalize the volumes of the reference chamber and the measurement chamber in the absence of the sample and with the measurement pistons set to their zero positions. The porous sample is then placed in the measurement chamber. The reduction in the volume of air in the measurement chamber due to the introduction of the porous solid corresponds to the volume of the solid of the porous sample. The accuracy of this method is within 3% for materials of low porosity (<0.3) and 7% for the case of materials with medium and high porosity material (>0.5).

A second method tried was more to measure the weights of a dry sample and the weight of a sample saturated with water. The dry sample was tightly inserted into a container (200 and 1000 ml) of the same shape as the sample and with an open top flush with the top surface of the sample. A water-saturated sample was obtained by submerging the container in water in a vacuum vessel

covered with a perforated plate. A weight was put on the top of the plate to ensure that the sample was fully immersed and vacuum applied until no more bubbles are released from the open surface of the material. At this point, the pump was switched off to release the vacuum and allow the container with the sample to be removed carefully from the vessel to determine its wet mass. Knowing the volume of the sample (v_s) and the difference between the dry and wet weights$(m_w - m_d)$**,** the porosity can be calculated as:

$$\Omega = \frac{(m_w - m_d)}{1000 \times v_s} \tag{3.2}$$

In spite of its simplicity, this technique provides an accurate determination of open cell porosity with errors less than 5%.

3.4.1.2 Porosity Distribution

The water suction method was used to measure the pore size distribution. The principle of measurement here is the application of a pressure drop that extracts a measured volume of water held in the sample by the capillary action effect.

In the experiments, a 100mm sample was inserted into a sample holder with the same internal diameter as shown in Figure 3.12. A filter paper was placed on the bottom of the sample holder and its edge sealed before the sample was inserted into the holder. The relative height of the sample holder was fixed and measured. A rubber tube was connected to the bottom of the sample holder and the bottom of the burette. The start point (zero position) was set at the position where the water in the burette was at the same level with the water in the sample

and at equilibrium pressure, i.e. at the level being normally immediately above the porous sample.

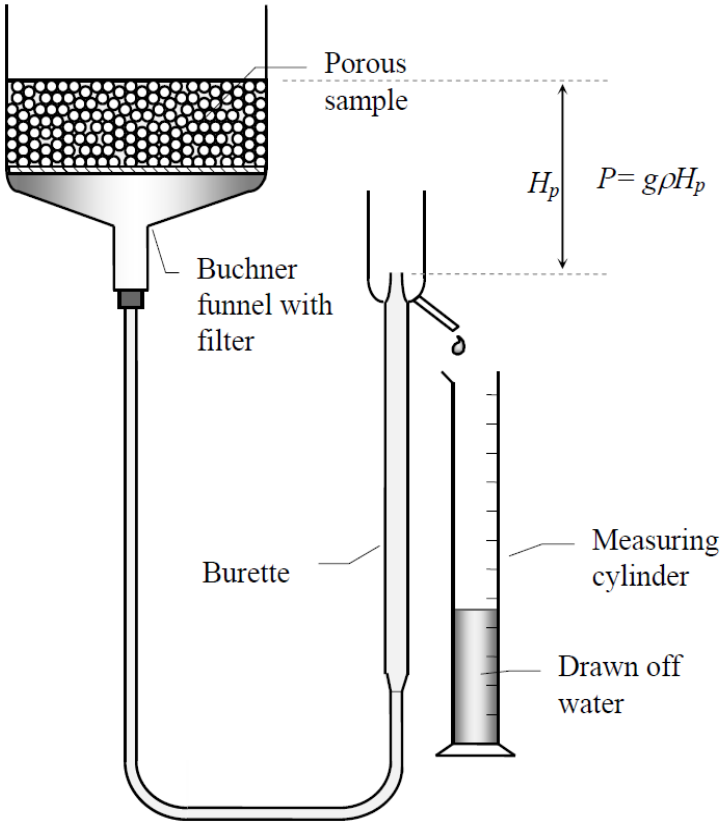

Figure 3.12. Schematic of the water suction method

The water suction was achieved by lowering the burette position from the zero point. The height of the burette was decreased by 5 mm until water stopping, in order to extract a controlled amount of water from the capillary pores in the material sample. A measuring cylinder was used to collect the extracted water leading to a cumulative water volume curve vs. level head H_p as shown in Figure 3.12. The experiment was completed when no further draining of water with a further increase in the value of the reduced head level was observed.

The suction pressure P applied to the water in the material pores was determined from the reduced level head H_p, the density of the water ρ and the gravitational acceleration g:

$$P = \rho g H_p \tag{3.3}$$

This pressure relates directly with porosity Ω and the induced capillarity action through the surface tension of the water σ and the curvature r_c of the pores as:

$$P = \frac{\sigma}{r_c} = \frac{\sigma}{(\frac{\Omega}{2cos\theta})} \tag{3.4}$$

In the above equation, θ is the wetting angle between the water and the material sample, which has to be determined separately by measuring the angle that a drop of water forms on the material sample. As in this case, the particulates are fully wetted by water, the angle approaches zero.

Using the above equations, the probability density function of the pore size distribution could then be found by normalizing the cumulative water volume (V_c) by the total volume of open pores (V_d) and numerically differentiating the obtained cumulative pore size distribution. Figure 3.13 gives an example of such a probability density function.

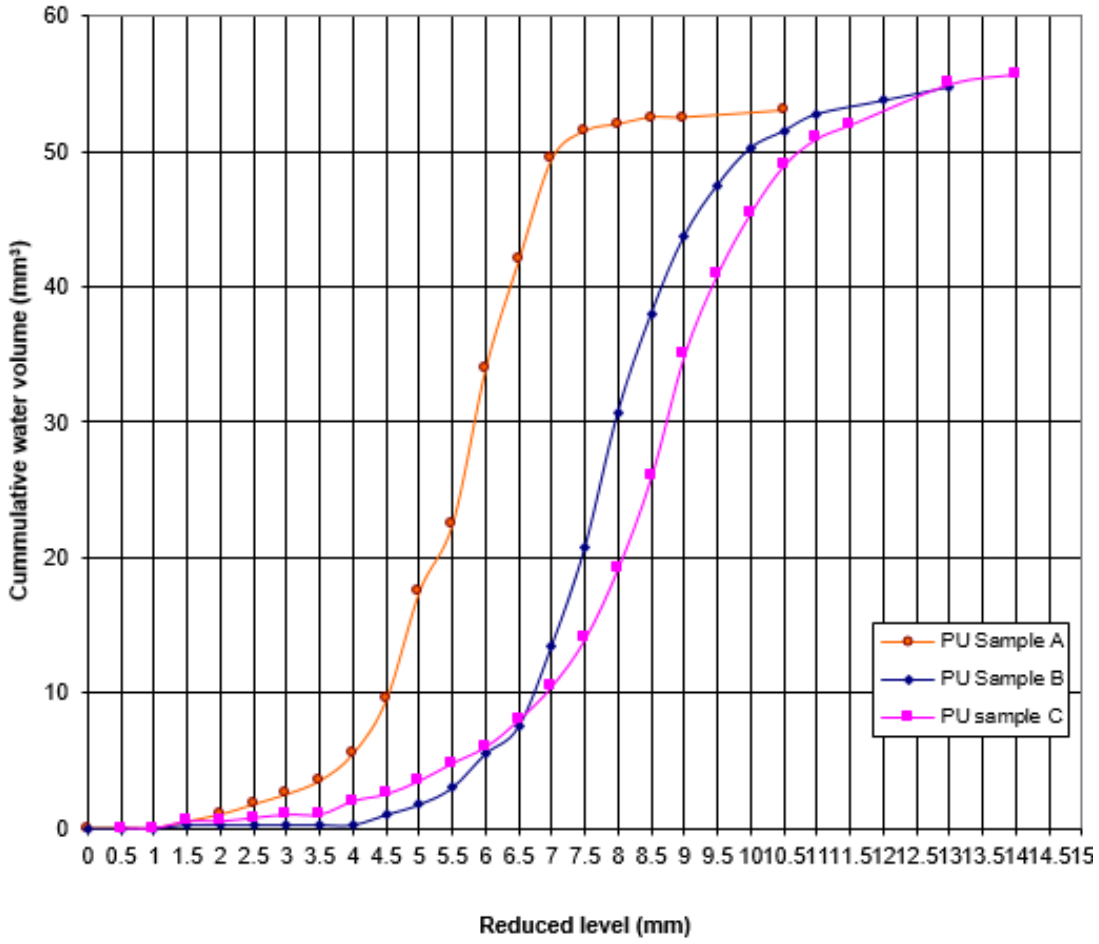

Figure 3.13. Cumulative distribution of water in some samples of the developed porous media.

3.4.2 Airflow Resistivity

Like tortuosity, flow resistivity is another fundamental property that describes acoustic absorption of fibrous and granular materials. As the name implies, it determines the ability of a sound wave to penetrate a material sample and be attenuated. Higher values of flow resistivity imply obviously higher absorption and attenuation. The experimental setup for measuring the flow resistivity used in this work is shown in Figures 3.14 and 3.15. The procedure follows ISO 9053: 1991, the

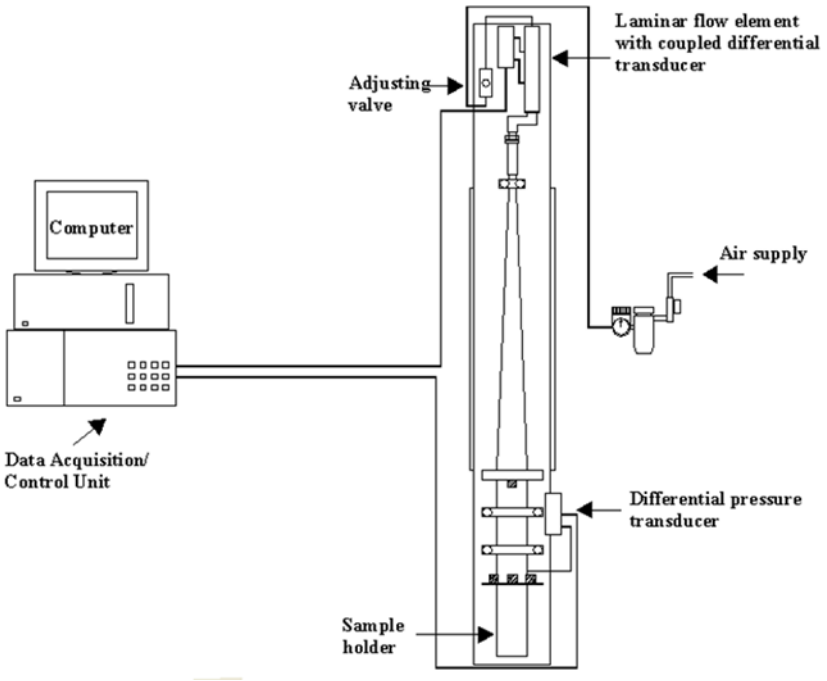

Figure 3.14. Flow resistivity measurement set-up.

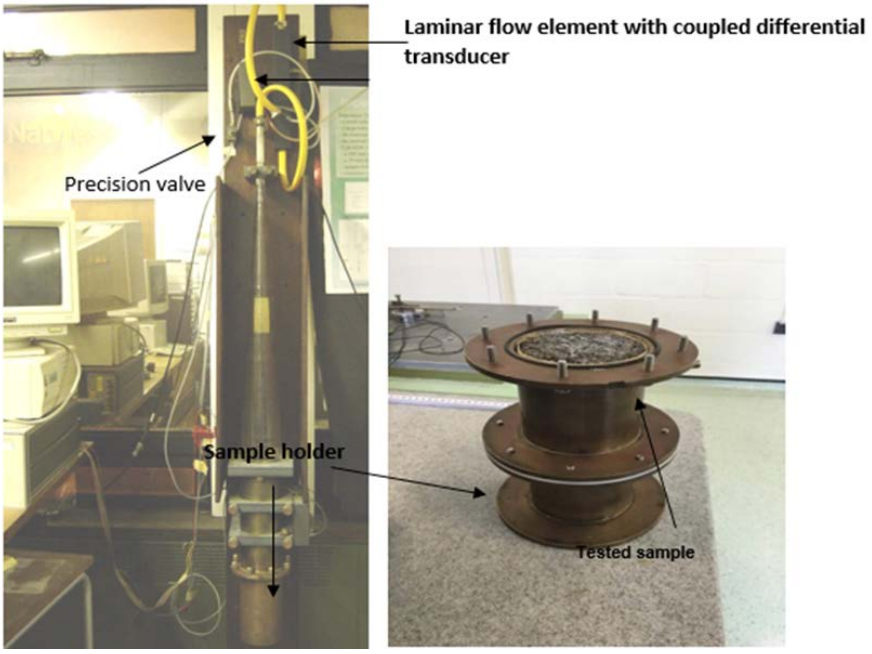

Figure 3.15. Flow resistivity measurement with sample holder.

standard for the determination of the air flow resistivity of acoustic materials (Champoux and Allard 1991). Essentially, the set-up is designed to measure the pressure drop of an air flow through a sample of the material being tested. Thus, a sample was cut into a cylindrical shape, 100mm in diameter, then inserted into the sample holder, of diameter a few mm larger than 100mm. The sample was sealed around its edge with putty in order to prevent air leakage through the gap between the sample and the holder. Air was supplied from a compressed air reservoir, and its flow was controlled using a precision valve connected to a flow meter measuring in the range 0.3 – 30 litre/min with an accuracy of 0.1 litres/min(see figure 3.16). The air so measured comes out of the flow meter and travels through a conical section glass tube to reduce the level of air turbulence then penetrates the sample and exits out of it. Two air pressure differential transducers were connected 50mm above the sample holder. These transducers allowed to measure the pressure surge due to the finite permeability of the investigated porous sample in the ranges 0.1 – 20 Pa and 0.5 – 100 Pa. At the beginning of this experiment, the valve was set to ensure the minimum possible flow rate of 0.3 - 0.5 litre/min. The valve was then opened slowly in steps to increase the discharge by 0.3-0.5 litre/min. A time period of 30-40 sec was given between each step to allow to stabilise the laminar flow in the sample holder.

The data on the flow rate and differential pressure was acquired using HP-A/D converter controlled by special software implemented in HP VEE language Figure 3.17. The data was saved automatically in the form of a text file and then plotted and processed with MS Excel to determine the gradient of the

dependence of the pressure drop along the sample thickness ($\Delta P/d$) on the flow rate.

Figure 3.16. Precision valve.

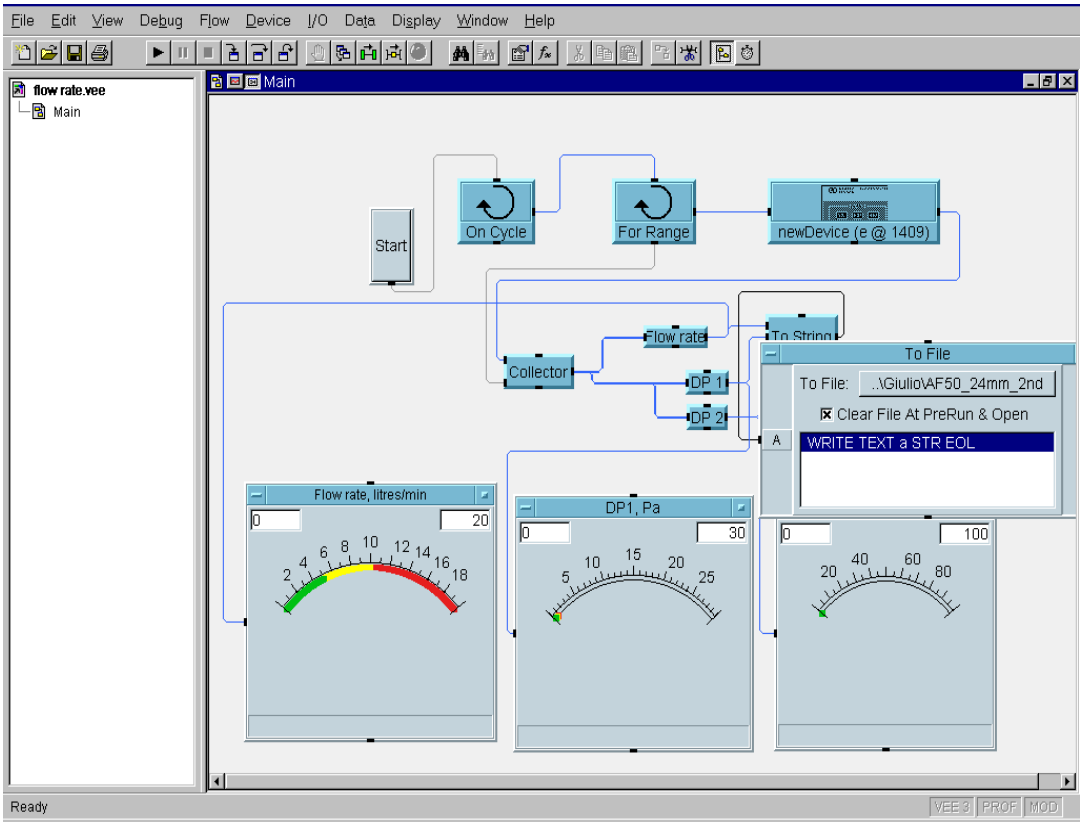

Figure 3.17. HP VEE data acquisition software screen.

Figure 3.18 gives the flow resistivity and it has been calculated based on this formula $R = (\Delta P/d)/V$, where V is the average air velocity calculated from the flow rate. As an indicator of values, it has been noted that for a hard-backed porous layer of thickness, the optimal flow resistivity which ensures the maximum acoustic absorption in a broad frequency range is $\sigma=3\rho_0 c_0$ (Kosten 1949).

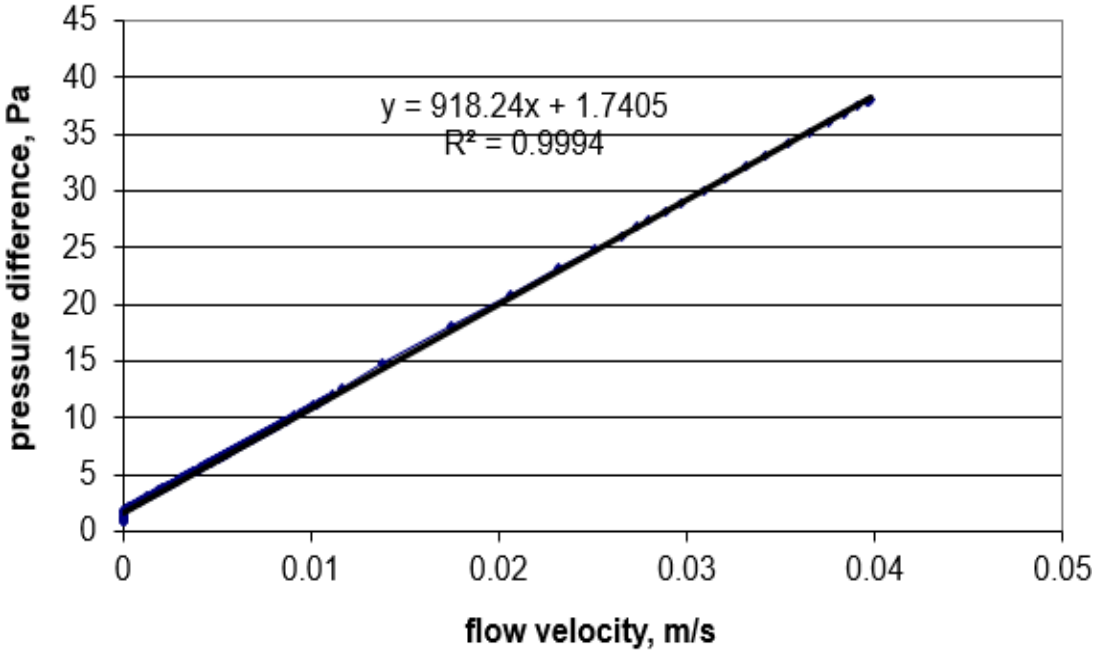

Figure 3.18. A calculation example of flow resistivity from the flow dependent differential pressure.

3.4.3 Tortuosity

Physically, tortuosity accounts for the twistiness of the pore in a material sample. As sound absorption is essentially an energy attenuation process, it is not surprising that its importance to the modelling of sound propagation in porous media has long been realised (Kosten 1949). One of the first fundamental studies of the effects of the tortuosity has been completed by Attenborough (1983b). In the simplest case, tortuosity, relates to the ratio of the actual path h_e, taken by a

high-frequency sound in a porous sample to the sample thickness h, a value always greater than 1, i.e. $\alpha=he/h>1$. Consistent with sound attenuation as a volume process, a more realistic definition of the tortuosity is the ratio of two volume integrals:

$$\alpha_{\infty} = \int_{\Delta} v^2 dV \left(\int_{V} v\mathbf{n} dV \right)^{-2} \tag{3.5}$$

where; v is the oscillatory flow velocity and n the unit vector in the direction of sound propagation.

There are several methods of measuring tortuosity the majority of which are indirect for the obvious reason that measuring the actual path length $\boldsymbol{h_e}$ is difficult if not impossible in a porous structure. Here we detail three particular methods which are, perhaps, the most common and reliable. Allard proposed the first method in 1994, based on the ultrasonic time of flight in the porous medium (J.-F. Allard 1994). The method assumes that at high frequencies the thickness of the viscous boundary layer becomes considerably smaller than the characteristic pore dimension, and the phase velocity of the sound wave in a porous medium correlates simply with tortuosity as:

$$c_b = \frac{c_o}{\sqrt{\alpha_{\infty}}} \tag{3.6}$$

where; c_0 is the speed of sound in air.

For a typical noise control material with mean pore size of 100μm (e.g. fibreglass), this regime is attained at frequencies greater than 25000 Hz.

A typical setup which has been developed and used routinely at the University of Bradford for measuring the tortuosity from the ultrasonic time of flight

is shown in Figure 3.19. It consists of a high-frequency tweeter mounted at the top of a PVC tube. A 48 kHz ultrasound wave is transmitted from the tweeter and received by two 1/4" microphones mounted on the top and the bottom of the sample with their centres aligned with the centres of both the sample and the tweeter as shown schematically in Figure 3.20. A separate measurement is carried out in the absence of the sample to determine the actual sound speed in air. The phase speed in the sample is measured by comparing the time delay (Δt) between the wavefronts of the incident and transmitted waves and making use of the expression:

$$\sqrt{\alpha_\infty} = \frac{c_o\,\Delta t - d_m}{h} \tag{3.7}$$

where; d_m=6.35×10^{-3} m is the diameter of the 1/4" microphone.

In the actual experiments, the transmitted sound between the two microphones was recorded using a professional sound card Marc-8, high-pass filtered and processed using WinMLS software. The time between the impulse response recorded on the top and bottom microphones was determined from the graph as shown in Figure 3.21. The sampling rate was set to 96000 Hz which allowed the signals with frequencies of up to 48 kHz to be generated, recorded and processed. The number of bits in the WinMLS for both the input and output was set to 16. The sound speed in air, c_0 which depends on the temperature (*T*) was predicted using following the correlation (3.8):

$$c_o = 332 + 0.6\,T \tag{3.8}$$

Following this method, tortuosity data for consolidated samples were measured to check on the accuracy of the technique, found here to be within an

error of $\pm$ 4 to 5%, table 3-3 and 3-4 present such data indicating that the tortuosity of the sample with broader grain size distribution is higher than that for a sample with a single class of grain. Typically and expected, materials with higher values of tortuosity exhibit a better acoustic absorption performance in the low-frequency range.

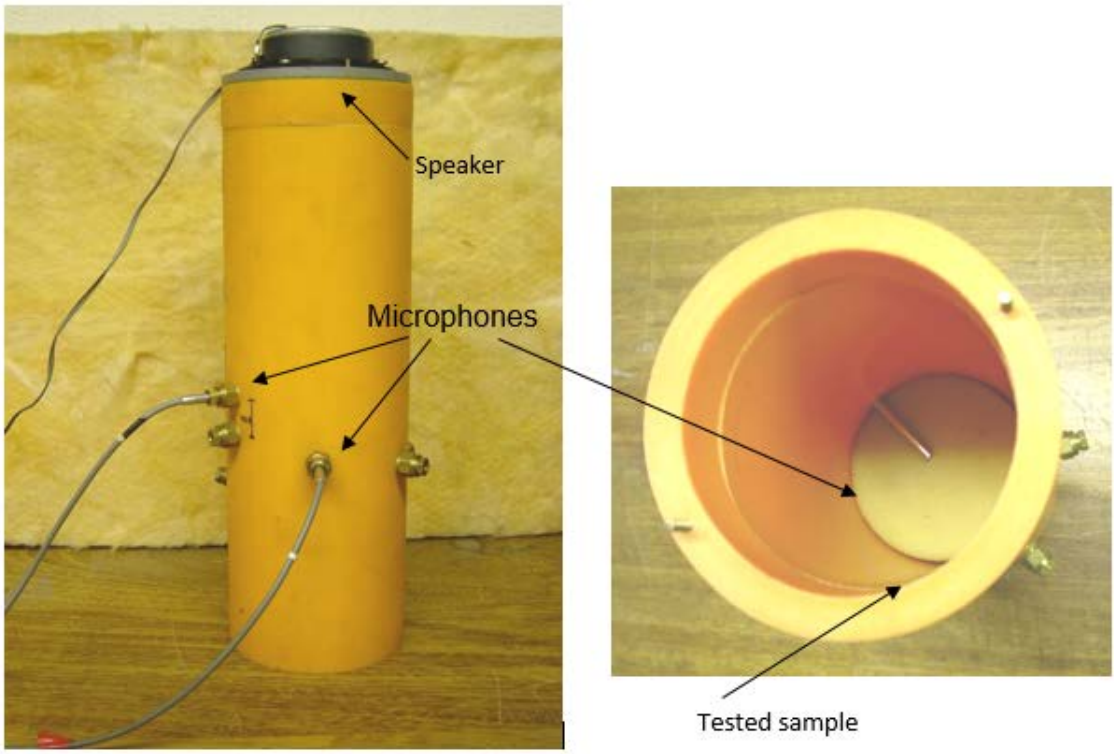

Figure 3.19. PVC cylinder for tortuosity measurements.

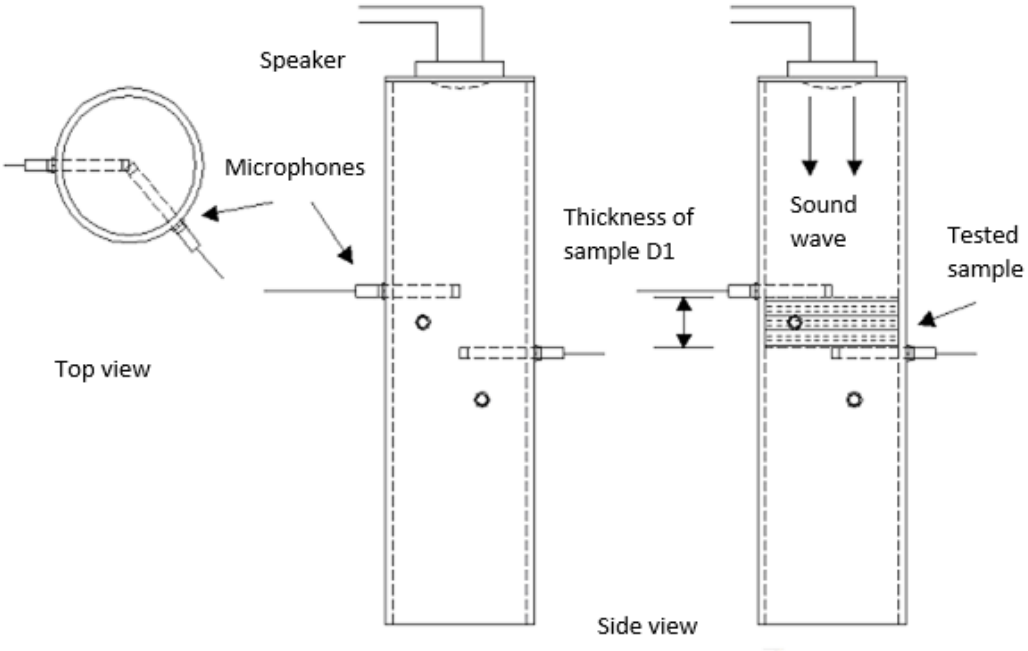

Figure 3.20. Schematic representation of the tortuosity equipment measurements

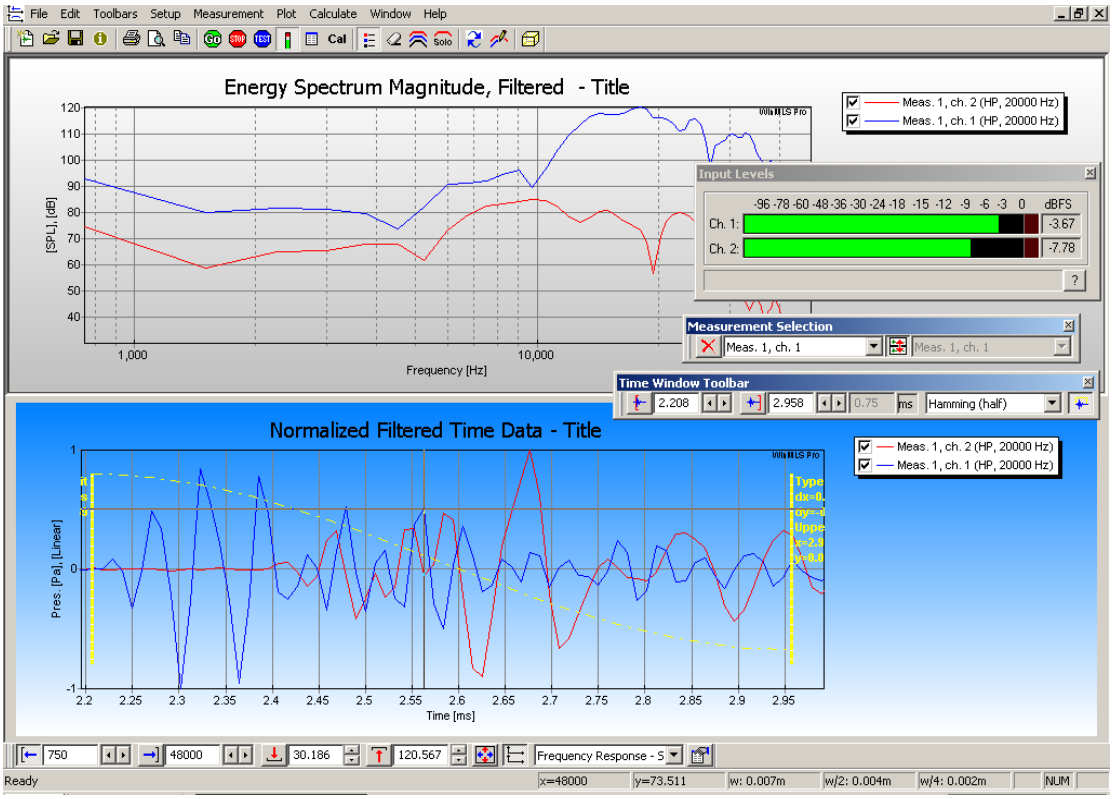

Figure 3.21. Typical result measured by WinMLS

Table 3-4. The measured tortuosity data for sample A which produced by 1.4-1.5 mm grain diameter.

time, t1(ms)	time, t2(ms)	time interval(ms)	tortuosity
2.563	2.646	0.083	1.09

Table 3-5. The measured tortuosity data for sample B which produced by 1.4-1.5 + <0.5 mm grain diameter.

time, t1(ms)	time, t2(ms)	time interval(ms)	tortuosity
2.396	2.49	0.094	1.23

3.5 Acoustic Properties Measurements

As acoustic insulation is at the heart of this research, the acoustic properties of the materials designed (cavity wall insulation, under-layer insulation and pipe insulation) formed an important part of the research. In terms of acoustic performance, sound absorption, transmission and impact sound insulation are the primary properties, measured as described below following international standards.

3.5.1 Sound Absorption and Transmission Measurement

Following ISO 10534 standard, airborne transmission loss was measured using an improved version of the impedance tube and two microphones method, using 4 microphones instead. As shown in Figure 3-23 and 3-24, the rig consisted of an 82 mm inner diameter impedance tube with a speaker lying in one end, driven by a Bruel and Kjear type 2706 amplifier and four ¼ “Bruel and Kjear type 2670 microphones fixed at a distance 60 mm and 105 mm each side of the tested sample Figures 3.25 and 3.26. To ensure that no leak in the sample occurred, sealing rings were in the gap between the wall of the tube and the edges of the sample. Also, adhesive putty was used around the gap where the microphone was mounted.

In the experiments, a random broadband signal between 0 and 2000 Hz was generated by a loudspeaker which was located at one end of the impedance tube. This sound wave propagates within the tube; some of this wave is reflected off the sample and the remaining parts of the wave (the propagating, reflecting and penetrating sound on the sample) are recorded by the microphones. In order to measure the sound absorption coefficient and the airborne transmission loss,

two such experiments were carried out, one with the impedance tube end open (absorption) and one with the end closed (transmission) as shown in Figure 3.22. To reduce the error in the closed-end experiments, a thick layer of wool fibers is used to absorb the sound and prevent it from being reflected.

Note that a single microphone was used to measure the broadband signal at each microphone port. This eliminated the need for calibration of the microphones at each location on the tube. Four microphone ports were utilized during the experiments and the same microphone probe was used to measure the signal at each location sequentially. Signals recorded at these channels were then analysed to determine the absorption coefficient of the sample tested. Since there were four channels, there were eight readings in total, four for the open-ended condition and four for the closed-ended condition.

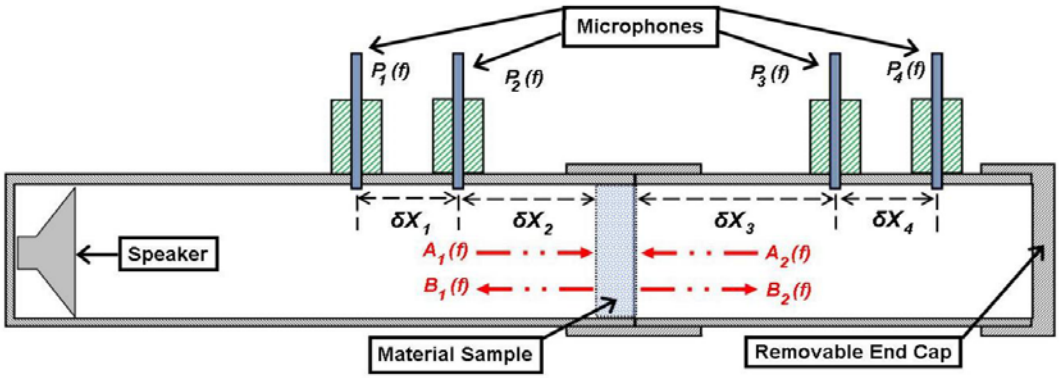

Figure 3.22. Schematic diagram of the modified impedance tube method.

Figure 3.23. Photograph of modified impedance tube rig.

Figure 3.24. Conditioning amplifier

Figure 3.25. Power amplifier.

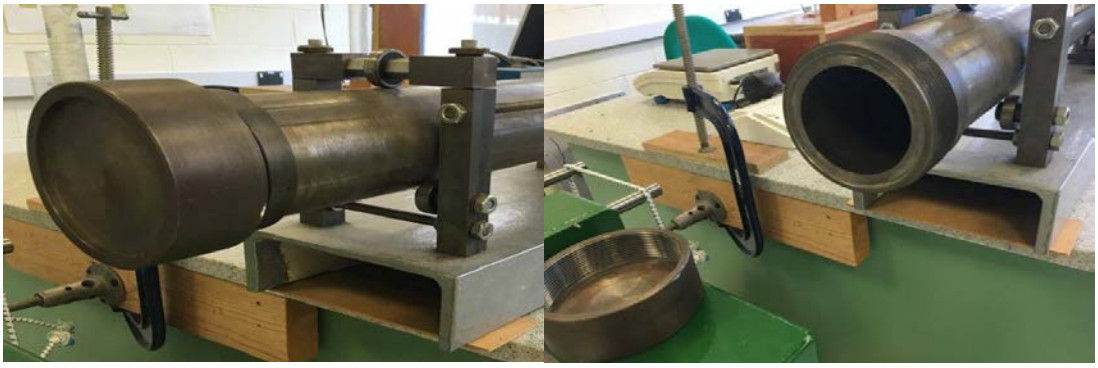

Figure 3.26. Closed and open end transmission loss test.

3.5.2 Impact Sound Insulation Measurement on Flat layers

The method used for the measurement of the impact sound insulation follows that described in the ISO 140 Part 8, and Building Regulation Approved but was implemented on a smaller scale test rig Figures 3.27 and 3.28 using only one impact hammer dropped manually at several (8) positions distributed uniformly across the specimen which was attached to a section of timber floor clamped onto a concrete slab.

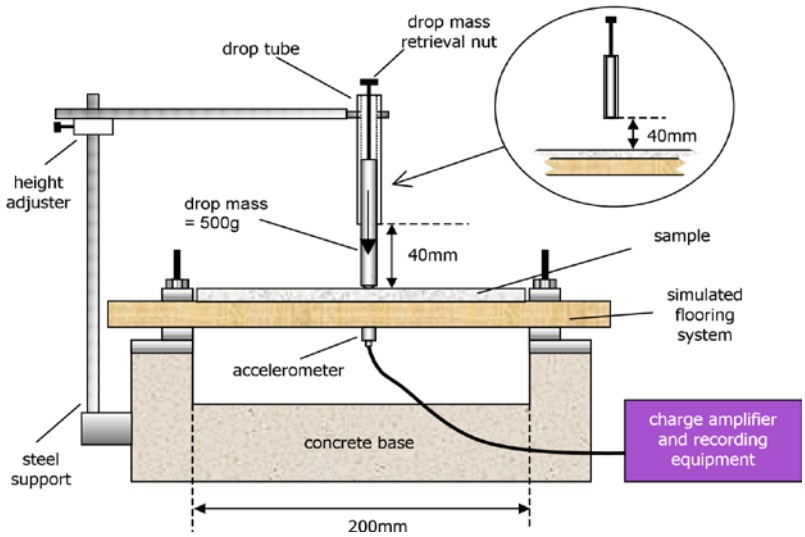

Figure 3.27. Schematic diagram of the impact transmission rig.

The scale of the rig allowed for a number of tests to be carried out quickly without compromising the accuracy of the measurement of E_d. In terms of sizes, test specimen were 200 mm x 144 mm, fixed on a 400 mm x 144 mm wood plan of thickness 18mm thick Figure 3.29. The brass cylinder weighed 500 g and was placed inside a tube and dropped from 40 mm height on the specimen. The presumption made here is that the sound pressure level resulting from the cylinder impact is directly proportional to the corresponding level of the floor

acceleration so that the need for an expensive reverberation chamber and a large area of the material surface was avoided.

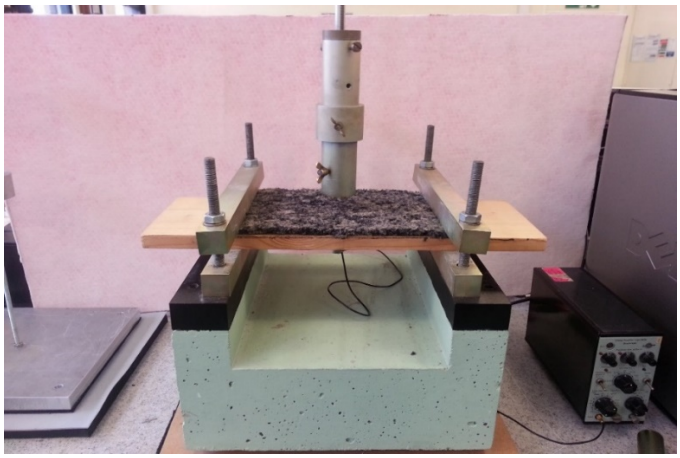

Figure 3.28. Photograph for impact transmission rig.

Figure 3.29. Accelerometer calibrator (Bruel & Kjaer Type 4291).

The level of vibrations caused by the hammer impact on the specimen and on the bare timber was measured by an accelerometer attached underside of the wood plan the signal of which was conditioned using a Bruel & Kjaer Type 2635 charge amplifier and recorded on a PC. Prior to the experiments, the accelerometer was calibrated using a standard calibrator (Bruel & Kjaer Type 4291), as shown in Figure 3.30.

The sensitivity of the charge amplifier was set to 31.6 mV/unit during the calibration.

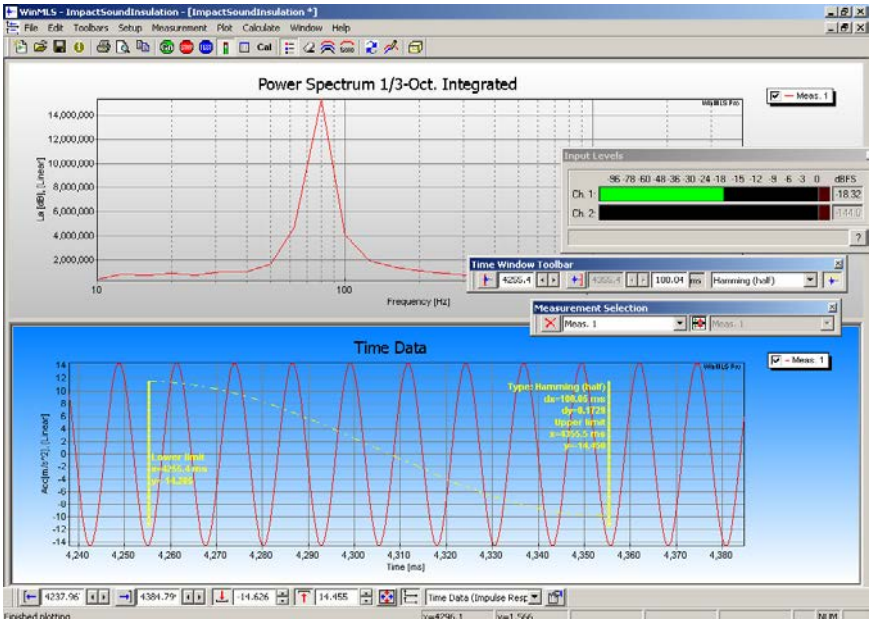

Figure 3.30. Typical accelerometer calibration results in WinMLS.

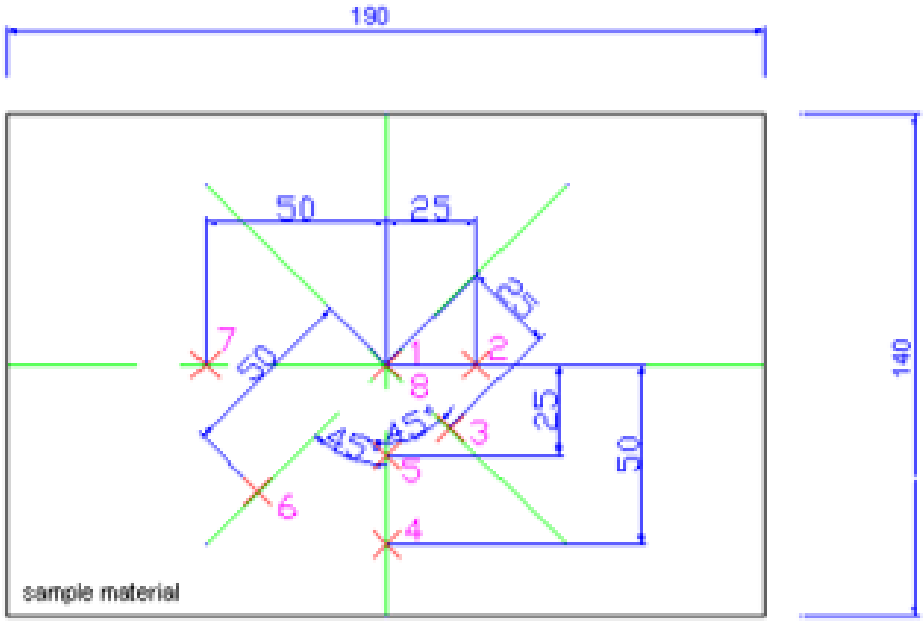

Figure 3.31. Positions for drop mass.

In order to obtain a spatial average of the impact acceleration, 8 different positions were chosen on the material sample at which the impact was accurately administered (see figure 3.32). In order to obtain a time average two drops at each of the eight positions were applied within 14 seconds for each position point.

The octave band acceleration level versus the frequency for the signal re-coded between the two selected points was then determined, related to the absolute reference acceleration level of 1g and the results of the analysis were graphically presented. The length of the time window used for the Fourier analysis was set to 100 milliseconds. By comparing the octave band acceleration levels between different material samples, the difference in impact sound insulation performance could be established. Figure 3.32 presents a typical screen image for the measured spectrum of the acceleration level and corresponding time history of two impact events.

Values of vibration according to different frequencies will explain clearly the performance of each formula as a sound and vibration insulation. The thickness of test specimen is important in this test, therefore, using the same thickness for all specimens will give accurate results to compare the performance of the different formula. Measuring the average of five points of each sample two or three times will give a more accurate result for this sample.

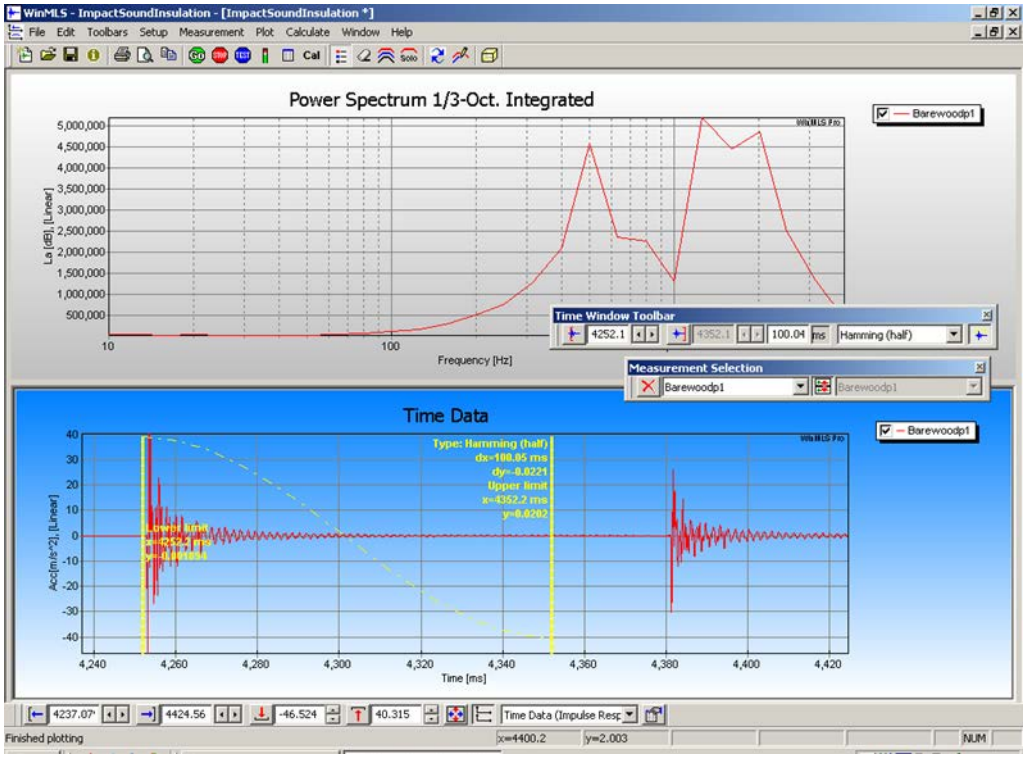

Figure 3.32. The corresponding narrowband spectrum and (b) the time series for the acceleration level.

3.5.3 Novel technique to measure insertion loss performance of pipe cladding

According to BS ISO 15665:2003 standard, insertion loss of pipe insulation is measured in a reverberation room using very long section of pipes, as long as 6m for a pipe of outer diameter 300mm and a wall thickness of 6mm. A sound source has to be fixed outside the reverberation room and should be connected to the test pipe. Figure 3.33 and figure 3.34 give pertinent details of this standard approach. Clearly, this is a tough requirement making the test very costly. In this research, a new, simpler and cheaper method that dispenses with a reverberation room and uses a short section of pipe 300mm was developed. The results as described in the Results section compare very well with measurements using BS ISO 15665:2003 standard.

Table 3-6. Minimum insertion loss required for each class according to ISO 15665:2003.

Class	Nominal pipe diameter D mm		Octave band centre frequency, Hz						
			125	250	500	1 000	2 000	4 000	8 000
	lower limit	upper limit	Minimum insertion loss, dB						
A1		< 300	- 4	- 4	2	9	16	22	29
A2	≥ 300	< 650	- 4	- 4	2	9	16	22	29
A3	≥ 650	< 1 000	- 4	2	7	13	19	24	30
B1		< 300	- 9	- 3	3	11	19	27	35
B2	≥ 300	< 650	- 9	- 3	6	15	24	33	42
B3	≥ 650	< 1 000	- 7	2	11	20	29	36	42
C1		< 300	- 5	- 1	11	23	34	38	42
C2	≥ 300	< 650	- 7	4	14	24	34	38	42
C3	≥ 650	< 1 000	1	9	17	26	34	38	42

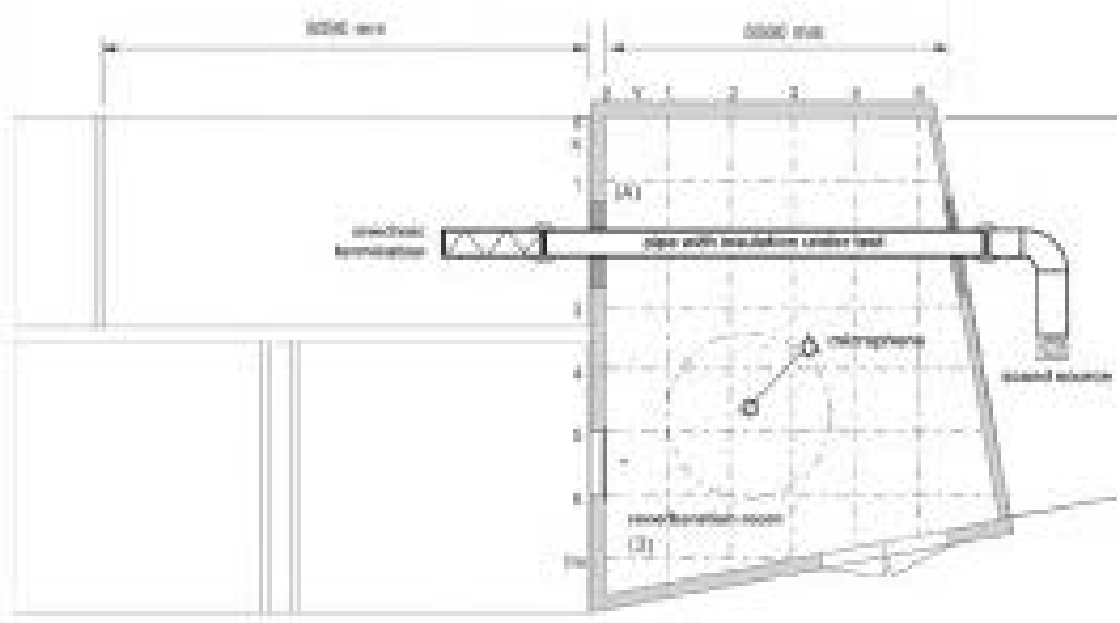

Figure 3.33. Pipe insulation performance measurement set-up according to ISO 15665:2003.

Figure 3.34. Photograph of pipe insulation performance test inside the reverberation room according to ISO 15665:2003.

3.5.3.1 The new set up

It is described in Figure 3.35 and uses a short section of a stainless steel pipe (303 mm long) of inner diameter 314 mm and thickness 4.7 mm to which the insulation is fixed using a double-sided adhesive tape. The insulated pipe is then suspended from a steel frame using a set of elastic bands. To the pipe section just described, vibrations were induced using a manually activated small brass pendulum, which was suspended on a hinge attached to a bar. The bar was mechanically isolated from the mechanical frame and from the pipe.

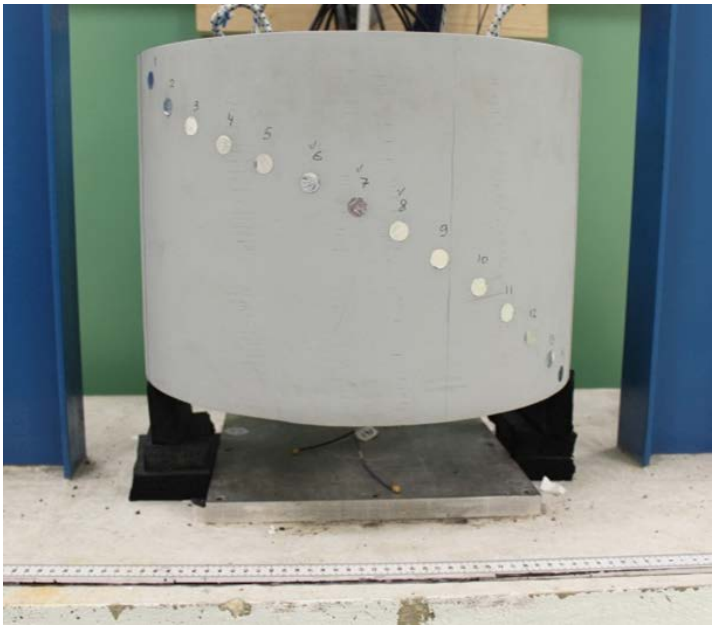

Figure 3.35. The 14 measurement points on the outer skin of the insulation system.

The impact point was on the inner side of the wall and approximately 110mm below the top rim of the wall. Two Bruel & Kjear Type 4514 accelerometers were attached to the internal surface of the pipe, opposite the point of impact at 180 mm and 280 mm below the top rim of the pipe, respectively. An Ometron VH-1000-D laser vibrometer was used to measure the vibration of the outer skin of the insulation system.

The measurement was taken at 14 positions which were arranged along the outer surface of the acoustic insulation layer in a diagonal fashion as shown in Figure 3.36. The accelerometers and the laser vibrometer were calibrated to 1 *g* using a B&K Accelerometer Calibrator Type 4291. The vibration data were recorded at a sampling rate of 22050 Hz in WinMLS software running on a PC with a Marc-8 sound card. The acceleration signals received from the two reference accelerometers were integrated using a standard cumulative

integration rule to allow for a comparison with the vibration velocity signal recorded with the laser vibrometer.

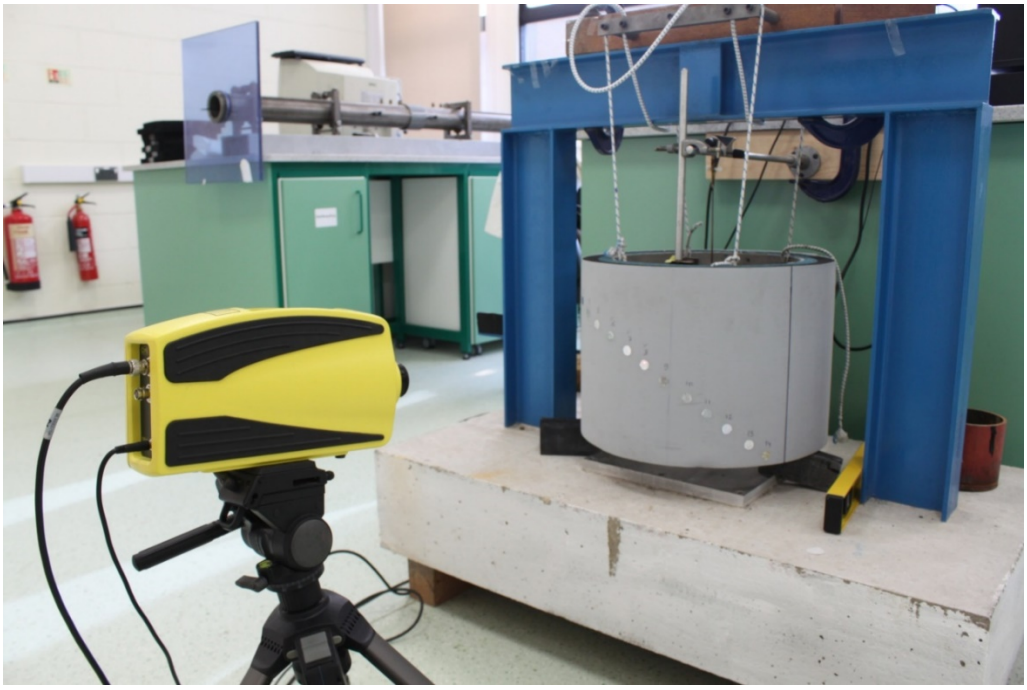

Figure 3.36. The experimental setup for the pipe insulation experiment.

Figure 3.37 presents an example of the vibration velocity data generated by a pendulum impact.

The vibration velocity data recorded in the time domain were transformed into the frequency domain using the 16384-point fast Fourier transform. The 14 narrow band spectra recorded with the laser vibrometer were averaged to obtain the mean spectrum of the vibration velocity of the outer insulation skin, V . The velocity spectra recorded with the two accelerometers were also averaged to determine the mean vibration velocity of the inner wall of the pipe, $\tilde{V}$. The mean narrow band spectra were converted to octave bands and used to calculate the octave band transmission loss (TL_n), which was predicted by:

$$TL_n = 20Log\frac{\tilde{V}_n}{V_n} \quad (3.9)$$

where; $\tilde{V}_n$ and V_n velocities on the inner pipe wall and the outer wall of the insulation system, respectively. The result from equation (3-1) was compared against the result of the standard insulation test performed on insulation System B in accordance with ISO 15665 [2] and against the result of the finite element modelling.

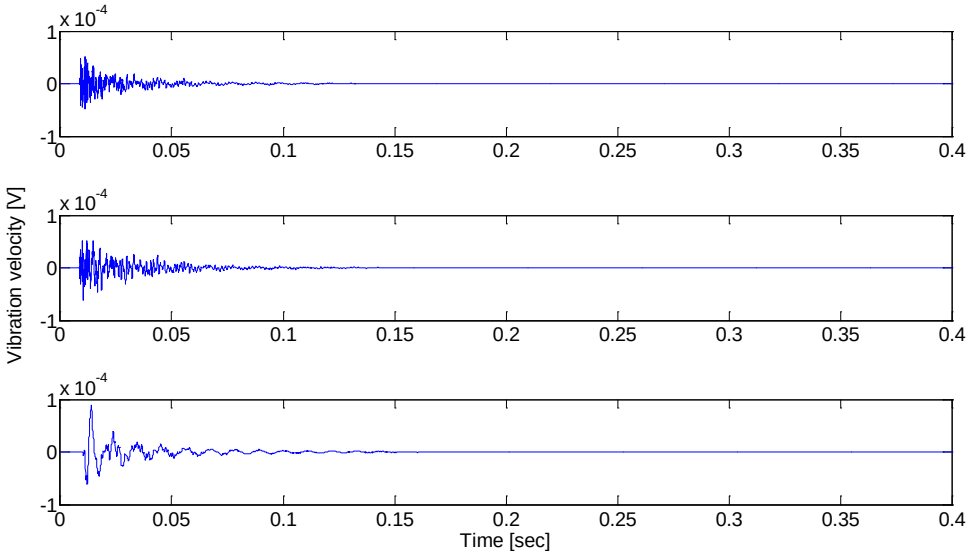

Figure 3.37. The vibration velocity associated with a pendulum impact: top accelerometer- top graph, bottom accelerometer- middle graph, laser vibrometer- bottom graph.

3.5.3.2 Calibration and Check against ISO 15665

The data collected using the above method was checked against the calibrated data obtained using ISO15665 performed on a calibrated sample consisting of 3 layers supplied by Armacell Ltd. These 3 layers were composed

of a 25 mm layer of closed Armaflex, the first layer on the pipe followed by two successive layers, a 25mm open cell Arma-Sound foam and a 2mm layer Arma-Check heavy barrier layer glued one on top of the other using Armaflex adhesive 520.

3.5.3.3 Finite Element Method

In comsol multiphysics the mechanical module has been selected to develop a finite element model of a short pipe section with three insulation layers, the model predicts the transmission loss for the pipe section.This mathmatical simulation has been build around the Nevair- Stokes equation as shown below:

$$\rho\left(\frac{\partial u}{\partial t}+u.\nabla u\right)=-\nabla p+\nabla.\left[\mu(\nabla u+(\nabla u)^{T})-\frac{2}{3}\mu(\nabla.u)I\right]+F \qquad (3.10)$$

where; u is the fluid velocity,

P is the fluid pressure.

ρ is the fluid density

μ is the fluid dynamic viscosity

$\rho\left(\frac{\partial u}{\partial t}+u.\nabla u\right)$ is the inertial forces

$-\nabla p$ is the pressure forces

$\nabla.\left[\mu(\nabla u+(\nabla u)^{T})-\frac{2}{3}\mu(\nabla.u)I\right]$ is the viscous forces

And by applying the equation of motion:

$$\frac{\partial \rho}{\partial t}+\nabla.(\rho u)=0 \qquad (3.11)$$

Hook's law has been applied, which is related to the stress tensor and the elastic strain tensor as shown in equation.

$$\sigma = \sigma_{ex} + C : \varepsilon_{el} = \sigma_{ex} + C : (\varepsilon - \varepsilon_{inel}) \tag{3.12}$$

where; C is the 4th order *elasticity tensor*,

":" stands for the double-dot tensor product (or double contraction).

The elastic strain ε_{el} is the difference between the total strain ε and all inelastic strains ε_{inel}.

There may also be an extra stress contribution σ_{ex} with contributions from initial stresses and viscoelastic stresses. In case of geometric nonlinearity, the second Piola Kirchhoff stress tensor and the Green-Lagrange strain tensor are used.

The elastic strain energy density is

$$W_s = \frac{1}{2}\varepsilon_{el} : (C : \varepsilon_{el} + 2\sigma_0) = \frac{1}{2}\varepsilon_{el} : (\sigma + \sigma_0) \tag{3.13}$$

This expression assumes that the initial stress contribution is constant during the straining of the material.

Loss factor damping is only applicable in frequency domain. When using loss factor damping, a complex constitutive matrix is used. With an isotropic loss factor η_s , this means that

$$D^c = (1 + j\,\eta_s)\,D \tag{3.14}$$

where; D is the constitutive matrix computed from the material data.

D^c is the complex constitutive matrix used when computing the stresses.

For a linear elastic material, this would be equivalent to multiplying Young's modulus by the factor $(1+\eta_s)$. For a nonlinear elastic material, this applies to the tangential stiffness.

It is also possible to give individual loss factors for each entry in the constitutive matrix, so that

$$D^c_{mn} = (1 + j\,\eta_s\,, mn)\, D_{mn} \qquad (3.15)$$

In the case of an orthotropic material, yet another option is available, where each individual component of Young's modulus and shear modulus can be given an individual loss coefficient:

$$E_m{}^c = (1 + j\eta_E, m)E_m$$

$$G_m{}^c = (1 + j\,\eta_G, m)G_m$$

where;, m = 1, 2, 3.

The complex moduli are then used to form the constitutive matrix.

For hyperelastic materials, the loss information appears as a multiplier in the strain energy density, and thus in the second Piola-Kirchhoff stress:

$$S = (1 + j\eta_s)\frac{\partial W_s}{E} \qquad (3.16)$$

For loss factor damping, the following definition is used for the elastic part of the entropy:

$$S_{elast} = \alpha : (s - j\,\eta_s)(C : \varepsilon) \qquad (3.17)$$

note that S_{elast} here denotes the entropy contribution and not any stress. This is because the entropy is a function of state and thus independent of the strain rate, while the damping represents the rate-dependent effects in the material (for example, viscous or viscoelastic effects). The internal work of such inelastic forces averaged over the time period 2π/ω can be computed as:

$$Q_h = \frac{1}{2}\,\omega\eta s\,\text{Real}(\varepsilon : \text{Conj}(C : \varepsilon)) \tag{3.18}$$

Q_h can be used as a heat source for modelling of the heat generation in vibrating structures, when coupled with the frequency-domain analysis for the stresses and strains.

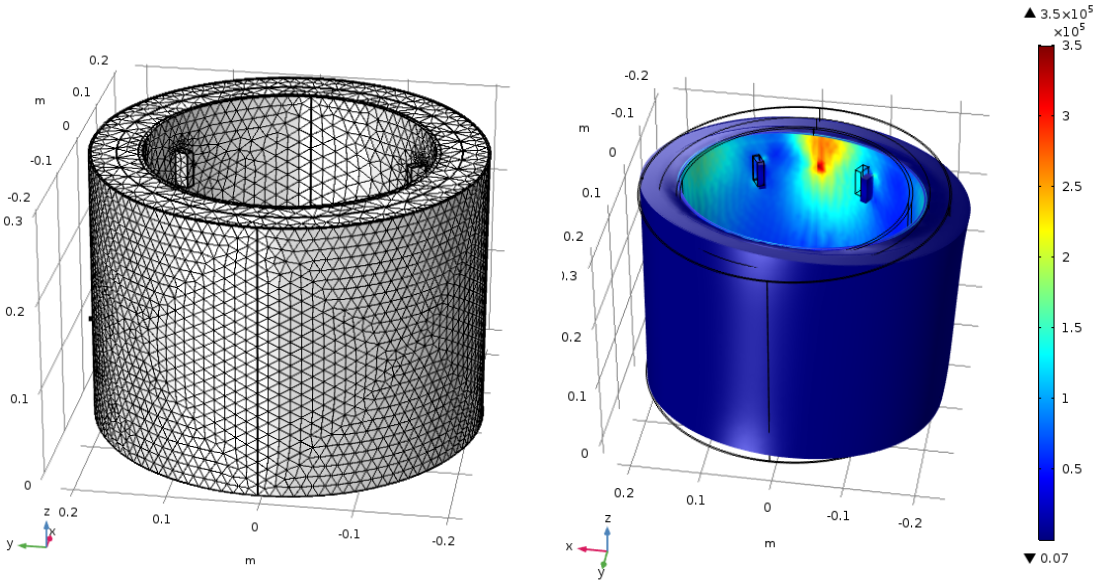

(a) (b)

Figure 3.38. 3D geometry of short pipe section, (a) mesh and (b) stress profile of impact applied on the internal surface of the pipe.

3.6 Thermal Insulation Measurement

3.6.1 Principle

As stated in the introductory chapter, evaluation of the thermal insulation of the new materials developed formed an important objective of this research. Thus their thermal conductivities were measured using the method described below.

The design of the instrument and procedure for determining the thermal conductivity were chosen in accordance with BS 1902–5.8 (1992). This standard is based on the split column principle and is recommended for testing shaped refractory materials with thermal conductivities in the range 3 to 80 W/m.K at a mean temperature in the range 300 to 850^{o}C. The standard was adapted to measure thermal conductivities above that of vermiculite (30 mW/mK) at temperatures in the range of 75 to 150^{o}C. Thus, the steel blocks suggested in BS 1902-5.8 were replaced with two aluminum cylinders to increase the thermal conductivity and the resultant heat flux to and from the test sample. Because of the limited (5-10mm) thickness of a typical sample used in this test it was found impractical to use a thermocouple pair inserted in the sample. Instead, the temperature difference was determined using a pair of thermocouples installed in the bottom and top blocks in the general vicinity of the sample surface. The distance from the centres of these thermocouples to the sample surface was 10mm. This method is not exact but provides a good relative estimate of the thermal conductivity of the samples prepared.

The thermal conductivity (coefficient of thermal conductivity) of the material by its definition is the rate of the linear heat flow, under a constant state

temperature condition, through a unit area of the test sample, per unit temperature gradient, in a direction perpendicular to the tested area. According to the split column method, the thermal conductivity of the tested piece is calculated in two steps.

Firstly, the heat flux, q (Watts), through the aluminum cylinders is determined from:

$$q = \lambda_{alu} \times \Delta T_m \times A / d \tag{3.19}$$

- λ_{alu} is the thermal conductivity of aluminum (Watts/m K)
- ΔT_m is the mean temperature difference between thermocouples (K)
- A is the cross-sectional area of the aluminum cylinder (in m^2)
- d is the distance between these thermocouples (m).

Secondly, the thermal conductivity of the test piece is calculated from:

$$\lambda = q_{alu} \times t / (A \times \Delta T) \tag{3.20}$$

- ΔT is a temperature difference of sensor 3 and 4 (in K).
- t is the sample thickness (in m).

As with regard to accuracy, testing low conductivity materials with a low melt index (approximately to 150ºC) have certain limitations. Firstly, the temperature in the aluminum cylinders should be well below the melt/combustion temperature of the material sample. The reduced heat flux through the sample between the bottom and the top cylinders results in the reduced accuracy of the

measured data. As a result, the measured value of the thermal conductivity is affected by a combination of external factors such as the thermal losses through the vermiculite insulation, finite conductivity of aluminum and the errors in the measured temperature gradient between the top cool and bottom hot aluminum cylinders. The accuracy can be improved if the temperature gradient between the blocks is increased. However, this would require an increase in the temperature of the hot block which can result in melting/charring of the material sample if the temperature is raised above the melt/combustion point. Alternatively, the temperature of the top block can be reduced, but this would require an expensive low-temperature cooling system which can be difficult to install and control.

3.6.2 Set-up

The experimental setup used in this work is presented in Figure 3.38. The instrument consists of an aluminum cylindrical column split into three parts. The bottom aluminum cylindrical column is 100mm in diameter and 150mm in length. Four 125mm long heaters are permanently installed in the aluminum column in the direction perpendicular to the top surface.

The diameter of the heating element is about 12.5 mm and the power rating of each heating element is 500 W. These heaters are electronically controlled and supplied with 230Volt AC. A thermal sensor (PT100) which is placed 10 mm below its top surface is used to control the temperature of the heater through the electronic control unit (see figure 3.39).

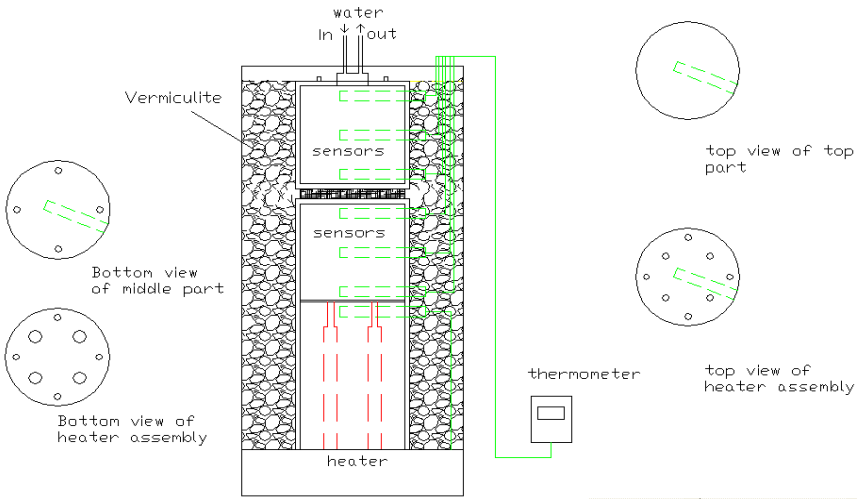

Figure 3.39. Schematic diagram of thermal conductivity apparatus with cylinders views.

In the middle and top aluminum cylindrical column, three thermal sensors (PT100) are positioned parallel to the top surface with centre spacing 40 mm to each other and 10mm to the edges. The middle cylindrical column is 100mm in diameter and 100mm in length, with a ground flat smooth finish top surface, see figure 3.40.

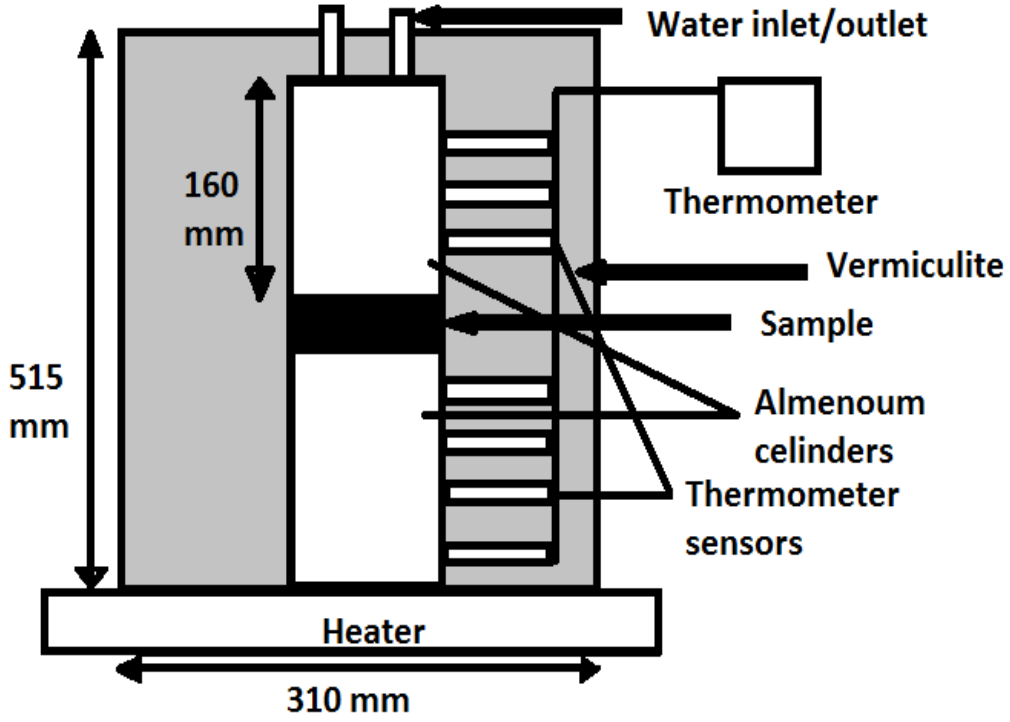

Figure 3.40. Schematic diagram of the thermal rig.

Figure 3.41. The overall look of the structure of the thermal conductivity measurement equipment.

The platinum resistance thermometer is used as the thermal sensor in the thermal conductivity measurement setup. Platinum wire-wound detectors include a pure platinum wire wound into a small spiral and located within axial holes in a high purity alumina rod. The detectors give good long-term stability and wide operating temperature range of -200 to 800^{o}C with an accuracy of 0.1^{o}C. The code number of the wire wound detector is PT100, with a 2.8mm diameter and 25mm in length in cylindrical shaped. The tolerance class of the detector is 1/10.

3.6.3 Measurement Procedure

Before the measurement started, the thermal measurement equipment was required to warm up. The heater which is positioned at the bottom of the equipment was required to preheat to the required maximum temperature. The top aluminum cylinder is placed directly on the top surface of the middle cylinder and left in this position until the temperature of thermal sensor no. 4 in the top cylinder is the range between 40 to 45^{o}C. At this point the tested sample can be inserted between the middle and top cylindrical columns, i.e. between thermal sensors 3 and 4 (see figure 3.40). If necessary, a special paste is applied to the top and bottom surfaces of the tested material sample to ensure good thermal contact between the sample and the aluminum cylinders.

The cooling water supply is turned on so that the temperature of the upper part of the top cylinder is controlled within 10-18^{o}C. Finally, expanded vermiculite is loaded around the cylindrical column to reduce the heat loss due to air convection. Vermiculite Premium Horticultural Grade, the insulation material that used around aluminium cylinders in this test, is a member of the phyllosilicate

group of minerals, resembling mica in appearance and it is characterised by a very low value of thermal conductivity of 58 mW/mK.

3.6.4 Calibration and accuracy

Some materials such as wood and PVC with known values of thermal conductivity have been tested, and the measured data were compared with those provided in the textbook. Specifically, the measured thermal conductivity of the 19mm thickness wooden sample is 0.129 W/ mK. These compare closely with the reference value of the thermal conductivity of wood of between 0.15 (Oak) to 0.112 W/ mK (white pine). The result for a 9mm thick PVC sample is also close to its reference value: 0.155 W/mK (measured) 0.15-0.35 W/mK (Glicksman et al. 1987).

In order to obtain more accurate data for materials with very low thermal conductivity, some tests were repeated on the same sample at different times or with the different circumferential condition, i.e. with or without vermiculite surrounding the cylinder/specimen area during the experiment. Three particular samples (6BR3a, 50RB2c, and RB2b) have been tested repeatedly, and their thermal conductivity measured with the vermiculite insulation was found to be lower than without vermiculite. The result suggests that the vermiculite insulation is very effective in terms of the reduction of the unwanted heat loss through the air surrounding the experimental setup table 3-7. A detailed analysis of these data shows that the provision of the vermiculite insulation results in the 40-50% change in the measured value of the thermal conductivity which cannot be ignored.

The effect of the driving temperature on the measured value of the thermal conductivity was also investigated in a separate set of experiments. The driving

temperature of the heater was adjusted from 100^{o}C to 75^{o}C and 50^{o}C for sample GF3a. The experiments were conducted in the presence of vermiculite insulation. The thermal conductivity of the sample can fluctuate when the driving temperature was adjusted between 50^{o}C and 100^{o}C (table 3-8).

A 20% increase in the measured value of the thermal conductivity is observed if the driving temperature is reduced from 100^{o}C to 75^{o}C. A further reduction in the temperature does not seem to result in any significant change in the measured value of the thermal conductivity. One can argue that the accuracy of better than 20% is attained in this experiment. The thermal conductivity data are most repeatable in the case of sample RB2b for which the reproducibility in the experiments is the best.

Table 3-7. The effect of vermiculite insulation on the measured value of the thermal conductivity (w/mK).

Sample	With vermiculite	Without vermiculite
6BR3a	0.060	0.0930
50RB2c	0.0796	0.0945
RB2b	0.0798	0.1122

Table 3-8. The effect of driving temperature on the measured value of the thermal conductivity of GF3a Sample.

Driving temperature (^{o}C)	Thermal conductivity
100	0.0674
75	0.0811
50	0.0791

CHAPTER FOUR

RESULTS AND DISCUSSION

4.1 Introduction

Following from the aim and objectives to construct porous structures of designed cells and the experimental methodology to achieve this, the results of the experiments and underpin which have been presented here with theoretical predictions. This chapter follows naturally, organised into the construction of (i) random multi-size cells with an SBR non foaming binder, (ii) random multi-size cells with a PU foaming binder and the application of vacuum and (iii) stratified size cells with multi-layering.

As the theoretical underpinning forms an important part of the research (it tests the accuracy of the absorption data as explained later), it is introduced first to enable comparison with the sound absorption data. A brief overview of modelling of sound absorption was presented in the literature review. Here, more details are given leading to the widely used Johnson Champoux-Allard which served to test the accuracy of sound absorption data of the porous structures developed here.

4.2 Modelling of Sound Absorption in Porous Media

Even on a macroscopic level the description of sound propagation in a porous medium can be very complicated since sound not only propagate through the pores but also through the frame particularly in situations where the frame components are elastic as is the case in our situation with the rubber crumb, the

fibres and the binder all being elastomeric. In both the rigid and elastic frame situations, the sound propagating loses energy by (i) viscous dissipation and (ii) thermal dissipation. Thus in modelling sound absorption in complex porous systems such as the ones developed in this study, all these aspects must be accounted for.

A plausible description of a porous material is to consider it as an *equivalent fluid*. When the material is highly porous (porosity close to 1), further assumption may be assumed that this equivalent fluid has the same properties as the air in the porous media at the macroscopic scale. Thirdly, in such a system the dimensions of the pores will be small compared to the wavelengths of an incident sound. On the basis of these assumptions, models have been developed depending on the porous geometry is described. Raleigh (1894) started this modelling pursuit by considering the pores to be simply parallel cylinders held in a rigid frame with the one incident wave travelling longitudinally through them. The analysis in such a situation is simply in one phase, the fluid. Once the elasticity of the frame is considered, we see that the boundary will play a role and the analysis must consider simultaneously both the fluid and the elastic frame which will deform depending on the intensity of the incident wave. This coupled situation was first analysed by Biot (1956) who established that three waves occurred, one transversal and one longitudinal in the solid phase and one longitudinal in the fluid phase, thus establishing that the sound propagate both in the frame and in the fluid. Such observation is of course not surprising but its importance varies depending on the properties of the fluid and the solid and the geometry of the pores. Building on these models, several researchers followed, Zwikker and Kosten (1949), Attenborough (1983a), Lauriks (1989), Johnson et

al. (1987), Champoux and Stinson (1992), Allard (1993) and many others considering variations in the properties of this coupled problem.

Of all the models available, the one formulated by Allard (1993), Champoux and Stinson (1992) and Johnson et al.(1987) is the most widely used as (i) it uses parameters that have physical meaning (porosity, flow resistivity, tortuosity, characteristic viscous length or size of the connected pores, characteristic thermal length or a measure of the size of the largest pores) and are measurable; and (ii) it gives predictions that are in agreement with data for a large variety of porous materials (see assessment by Fellah et al.,(2004)). This model will be used in this study to test the validity of our sound absorption measurements using porosity, flow resistivity, tortuosity as determined in the previous chapter and the characteristic viscous and thermal lengths as will be shown below.

Here has been noted for completion of this overview on the modelling approach that there exists a semi-empirical approach devised by Delaney and Bazley (1970). These researchers have measured the wave number and the characteristic impedance of many porous fibrous media (porosity approaching 1) in a large range of frequencies and found that these depended mainly on the angular frequency ω and the flow resistivity σ of the material with good fit correlations as follows:

$$Z_c = \rho_0 C_0[1 + 0.0571X^{-0.754} - j0.087X^{-0.732}] \tag{4.1}$$

$$k = (\frac{\omega}{C_0})[1 + 0.978X^{-0.7} - j\ 0.189\ X^{-0.595}] \tag{4.2}$$

where; ρ_0 is the density of air and c_0 the speed of sound in air.

X= c_0 f/ σ is a dimensionless parameter combining air density, flow resistivity and frequency and it is in the range 0.01<X<1.

Clearly, this is a very simple empirical model which does not consider the complexity of our material systems. Besides fluid properties, this model only considers flow resistivity.

4.2.1 Johnson Champoux- Allard Model

As just explained, the model describes a coupled analysis, which of (1) the sound propagation in the fluid phase coupled with (2) the displacement of the elastic solid phase. As the sound propagation is simply a pressure wave propagation, the equations required are (a) a force balance or the equation of motion and (b) an equation of state for the fluid (air) or its compressibility. These equations are:

Equation of Motion and Pressure Wave Equation

$$\rho_{\circ} \frac{\partial \vec{v}(\omega, \vec{r})}{\partial t} = -\vec{\nabla} p(\omega, \vec{r}) \tag{4.3}$$

$$\frac{1}{K_a} \frac{\partial p}{\partial t} = -\vec{\nabla}.v \tag{4.4}$$

with ρ_0 and K_a being the air density and compressibility modulus, p the sound pressure and $\vec{v}$ the fluid velocity vector, both depending on position vector ($\vec{r}$) and sound frequency (ω). Both $\vec{v}$ and p will naturally depend on time (t) owing to their dependence on frequency. In keeping with the assumption of an equivalent fluid and the interaction with the frame holding the pores, the fluid will be

described by a complex effective density $\tilde{\rho}(\omega)$ and a complex effective bulk modulus $\widetilde{K}(\omega)$ with the wave equation expressed as:

$$\nabla^2 p(\omega,\vec{r}) = -\omega^2 \frac{\tilde{\rho}(\omega)}{\tilde{K}(\omega)} p(\omega,\vec{r}) = -k^2(\omega) p(\omega,\vec{r}) \tag{4.5}$$

with the wave number $k(\omega)$ defined as:

$$k(\omega) = \omega \sqrt{\frac{\tilde{\rho}(\omega)}{\tilde{K}(\omega)}} \tag{4.6}$$

The wave pressure can now be written simply as a function of the wave number as:

$$p(\vec{r}) = p(0,0,0) e^{-jk\vec{r}} \tag{4.7}$$

Inertia, Viscous and Thermal Interactions

For Eq. (4.3) to be complete, the effective density $\tilde{\rho}(\omega)$ must express inertial and viscous interaction and the bulk modulus $\widetilde{K}(\omega)$ thermal exchange between the fluid and the frame due to friction. If wave propagation has been assumed in the fluid phase only, Allard [1993] formulation could be used for the dynamic density:

$$\tilde{\rho}(\omega) = \propto_{\infty} \rho_{\circ} + \frac{\sigma\Omega}{j\omega} G(\omega) \tag{4.8}$$

Eq. (4.8) introduced three important material parameters, the tortuosity α_{∞} , the porosity Ω and the flow resistivity σ of the porous material and the function $G(\omega)$ which expresses the frequency dependency of the velocity profile. Following Johnson et al. [1987], $G(\omega)$ can be written as:

$$G(\omega) = \sqrt{1 + \frac{4j\alpha_\infty^2\ \eta\rho_\circ\omega}{\sigma^2\ \Lambda^2\ \Omega^2}} \tag{4.9}$$

where Λ is the characteristic viscous length which combines material parameters (tortuosity α_∞ , the porosity Ω , the flow resistivity σ and the pore shape c) and air viscosity η:

$$\Lambda = \frac{1}{c}\sqrt{\frac{8\alpha_\infty \eta}{\sigma\Omega}} \tag{4.10}$$

Now for the thermal interaction modulus $\widetilde{K}(\omega)$, following Champoux and Allard [1991], :

$$\widetilde{K}(\omega) = \frac{\gamma P_\circ}{\gamma - (\gamma - 1)\left[1 + \frac{8\eta}{j\Lambda'^2\ B^2\ \omega\rho_\circ} G'(\omega)\right]^{-1}} \tag{4.11}$$

$$G'(\omega) = \sqrt{1 + \frac{j\Lambda'^2\ B^2\rho_\circ\ \omega}{16\eta}} \tag{4.12}$$

This equation introduces the thermal characteristic length, Λ', which combines material parameters (tortuosity α_∞ , the porosity Ω, the flow resistivity σ and the pore shape c') and air viscosity η:

$$\Lambda' = \frac{1}{C'}\sqrt{\frac{8\alpha_\infty\ \eta}{\sigma\Omega}} \tag{4.13}$$

As noted by Johnson et al., [1987], the characteristic viscous length is always smaller than or equal to the characteristic thermal length, making $c' < c$

with larger pores contributing more to Λ' than smaller pores. Figure 4.1 depicts the relative magnitude of Λ and Λ' in a typical porous structure.

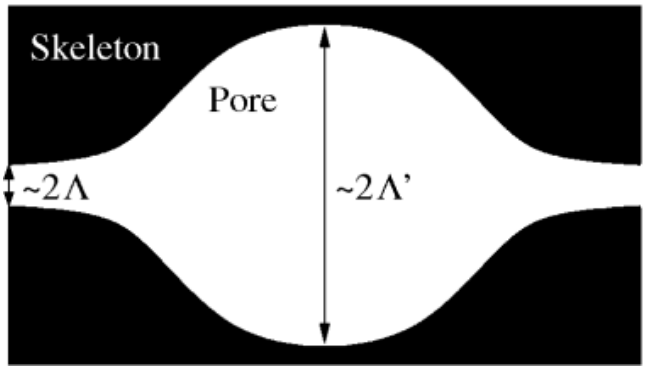

Figure 4.1. Schematic of a 2-Dimensional pore, the viscous characteristic length Λ, and the thermal characteristic length Λ'.

The influence of these two characteristics on the sound speed, attenuation and the impedance of the porous medium has been known for a long time and analytical forms have been developed to predict their frequency-dependent behaviour as a function of macroscopic parameters of the porous space (Zwikker and Kosten 1949), (Biot 1956) and (Attenborough 1985). It has been shown that the viscous friction losses in the oscillatory flow in a material pore of characteristic size s are controlled by the non-zero imaginary part of the dynamic density

$$\rho_b \cong \rho_0 + i\frac{\eta}{\omega s^2} \tag{4.14}$$

and are pronounced at frequencies below the so-called Biot frequency:

$$\omega_v = \frac{\eta}{S^2\,\rho_\circ\,\alpha_\infty} \tag{4.15}$$

Above this frequency, the viscous friction is relatively small and the inertial forces are predominant. Therefore, the value of this frequency is of importance as it separates the viscous and inertia regimes.

Similarly, the thermal losses are controlled by the non-zero imaginary part of the complex compressibility and are pronounced around the characteristic thermal frequency:

$$\omega_B = \frac{k}{S^2 \rho_\circ C_p} \tag{4.16}$$

where; k and Cp are the thermal conductivity and the specific heat of air. This frequency separates the isothermal (low-frequency, $C_b = P_o^{-1}$) and adiabatic (high-frequency, $C_b = (\gamma P_o)^{-1}$) regimes. There is a considerable amount of experimental evidence which confirms that the above assumptions are valid for the accurate prediction of the acoustic properties of a porous surface(Stinson 1991) and (Salissou and Panneton 2007).

4.2.2 Predicted Absorption coefficient

Following from this model equations (4.3-4.16), the absorption coefficient $\alpha(\omega_i)$ of a material backed by a rigid wall (such that would occur in an impedance tube when absorption is measured) is given at a given frequency ω_i as:

$$\alpha(\omega_i) = 1 - \left|\frac{Z(\omega_i) - 1}{Z(\omega_i) + 1}\right|^2 \tag{4.17}$$

where; $Z(\omega_i)$ is the surface impedance of a porous layer expressed in terms of Z_0 is the air characteristic impedance and the parameters defined earlier as:

$$Z(\omega_i) = j\frac{1}{\alpha Z_0}\sqrt{\rho_e(\omega)K_e(\omega)}\ \cot\left(\omega h\sqrt{\frac{\rho_e(\omega)}{K_e(\omega)}}\right) \qquad (4.18)$$

Model Solution

Having defined the model equations above, the procedure in principle is to input the parameters of the model and then find the absorption coefficient over the range of frequencies, low to high. As described by the above equation, 5 parameters were used: tortuosity, porosity, flow resistivity, thermal length and inertia-viscous length (α_∞ , Ω , σ , Λ and Λ' respectively). Whereas the first three parameters can be established from characterising the materials as was described in Chapter three, Λ and Λ' cannot. An alternative method of computation should be founded.

The most reliable method of computations is to approach the solution inversely: input the measured absorption coefficients, starting at the low frequency, and then extract these 5 parameters, then compare the 3 predicted materials parameters tortuosity, porosity and flow resistivity with those measured. As this model has been proven to hold from a number of studies (Panneton and Olny 2006) (Olny and Panneton 2008) and (Brouard et al. 1995) the fit between the predicted and measured tortuosity, porosity and flow resistivity will validate or not the data collected.

To perform this inverted mode of solution, we used a commercial program FOAM-X 2015 based on the Johnson Champoux- Allard model with adjustable 5 parameters in the range:

$$1 \leq \propto_{\infty} \leq 5$$

$$1\mu m \leq (\Lambda\,, \Lambda') \leq 2000\mu m$$

$$\Lambda \leq \Lambda'$$

$$1000\ N.s.m^{-4} \leq \sigma \leq 5 \times 10^{6}\ N.s.m^{-4}$$

$$0.7 \leq \ \alpha\ < 1$$

The procedure is described in the programme manual but basically the approach is to divide the input measured absorption coefficient function $\Omega(\omega_i)$ and divide it into 3 frequency zones (Z1, Z2 and Z3) from which are extracted in turn (Ω , σ , Λ'), (α_{∞} , σ , Λ) and (Ω , Λ , Λ') respectively as illustrated in Figure 4.2, the reason being that depending on the frequency range, the five parameters model effectively reduces to a three parameters model, the parameters being different in each zone.

In order to minimise errors, absorption curves from at least two material specimen were used.

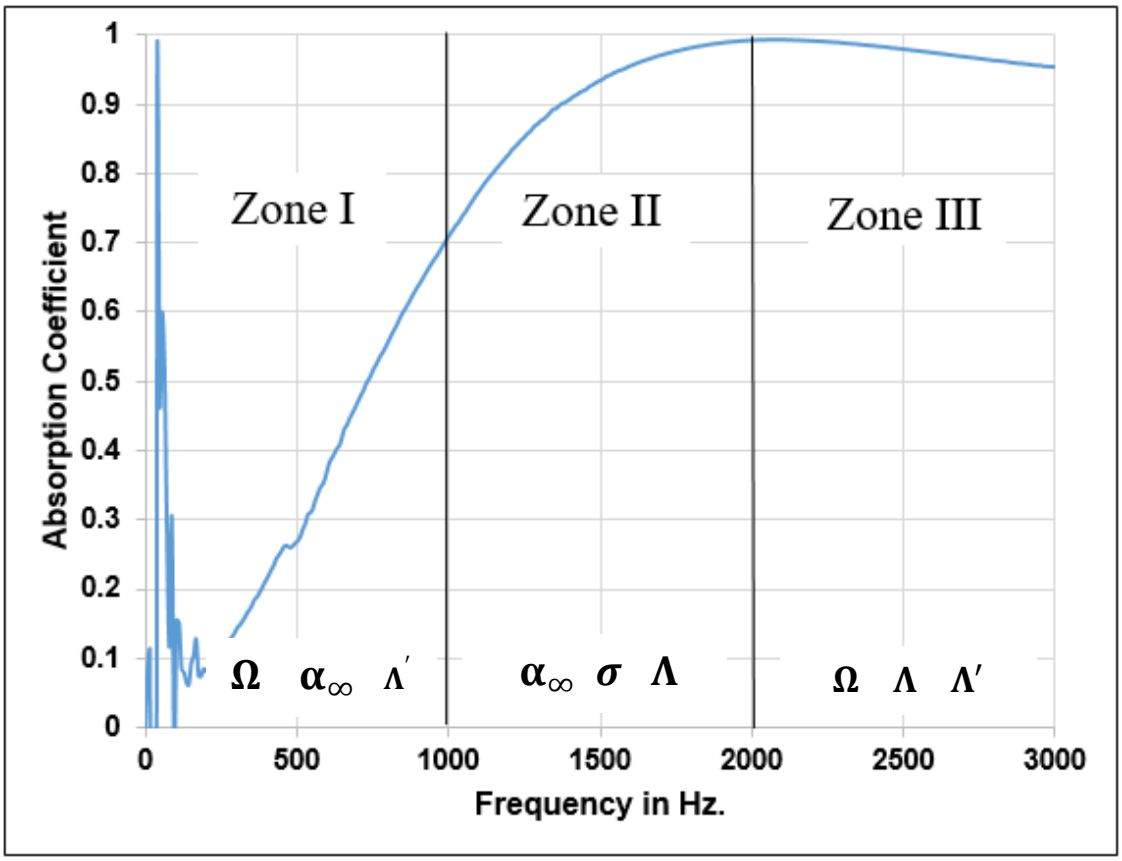

Figure 4.2. Frequency zones of a typical sound absorption coefficient with the main effecting parameters for each frequency zone.

4.2.3 Random Multi-Size Cells Porous Structuring with SBR binder

This construction as explained earlier is intended for under-layer sheets application and as such must achieve good impact sound and thermal insulation performance. As acoustic and thermal performances require different pore cell structures, open cells for acoustic and closed cells for heat insulation, an optimisation exercise is necessary to arrive at the best “recipes”. The main raw material used was tyre shred fibre residue (TSFR) from granulated tyres with fibre length ranging from 1mm to 60mm and fibre diameter in the range of 20–30μm. To this fibrous material was added the SBR non-foaming binder and tyre crumb

(TC) or bumper crumb (BC) of various particle sizes. The mix is thus complex and for a given quantity of the starting fibrous tyre shred, the performance will depend on the composition of the whole material system, i.e.:

- The initial amount of tyre shred fibrous residue
- The proportion of binder to this tyre shred fibrous residue
- The type and amount of rubber crumb added, tyre or bumper type
- The size of the crumb particulates
- The thickness of the material constructed (dictated implicitly by the above components).

The optimal composition was achieved on the basis of the following data.

4.3 Optimal SBR/TSFR ratio

Figure 4.3 presents the impact sound insulation data on samples taken from a 200g formed sheet 2cm thick x 20cm wide x 30cm long at SBR/TSFR ratio 20, 30, 40, 50 and 60% w/w. A comparison is made on this figure with wood and this shows the outstanding benefit of this material on impact sound insulation at all frequencies. The performance improves as the SBR/TSFR ratio with the best performance achieved at 20%. At the important frequency of 500 Hz, the impact sound insulation is 34dB going down with increasing frequency to 18dB AT 1000Hz. This suggest that inherently, the TSFR on its own is a good impact sound insulator as it might be expected from its fibrous nature. Binding it with a little SBR to form it into a sheet will produce a cheap, easy to install material.

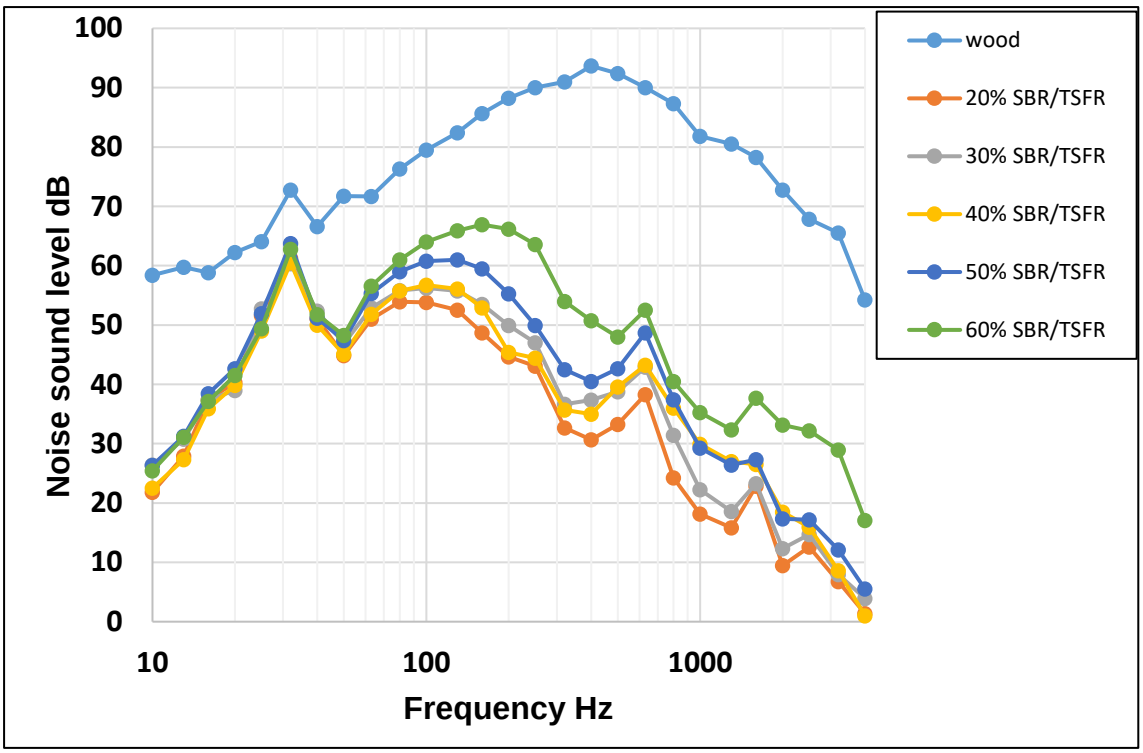

Figure 4.3. Effect of SBR/TSFR ratio on impact sound insulation.

Figure 4.3 shows also that impact sound insulation performance remains essential very good at SBR/TSFR ratio up to 40%. An increase SBR/TSFR ratio provides better material integrity which is always desirable when applying under-layer sheeting. There is a beak around 32 Hz. Frequency and this peak was very clear in all samples which means this frequency can represent the natural frequency of the system which means this is a resonance peak and has no relation with samples performance.

About thermal insulation, Figure 4.4 presents the heat insulation performance through the measured thermal conductivity. The trend in data shows a minimum at 40%, suggesting that at that binder loading closed porosity has been achieved. The shape of the curve in Figure 4.4 suggest that SBR addition first increases thermal conductivity. The explanation is that during mixing of the SBR into the

TSFR, the fibers at low SBR loading are merely coated and not binded together. Above 30%, binding that produces close cells kicks in, producing at 40% a significant number of closed cells, conducive to good thermal insulation. Above 40%, the closed cells begin to fill and the insulation drops, leading to increasing thermal conductivity.

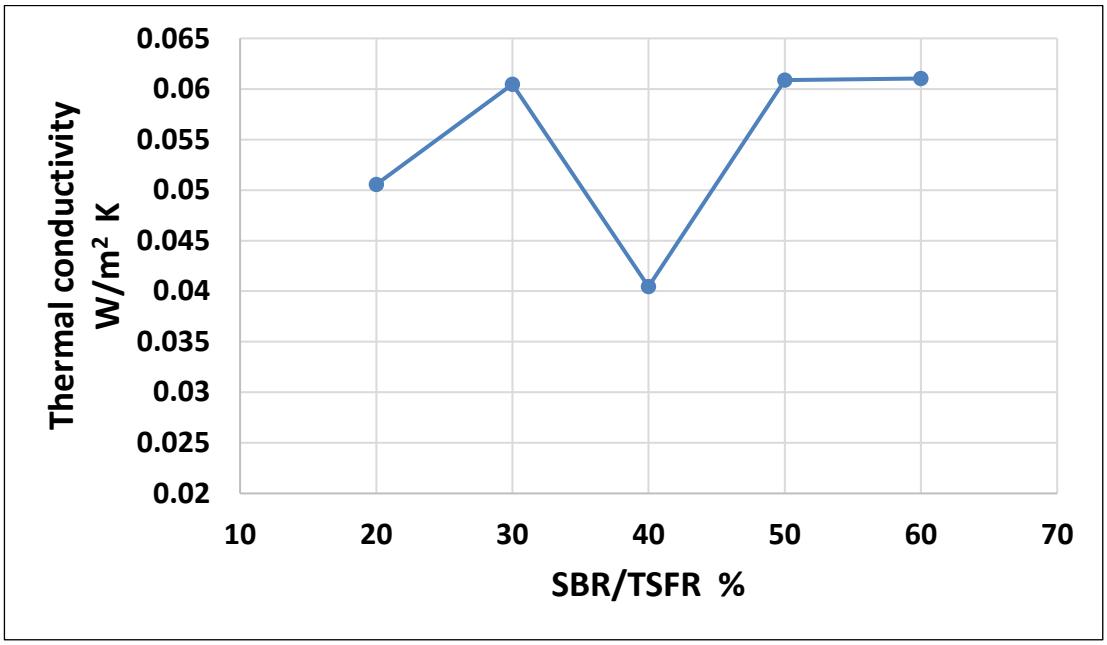

Figure 4.4. Effect of SBR/TSFR ratio on thermal conductivity.

As impact sound insulation is very good up to 40% SBR/TSFR ratio, on the basis of the data of Figures 4.3 and 4.4, 40% was retained as the optimum impact sound and thermal insulation loading.

4.3.1 Effect of crumb addition at optimal SBR/TSFR ratio

Having established an optimal SBR/TSFR ratio (40%), the next objective of the research was to assess what further improvement could be obtained with the addition of rubber crumb, either from tyres (TC) or bumpers (BC) and how the

particle size of these additives affect performance. The corresponding data are shown in Figures 4.5-4.7. The first observation that can be made is that BC addition is more effective and this is shown in the figures below complemented by the seven figures in Appendix A, (Figures A-1-A-7) depicting additions at 15, 22.5, 45, 52.5 and 60g loadings.

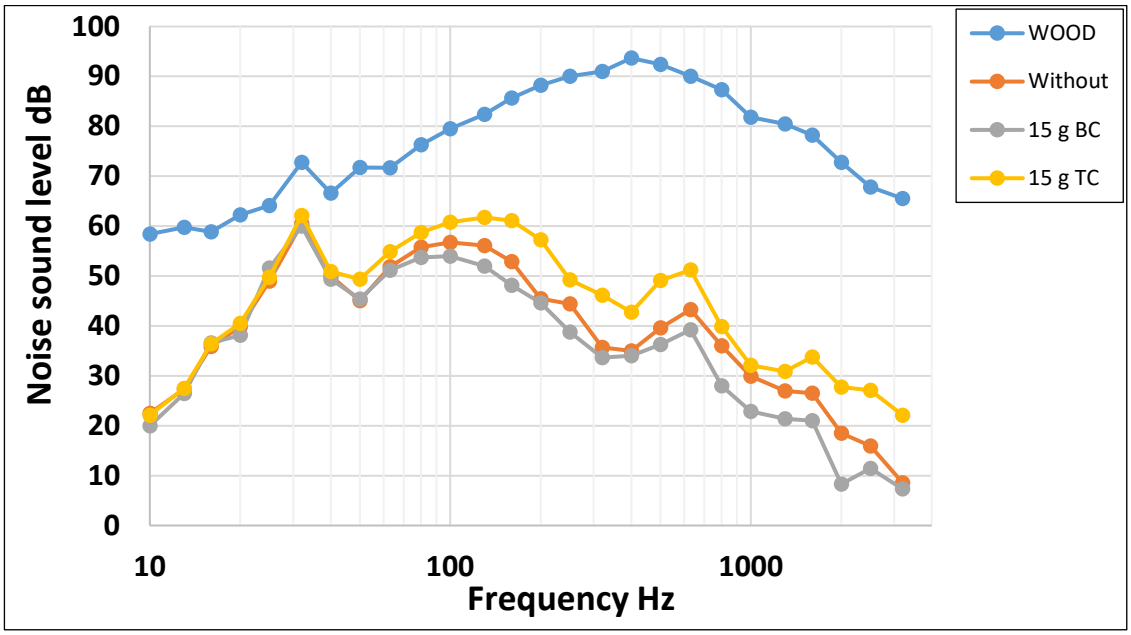

Figure 4.5. Effect of low loading BC addition on impact sound insulation.

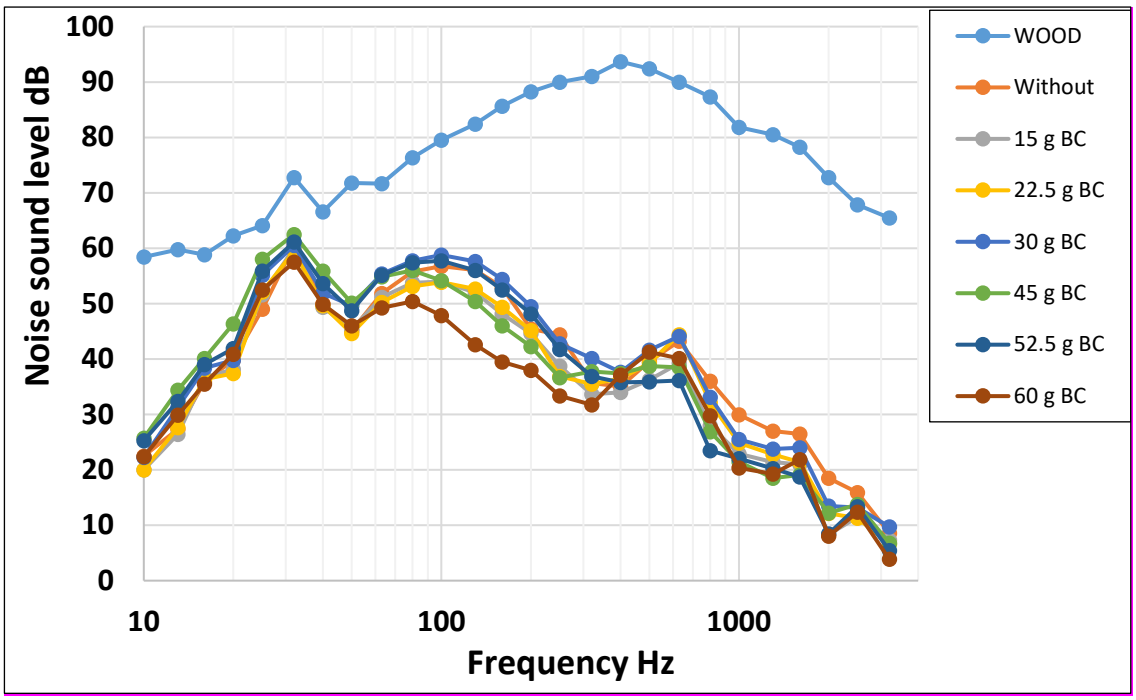

Figure 4.6. Effect of increased BC addition on impact sound insulation.

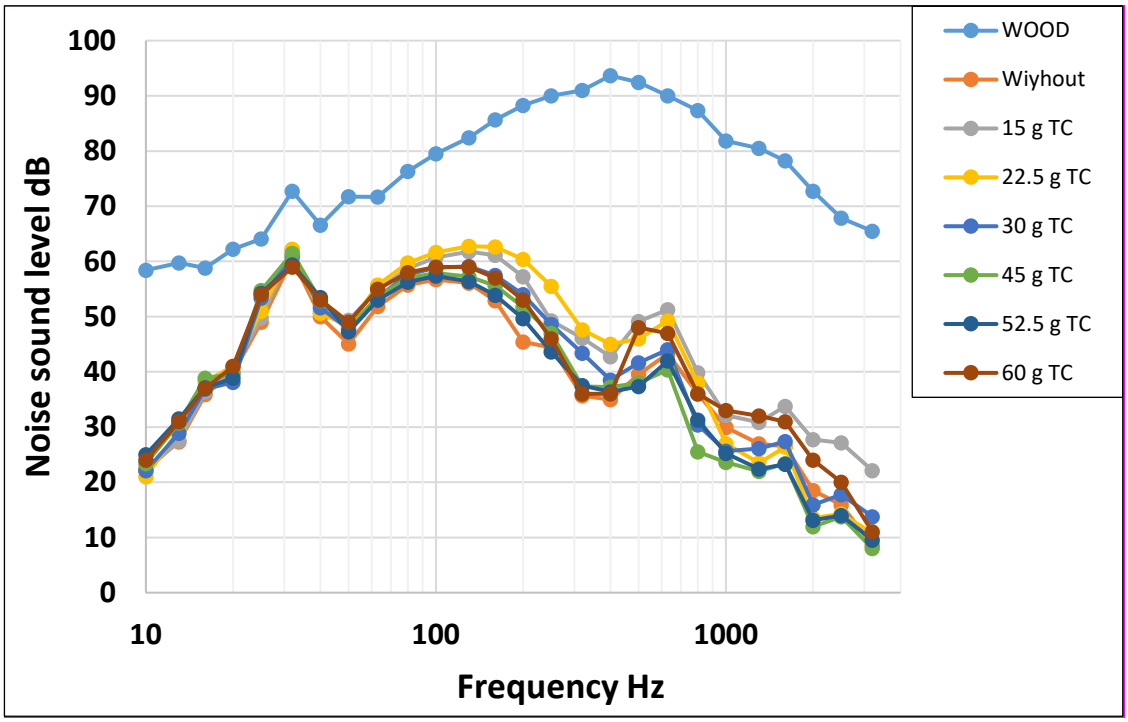

Figure 4.7. Effect of increased TC addition on impact sound insulation.

The second observation is with reference to the effect of the particle size of these TC and BC additives. Larger particle sizes increase performance in the important frequency range larger than 1000Hz. The data are presented in Figures

4.8-4.9 below complemented by the four figures in Appendix A Figures A6-A9 depicting particles sizes of 300, 600, 1180 and 2360 microns.

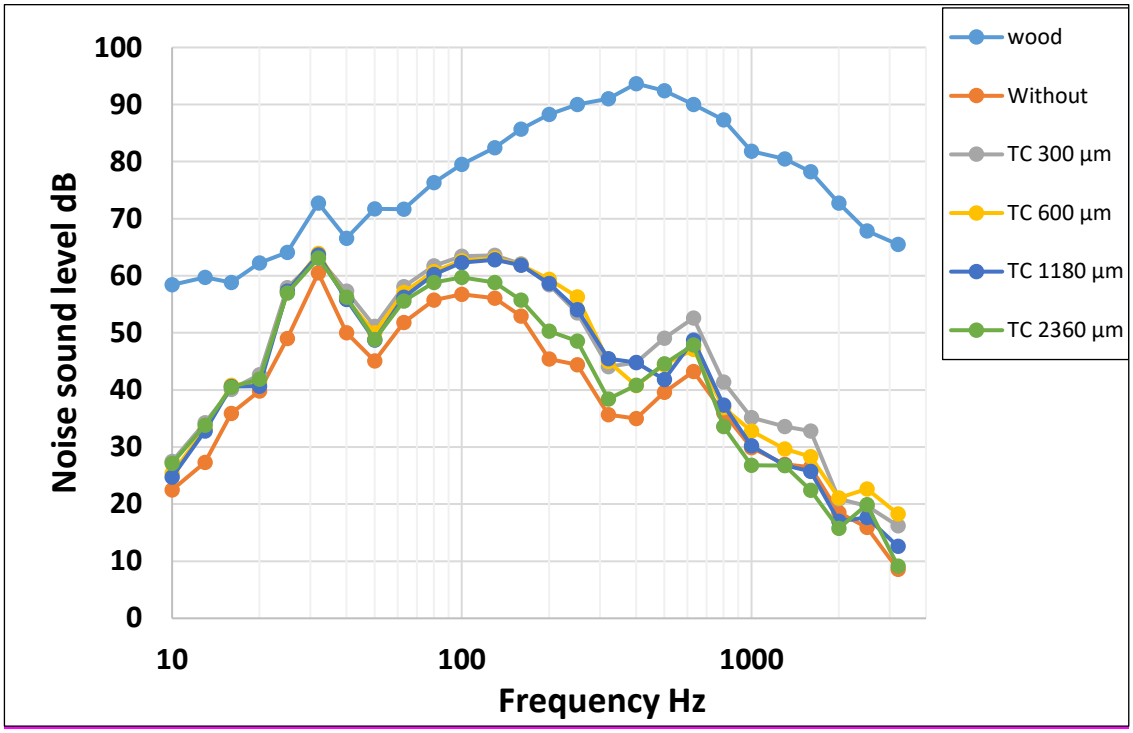

Figure 4.8. Effect of particulate size of TC on impact sound insulation.

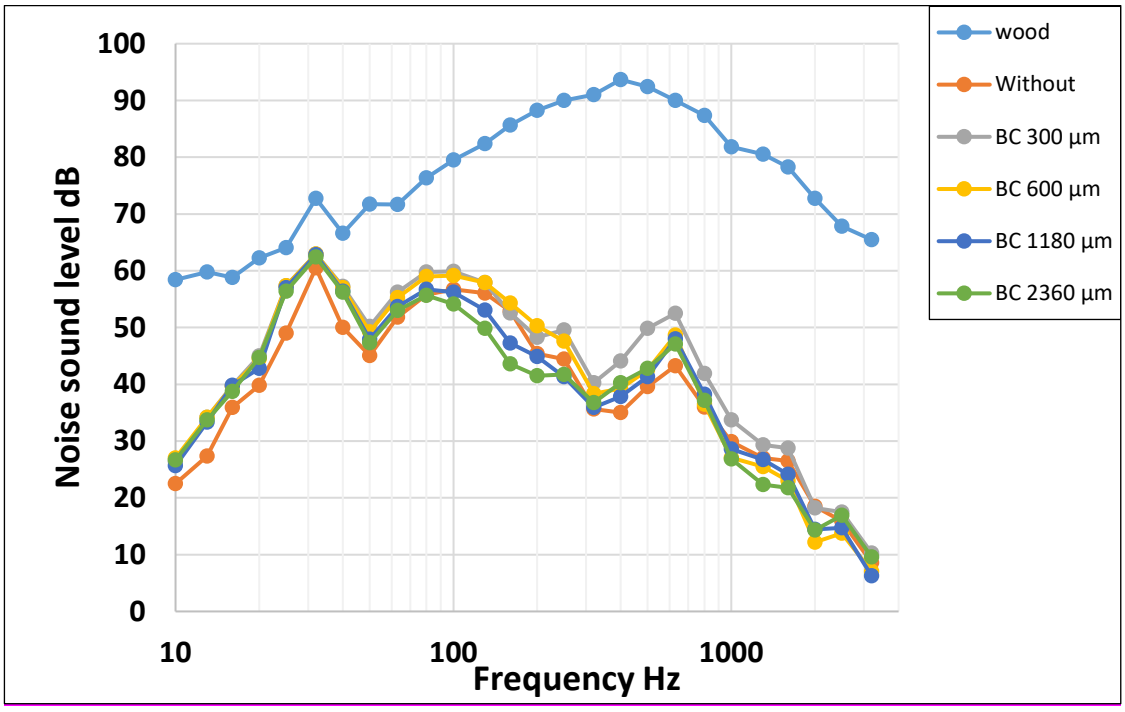

Figure 4.9. Effect of particulate size of BC on impact sound insulation

The net conclusion from these refinements in the choice of the formulation is that optimal performance is obtained with an SBR/TFSR of 40% and the addition of 30 g of large particle size bumper crumb BC. This corresponds to an optimum formulation of SBR/TSFR/>1mmBC of 80g/120g/>1mm 30g BC. Note the thermal insulation performance was optimised according to the data presented so far on the basis of the SBR/TFSR ratio only. In order to ensure that the thermal insulation performance still holds at this optimal 80g/120g >1mm 30g BC composition, thermal conductivity measurements were performed on such a sample. Figure 4.10 presents the pertinent data supported by further data (see Appendix A, figure A-12) in the entire parameters range. It can be observed that the thermal conductivity at optimal composition with BC addition is 0.03-0.04 W/m^2K compatible with the data in Figure 4.4 obtained on the basis of SBR/TFSR only. Thus the optimisation loop is complete with respect to material composition.

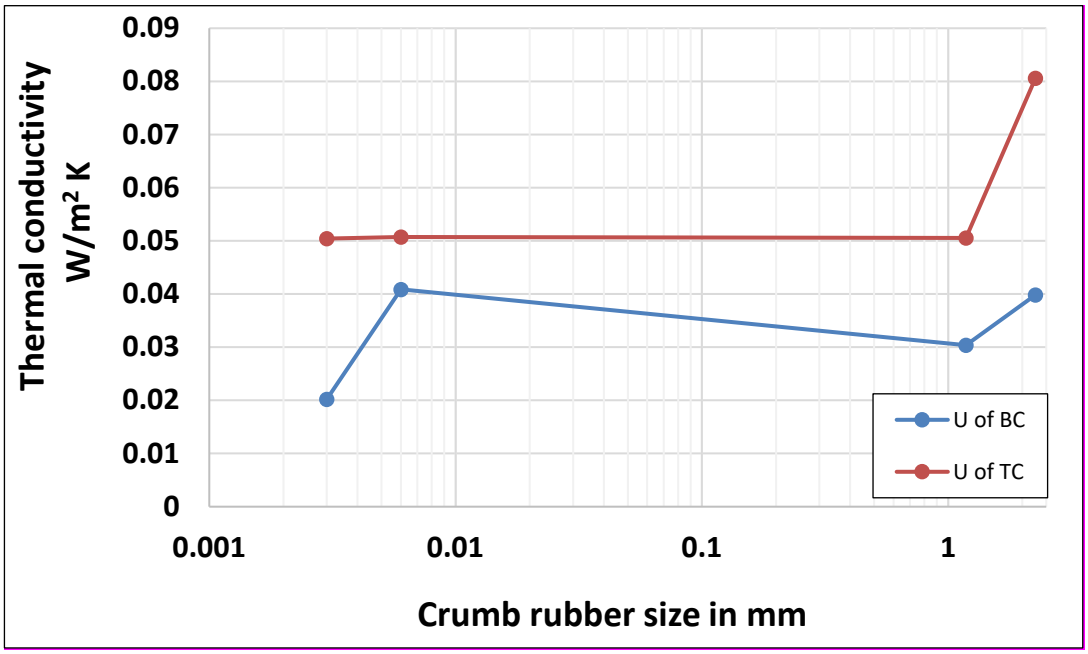

Figure 4.10. Effect of crumb rubber size on thermal conductivity at optimal composition SBR/TSFR/Crumb

Having established the optimal composition, the next objective was to establish the effective thickness required for insulation. This is clearly important from a cost-benefit perspective when considering large scale manufacturing. Figure 4.11 presents precisely this data and shows as expected increased performance at larger thickness but only in the range say 100-200Hz. At higher frequencies, a thickness of 10mm is sufficient and will perform just as well as

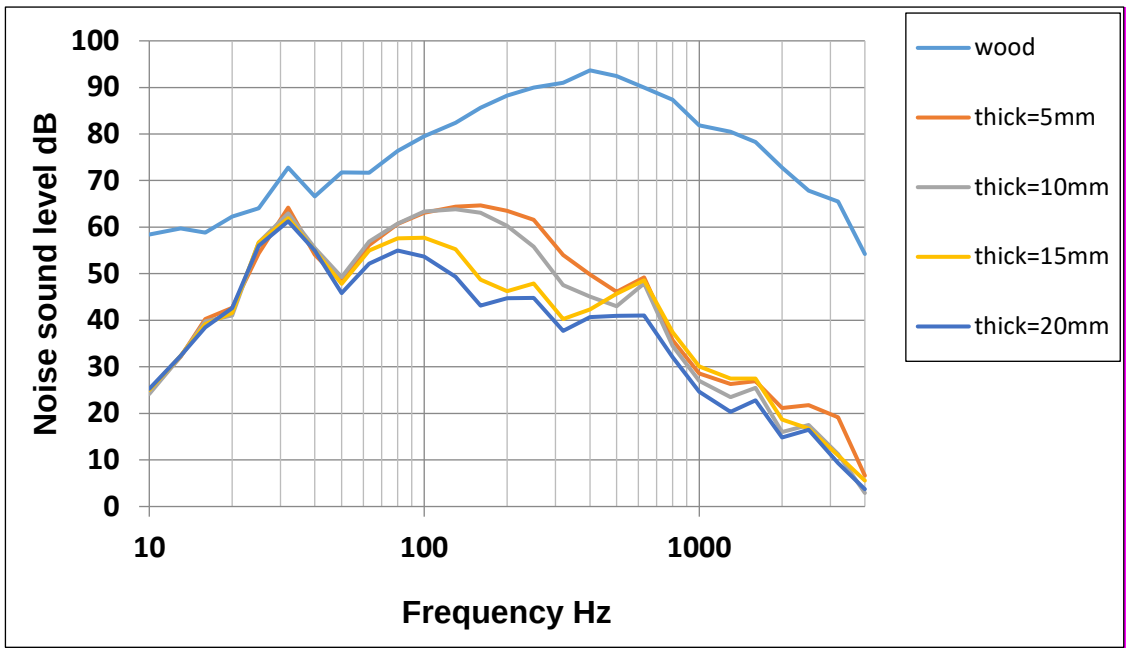

Figure 4.11. Effect of under-layer thickness at optimal formulation.

4.3.2 Comparison with commercial under-layer materials

Having arrived at the optimal formulation, it is now important to make a comparison of the insulation performance achieved with those of commercial materials. As shown in Figure 4.12, the material constructed in this research performs as well if not better than the competitor PU foam, Chip matrex and Cloud 9 materials. As this is a waste based material made essentially from tyre shred fibre residue (TSFR), it can be brought to market very cheaply whilst giving similar performance to the more expensive commercial materials.

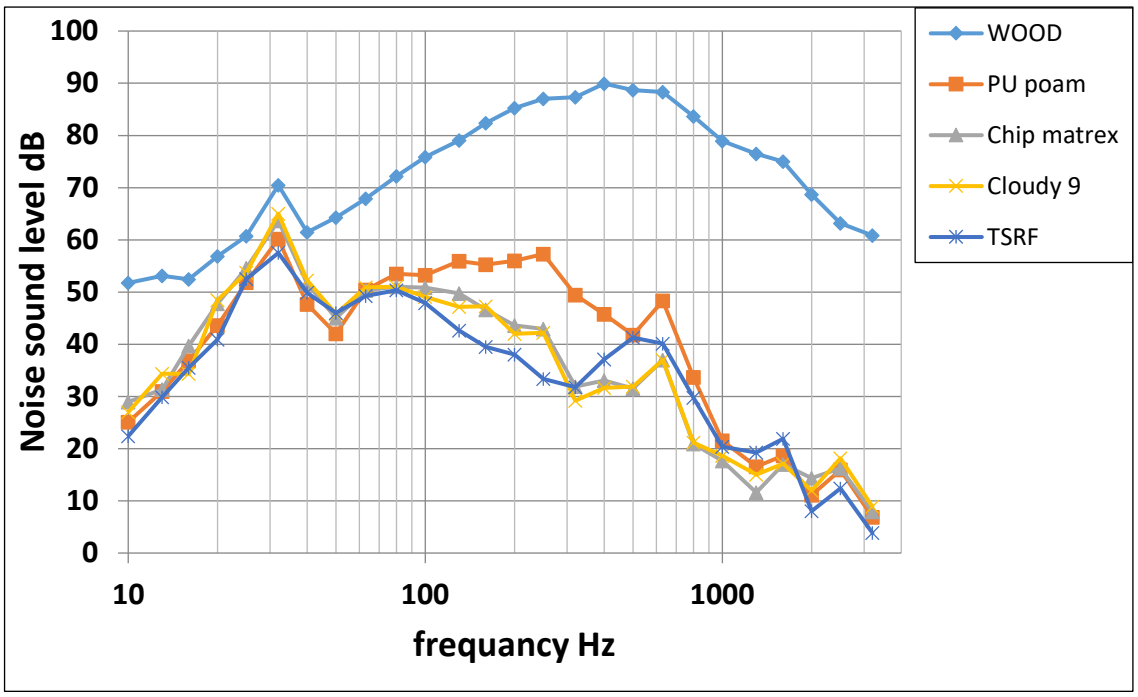

Figure 4.12. Acoustic insulation comparison between the waste based material made in this research with commercial products

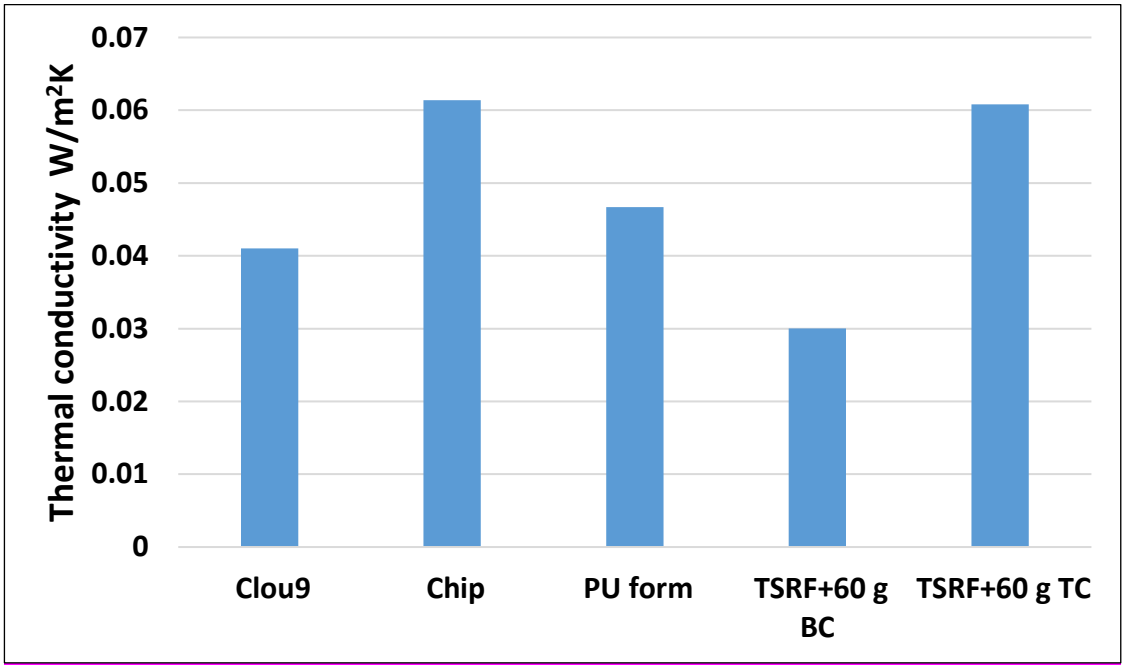

Figure 4.13. Thermal insulation comparison between the waste based material made in this research with commercial products.

4.3.3 Acoustic Absorption of SBR/TSFR compounded layers

In the previous section, data on the experimental work leading to the optimal construction of under-layer material with tyre shred fibre residue (TSFR) was presented. An optimal formulation was established by measuring the impact sound insulation and the thermal conductivity of the various samples made. In this section, the acoustic absorption of the SBR/TSFR compounded layers without crumb is studied. The objective for this work-package is many-fold:

1. Assess the suitability of these materials for sound absorption performance by measuring sound absorption for a range of SBR/TSFR ratios (10, 20, 30, 40, 50 and 60%) using a 29mm Bruel & Kjear 4 microphone standing wave tube as described in the experimental Chapter three.
2. Measure the fundamental properties of these materials, namely tortuosity, porosity, flow resistivity, α_∞ , Ω , σ , respectively.
3. Using the widely accepted Allard-Champoux-Johnson model described in Section 4.2, extract from the measured acoustic absorption, the theoretically predicted tortuosity, porosity and flow resistivity.
4. Compare the measured and predicted tortuosity, porosity and flow resistivity as a further test that the data so far collected are sound.
5. This exercise also enable the computation of the important fundamental properties, Λ and Λ', the inertia-viscous length and the thermal length respectively.

In conclusion, this package of work completes the full characterisation of these materials so that further studies can be made for further applications for example or to test other mathematical models.

The sound absorption data measured are given in Figure 4.14 and show that these materials are good at absorbing sound, performing as well as commercial acoustic foams (AFS) at SBR/TSFR 40%/60% w/w which provide the mechanical integrity required.

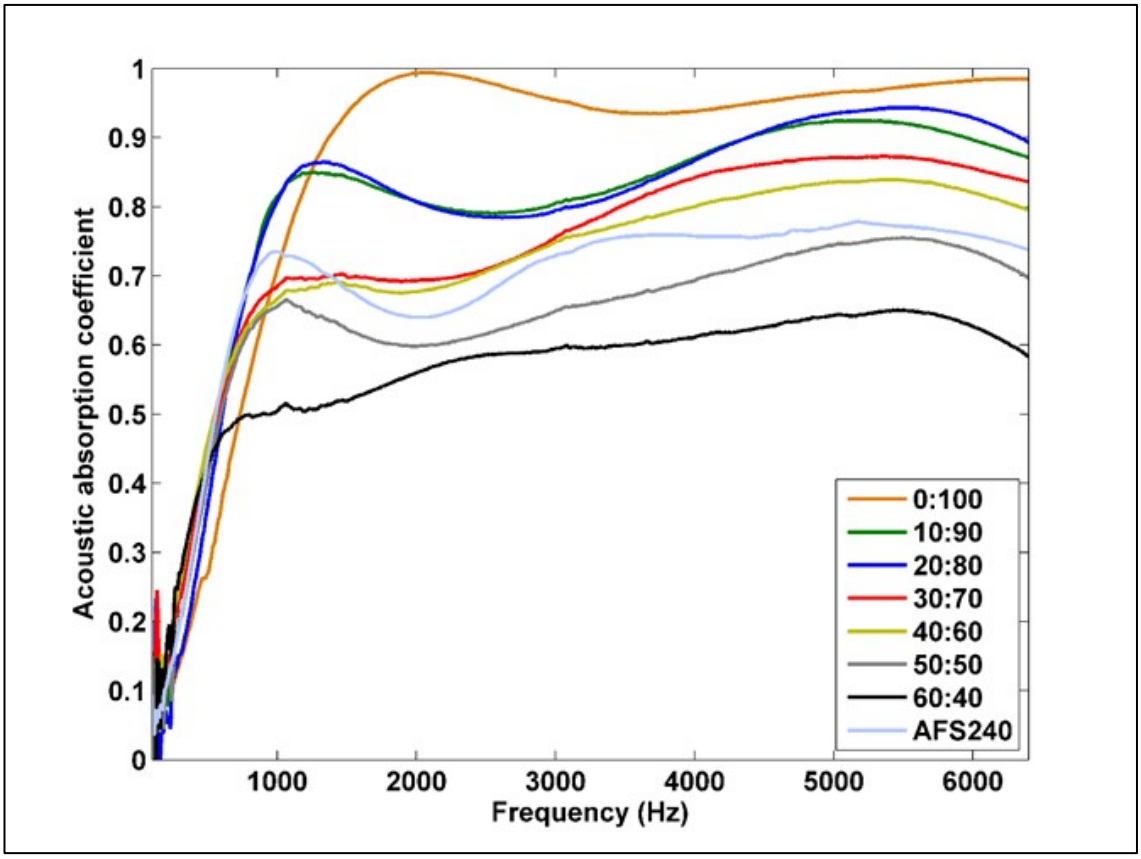

Figure 4.14. Measured acoustic absorption coefficient spectra for the materials and comparison with commercial material AFS.

As for the comparison between the measured and predicted, which are obtained by using the absorption curve from the impedance tube test in the FORMAX computer program which predict all five parameters, fundamental properties of tortuosity, porosity and flow resistivity, these are best summarised in Table 4.1 and Figure 4.15 below. The fit is remarkably excellent ($\pm$ 1%) and gives confidence in the accuracy of the data measured. Interestingly, whereas

the characteristic thermal length increases with increasing binder content, the characteristic viscous length decreases. Relating this observation to Figure 4.2 suggests that increasing binder content increasing “nipping” between the cells.

Table 4-1 Measured and predicted tortuosity, porosity and flow resistivity and predicted inertia-viscous length and thermal length at various SBR/TSFR ratios.

SBR/TSFR %	σ **Exp. Pa.s/m^2**	σ **Pred. Pa.s/m^2**	ϕ **Exp.**	ϕ **Pred.**	α_∞ **Exp.**	α_∞ **Pred.**	**ρ Kg/m^3**	Λ **µm Pred.**	Λ' **µm Pred.**
0:100	**36,390**	**35,478**	**0.97**	**0.97**	**1.61**	**1.60**	**106**	**264**	**382**
10:90	**138,033**	**138,510**	**0.79**	**0.79**	**1.78**	**1.78**	**187**	**244**	**415**
20:80	**162,393**	**161,099**	**0.77**	**0.77**	**1.78**	**1.78**	**277**	**240**	**450**
30:70	**200,730**	**202,627**	**0.76**	**0.76**	**2.59**	**2.41**	**346**	**160**	**481**
40:60	**299,067**	**297,627**	**0.74**	**0.74**	**2.76**	**2.62**	**380**	**127**	**563**
50:50	**412,250**	**410,175**	**0.67**	**0.68**	**3.28**	**3.06**	**427**	**91**	**657**
60:40	**713,053**	**711,954**	**0.64**	**0.63**	**3.35**	**3.17**	**482**	**83**	**682**

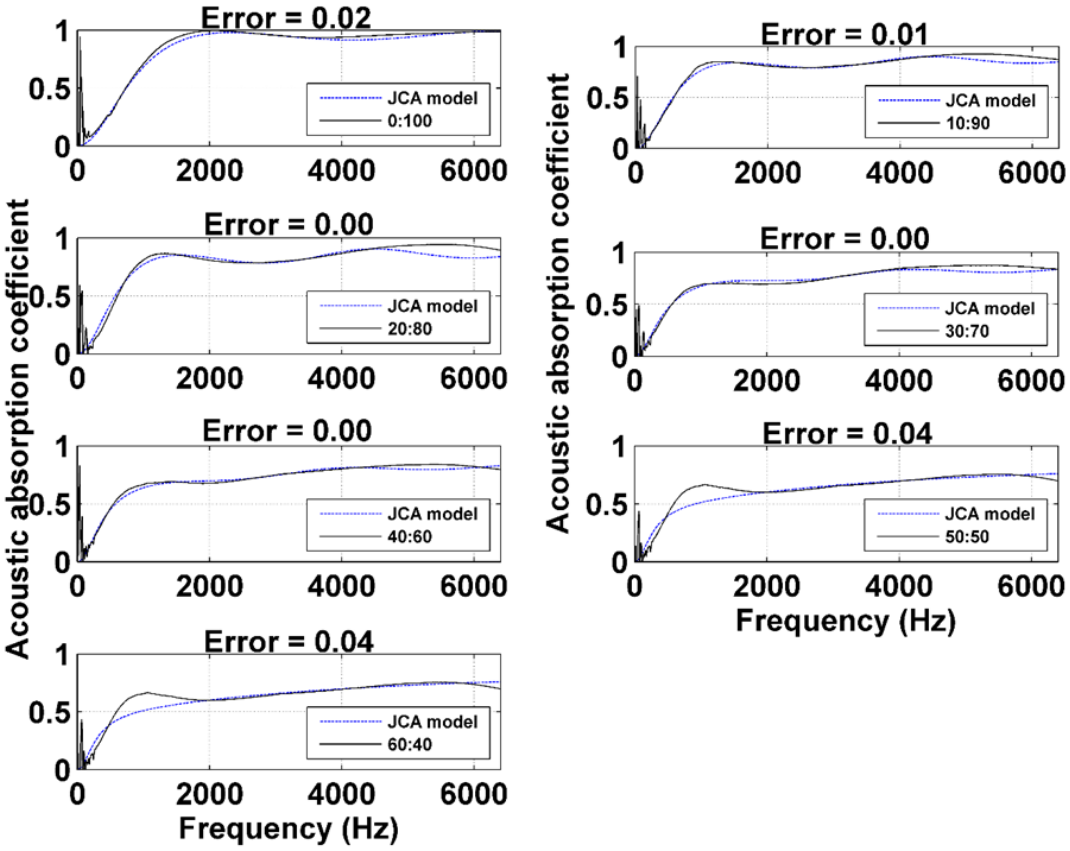

Figure 4.15. Measured and predicted absorption coefficient spectra vs. frequencies.

To complete the characterisation, Figure 4.16 displays the variation of the tortuosity, porosity and flow resistivity with increasing SBR/TSFR ratio. These figures tally with the acoustic absorption data in that the decrease in porosity is clearly reflected in the higher frequency regions in the acoustic absorption coefficient spectra. For frequencies above 3 kHz there is a systematic drop in the absorption coefficient with increasing binder levels. With tortuosity and flow resistivity, the increase with increasing SBR addition is consistent with decreasing open and connected pores hence an increase in the resistance of air passing through.

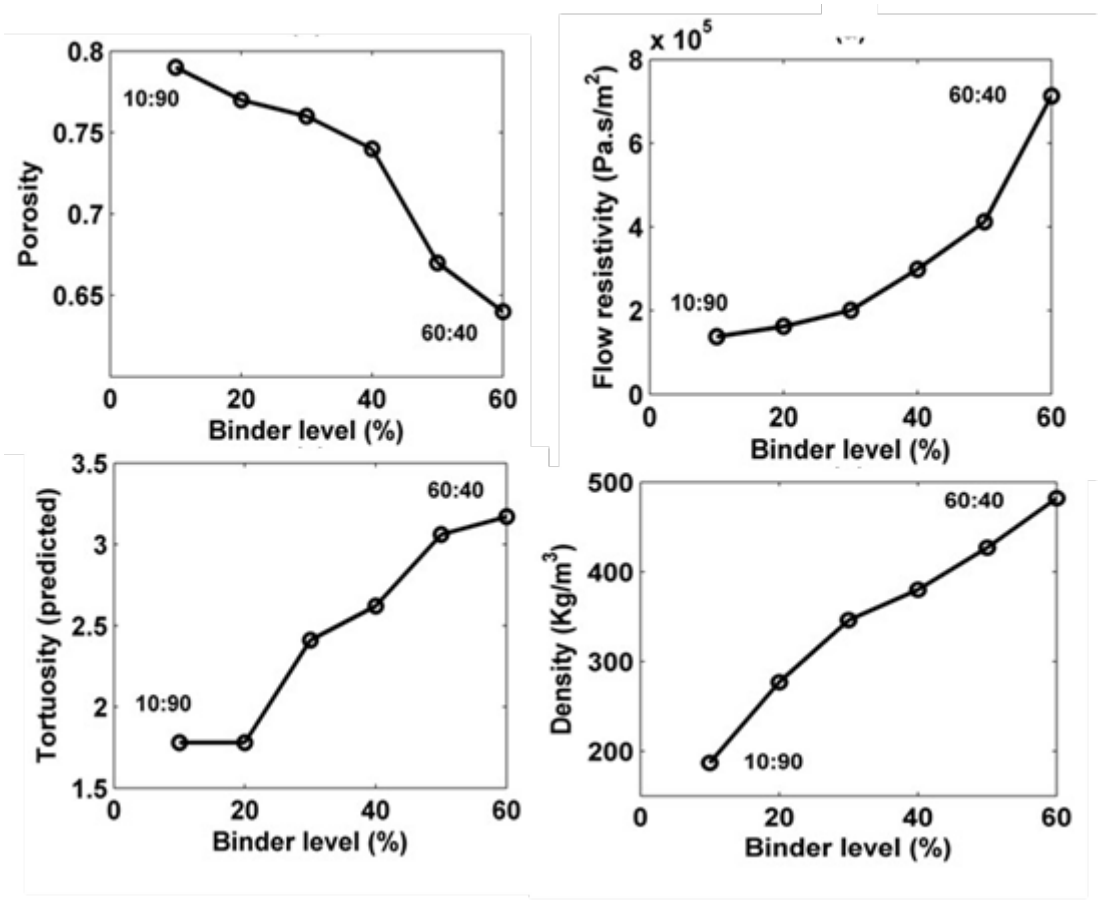

Figure 4.16. Variation of tortuosity, porosity, flow resistivity and density with increasing SBR/TSFR ratio.

4.3.4 Conclusion of SBR/SRFR

It has been demonstrated that it is possible to recycle tyre shred residue waste into an acoustic and thermal underlay product. Using recycled materials to produce new layers of acoustical and thermal insulation will help us to minimise the effect of these waste materials on our environment. The best formula according to acoustical prospect which has a minimum amount of latex, and it will minimise the noise about 50 dB especially with high frequencies above 1000 Hz. Bumper crumb of large sizes is better than tyre crumb additive for enhancing impact sound insulation. Large material thicknesses are intuitively better

performing but it was found that 10 mm thickness was sufficient for good impact sound insulation in the frequency range of interest. According to thermal insulation prospect, the 40% latex ratio to fibre is the best ratio. This is because this amount of binder is the optimum amount to bind fibre together without filling the small closed pores.

4.4 Random Multi-Size Cells Porous Structuring with PU foam binder under Vacuum

This construction as explained earlier is intended for cavity wall application to achieve good sound absorption performance. Again the main raw material is tyre shred fibre residue (TSFR) from granulated tyres with fibre length ranging from 1mm to 60mm and fibre diameter in the range of 20–30μm. Unlike with SBR, here a PU foaming binder was used in the proportion 40% PU-60% TSFR w/w. A two-component PU formulation was used as described in the experimental chapter, 90% DMI -10% polyol to obtain good mechanical integrity. In order to kick off the foaming reaction, the TSFR was wetted. In order to control the foaming further, vacuum was utilised. Thus, the components were mixed then poured in a cylindrical vessel from which vacuum could be applied at the top of the cylinder as describe to allow sufficient expansion of the foam the cylindrical mould to 12 cm high. As to measure sound absorption, a sample thickness of 3 cm is required, the formed foam was sliced into 4 separate samples. Now, as the sound absorption depends on the direction of the pores structure, the measurements in the impedance tube were performed on both sides of the sample. Thus 8 absorption curves were measured at each vacuum level, 0, -5, -

10, -15, -20, and -25 in Hg bringing the total data set to 48 curves. Also for each of these samples, the fundamental properties of porosity, tortuosity and flow resistivity were measured as well as density and pore size distribution. The pore size distribution is naturally of great interest here to assess the benefits of applying vacuum. As with the SBR construction, these data were underpinned by the Johnson Champoux- Allard model.

4.4.1 Porosity, tortuosity, flow resistivity and density

These are presented in Figure 4.17 and show the critical effect of vacuum pressure on structure formation and suggesting an optimal pressure of -10 in Hg.

At -10 in Hg, the porosity reaches a value of 92%. Below this threshold of vacuum, the data suggests a collapse of the porous structure. This is confirmed by the height at which the structure expanded during formation as shown in Table 4.2, with the maximum reached at -10 in Hg and dropping thereafter with increased vacuum.

Table 4-2 Expansion height of the TSFR-PU with applied vacuum levels

Applied vacuum (in Hg)	0	-5	-10	-15	-20	-25
Sample height in mm	58	177	245	212	146	42
Increase in volume (%)	0	3.05	4.22	3.66	2.52	-0.28

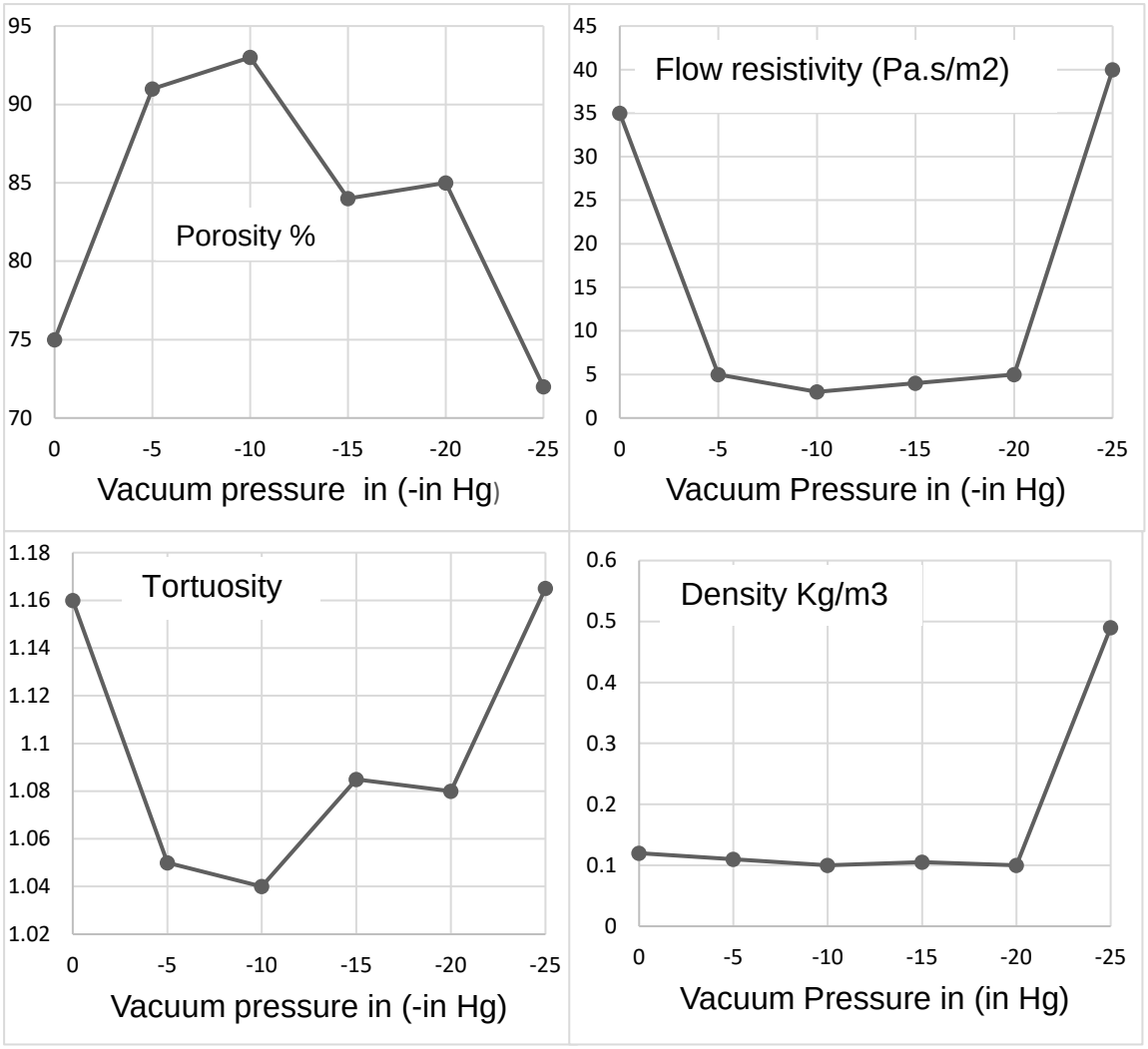

Figure 4.17. Properties of TSFR PU Foams

4.4.2 Pore Size Distribution

The pore size distribution was obtained by image analysis of the foam transversal samples shown in Figure 4.19. At atmospheric pressure, the pore sizes appear similar and as the vacuum is applied, large pores appear giving a wider pore size distribution compared to no vacuum. Figure 4.18, showed there is an increasing in the number of pores with all pore sizes range. The increasing in the pore's number is limited with macro pore size which is between 0 and 2 on

X-axis, while this increasing became more noticeable with micro pore size, which is between -2 and 0 on X-axis. The effect of vacuum on pore's number was very clear with finite pore size which is between -6 and -3 on X-axis. This increasing in the all pore's size has improved the acoustical performance of the final product, as well as, has increased the final product volume around four times. The result of the image analysis shows this clearly, confirming the optimal vacuum pressure with the highest pore size to occur at -10 in Hg vacuum pressure.

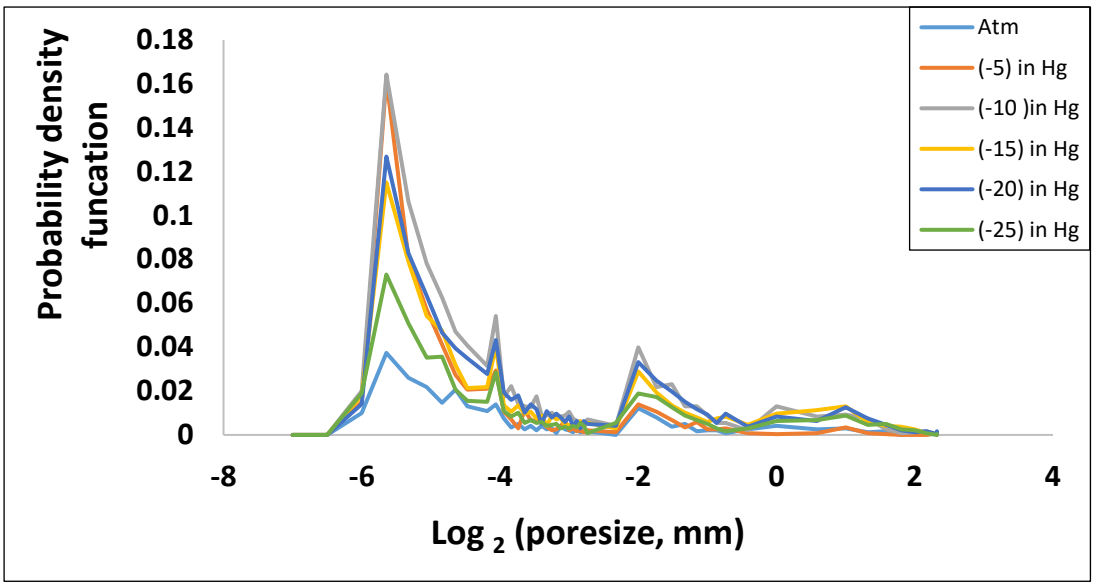

Figure 4.18. Pore size distribution variation with applied vacuum

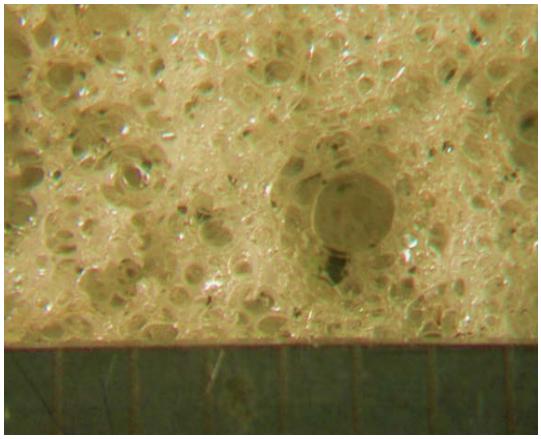

Polyurethane insulation produced under atmospheric pressure

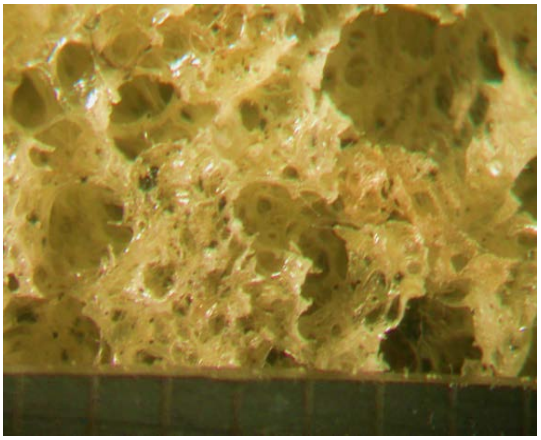

Polyurethane insulation produced under -5 in Hg vacuum pressure

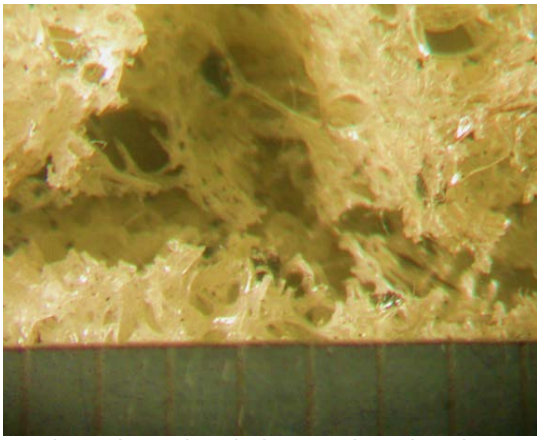

Polyurethane insulation produced under -10 in Hg vacuum pressure

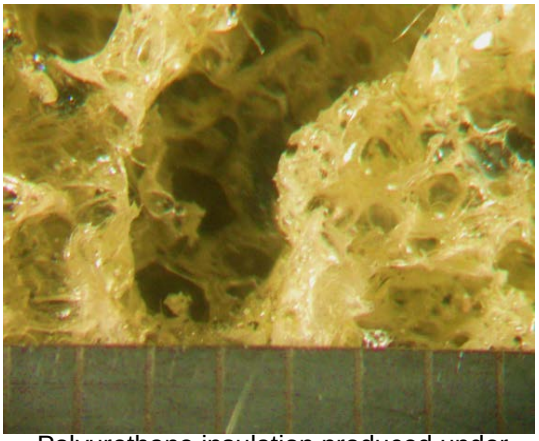

Polyurethane insulation produced under -15 in Hg vacuum pressure

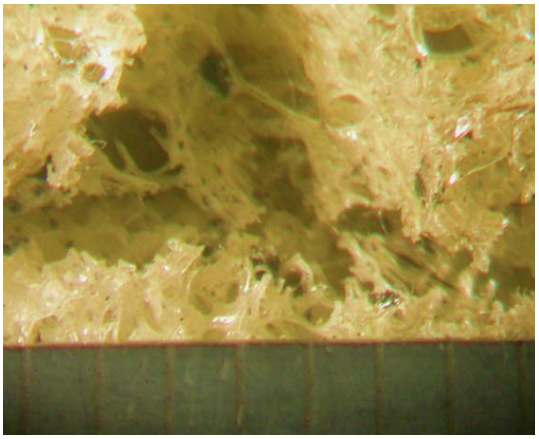

Polyurethane insulation produced under -20 in Hg vacuum pressure

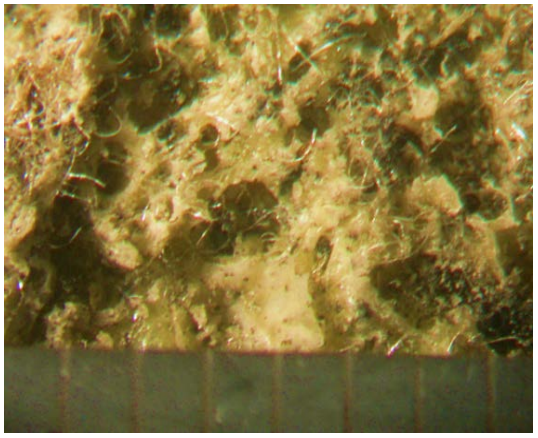

Polyurethane insulation produced under -25 in Hg vacuum pressure

Figure 4.19. Images of the foam transversal cuts

4.4.3 Sound absorption

Figure 4.20 and 4.21 present the sound absorption curves in both directions of pore growth, at the various vacuum levels tested and the enhancement the application of vacuum provides. Absorption measured in the direction opposite to pore growth shows 100% sound insulation at 400 Hz and a sound insulation fluctuation around 90% for the optimal -10 in Hg vacuum. This is a remarkable enhancement compared with the 45% sound absorption observed at 400Hz at atmospheric pressure. Further data in Appendix B on all the samples support this observation. Table 4-3 shows the measured and predicted properties of -10 in Hg vacuumed sample for four slides with 30 mm thickness of sample.

Table 4-3. The experimental and predicted non-acoustical parameters of -10 in Hg vacuumed polyurethane insulation samples.

Slabs of -10inHg	σ **(exp.) (Pa.s/m^2)**	σ **(pred.) (Pa.s/m^2)**	ϕ **(exp.)**	ϕ **(pred.)**	α_∞ **(exp.)**	α_∞ **(pred.)**	**Density (Kg/m^3)**	**Thick. (m)**	Λ **(μm) (pred.)**	Λ' **(μm) (pred.)**
1st	27545	4,866	0.917	0.939	3.044	2.175	98.93	0.03	83.1	391.1
2nd	17566	4,229	0.919	0.999	2.277	2.12	92.46	0.03	129.7	425.6
3rd	16435	5,474	0.921	0.95	2.087	1.936	92.06	0.03	137.5	438.7
4th	14884	3,506	0.927	0.999	2.133	1.873	91.83	0.03	132.6	432.5

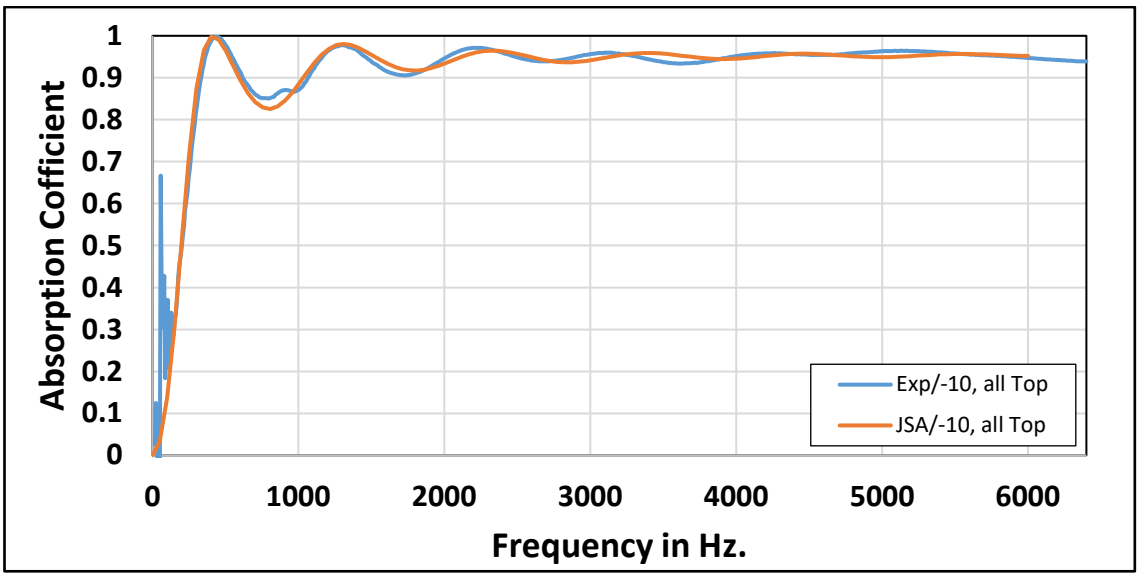

Figure 4.20. The experimental and theoretical absorption curves of the 120 mm thickness of -10 in Hg vacuumed pressure sample, the direction of the wave with the same pores growing direction.

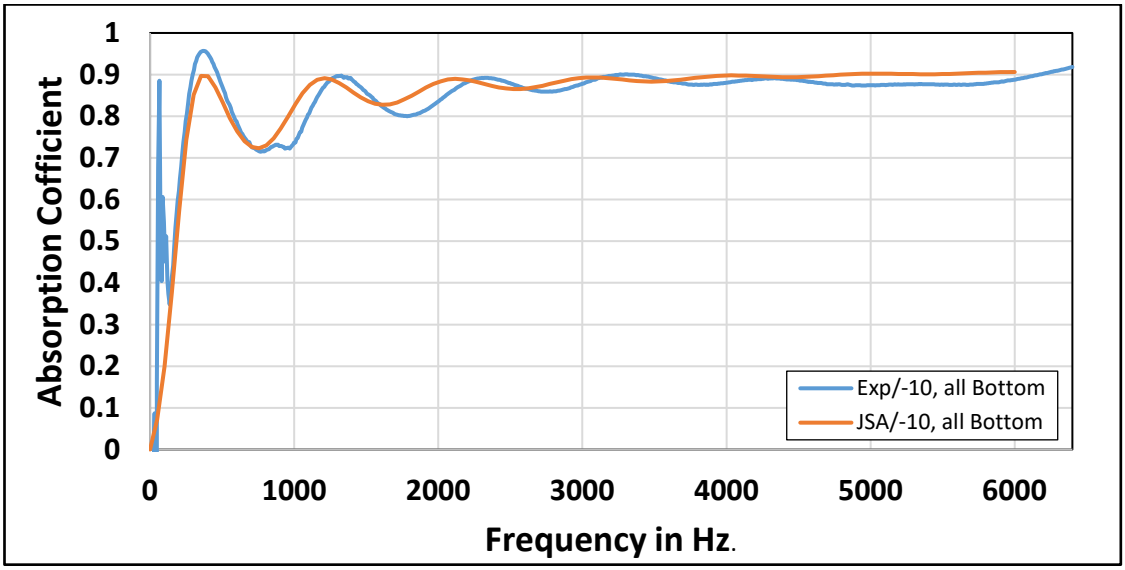

Figure 4.21. The experimental and theoretical absorption curves of the 120 mm thickness of -10 in Hg vacuumed pressure sample, the direction of the wave with the obverse pores growing direction.

4.4.4 Mathematical Underpinning

As with the SBR constructions, the absorption data of the PU foamed tyre shred fibre residues were analysed using the Allard-Champoux-Johnson model. The results of the modelling are shown in Table 4.4, comparing the output of the model (tortuosity, porosity, flow resistivity and characteristic viscous and thermal lengths). A very good fit is observed giving confidence in the experimental measurements. Interestingly, an increase in the thermal and viscous lengths are observed when the statistical indicator of fiber diameter increases with the log-normal mean fiber diameter yielding the better results.

This modelling was applied to all the sections, including the whole of the 120mm original sample and further data can be found in Appendix B1-6.

Note that in the modelling, when calculated macroscopic parameters are used, the main observed discrepancies related to the sound absorption coefficients are due to the resistivity estimation errors related to the moderately high and high resistive materials. For the lowest resistive material (-5Hg), thermal characteristic length errors have also a significant impact on the predicted sound absorption coefficient. This is shown in Table 4.4.

Table 4-4 Mathematical underpinning with Johnson Champoux-Allard model.

Binder : TSR (%)	σ **Mes. Pa.s/m²**	σ **Pred. Pa.s/m²**	ϕ **Mes.**	ϕ **Pred.**	α_∞ **Mes.**	α_∞ **Pred.**	**ρ Kg/m³**	**Thick. cm**	Λ **µm Pred.**	Λ' **µm pred.**
Atm T	46367	45791	0.85	0.85	1.3	1.3	120.256	12	16	73.8
Atm B	65598	68610	0.87	0.869	3.67	3.56	120.256	12	345	405.3
-5 in Hg T	9689	8865	0.98	0.999	2.834	2.669	107.423	12	140	169.9
-5 in Hg B	12955	11877	0.87	0.85	3.633	3.407	107.423	12	53.4	150.9
-10 inHg T	41261	43000	0.86	0.85	1.73	1.508	93.819	12	90	125.1
-10 inHg B	11781	10979	0.84	0.85	1.527	1.73	93.819	12	71.4	542.9
-15 inHg T	9197	8997	0.98	0.999	1.865	1.915	96.418	12	80.8	631.3
-15 inHg B	3930	3526	0.97	0.999	3.929	3.575	96.418	12	87	140.8
-20 inHg T	1699	1683	0.85	0.85	1.721	1.645	110.613	9	120.7	450.4
-20 inHg B	5392	5502	0.98	0.999	1.773	1.623	110.613	9	122.6	629
-25 inHg T	89640	89899	0.84	0.85	1.6	1.819	395.223	5	145	189
-25 inHg B	75660	71303	0.9	0.9	3.51	3.113	395.223	5	675	858.9

Following from this modelling, the absorption of the entire plug 120 mm of material formed in the cylinder could be modelled to predict its sound absorption as it is not possible to measure it. The corresponding absorption curves are shown in Figures 4.22 and figure 4.23.

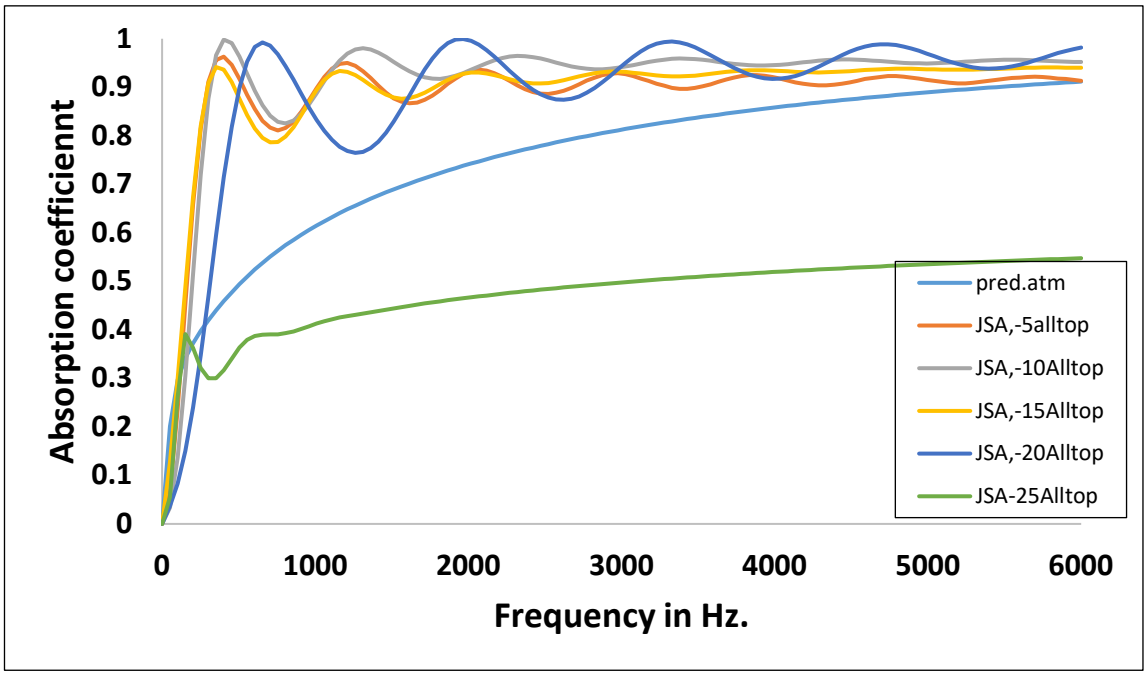

Figure 4.22. Sound absorption curve measured with incident sound hitting top of the sample (opposite of pores growing direction).

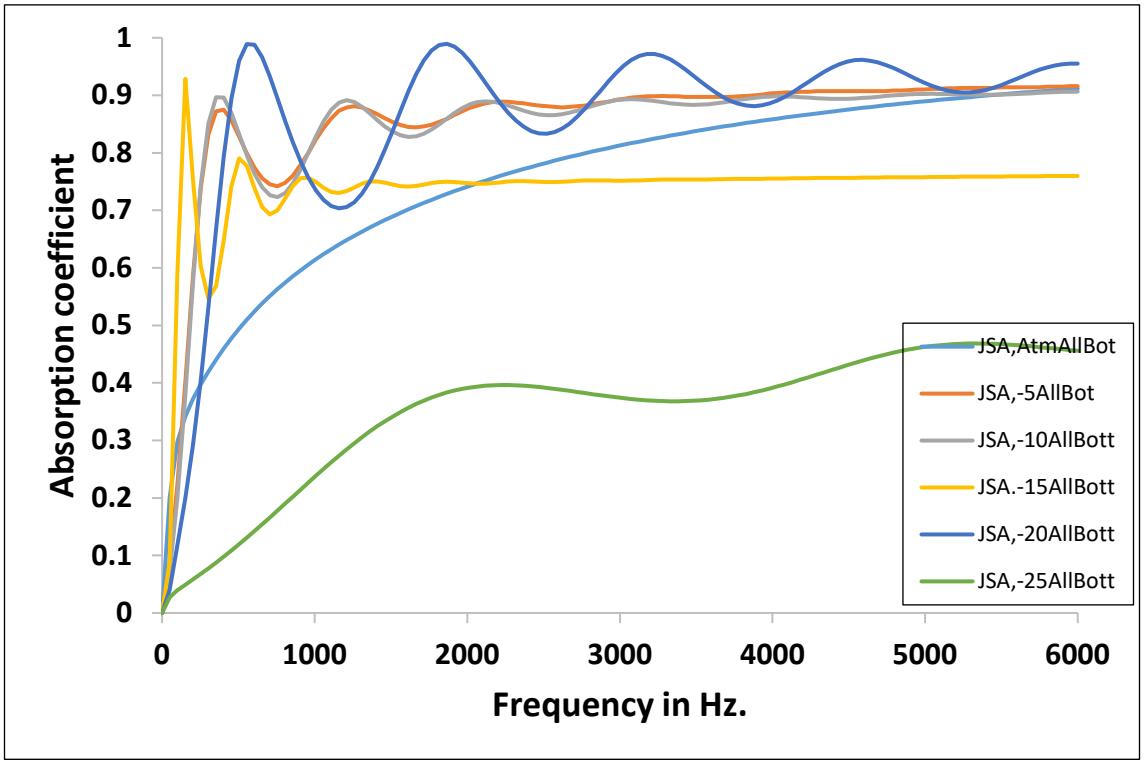

Figure 4.23. Sound absorption curve measured with incident sound hitting bottom of the sample (in the pores growing direction).

4.4.5 Conclusions

It has been proved that using vacuum pressure during polymerisation reaction with polyurethane binder has improved the acoustical properties of the produced insulation and multiply the production volume around four times with the right vacuum pressure. Producing a polyurethane insulation material under this process (vacuum pressure) should be done under an optimisation condition of applied vacuum pressure applied. The best applied vacuum pressure according to the production volume was -10 in Hg, where the volume increase was 4.22 times of the atmospheric sample volume. The insulation produced with this vacuum pressure yielded the highest absorption coefficient compared with tests at other high vacuum which lead to the collapse of pores.

4.5 Stratified Cells Porous Structuring with PU foam

This construction as explained earlier is intended for pipeline insulation of fluids that emit noise when pumped such as natural gas in offshore installations. The objective is thus to achieve as good sound absorption performance as achieved using expensive commercial pipe claddings. Such commercial pipe claddings use a series of layers, most typically 3 layers according to ISO 16556. For the comparison of performance, the very high performing Armaflex (24mm), ArmaSound RD 240 (27mm) and Arma-Chek R (3.2mm) three-layers or System B insulation will be used.

For the construction of our multilayer insulation, again the main raw material is tyre shred fibre residue (TSFR) from granulated tyres with fibre length ranging from 1mm to 60mm and fibre diameter in the range of 20–30μm. As with the cavity wall application, a two-component (MDI-Polyol) PU foaming binder was used with the fibre wetted with water, in varying proportion so as to tailor the porosity formed in each of the 3 layers, the objectives being to (i) create a gradient of porosity in the layers similar to the ones achieved with commercial claddings and (ii) whilst keeping the layer flexible enough to be wrapped around a pipe.

To achieve stratification, a multilayer moulding approach was used using the frame method described in the Experimental chapter, basically a rectangular mould 120cm x 30cm x 2cm + 2 frames 120cm x 30cm x 2cm, allowing the production of 3 x 2cm layers one on top of the other (see Figure 3.10). Samples from each layers were collected to measure the important fundamental properties of porosity, tortuosity and flow resistivity.

Now for the measurement of the acoustic transmission loss of such a 3-layer insulation, it was applied to a section of pipe and tested. A novel method was used and this is described in the Experimental Chapter 3. It dispenses with the use of a reverberation chamber and a long section of a metal pipe requiring a significant amount of insulation material and considerable preparation time. Instead, a compact laboratory setup is used, consisting of a short section of an insulated 12” metal pipe which may be excited with a simple mechanical impact, an accelerometer attached to the pipe wall and a laser vibrometer. The proposed method determines the ratio of the vibration velocity measured on the external wall of the pipe insulation and that measured on the external wall of the metal pipe.

In this section, the data collected are presented together and underpinned with (i) a comparative assessment of the measurement method using a well-defined standard insulation (System B described earlier) for which reverberation data are known and (ii) a finite element model developed to predict the acoustic behaviour.

4.5.1 Porosity, tortuosity, flow resistivity and density

As the control of porosity and related properties, tortuosity, and flow resistivity as well as elasticity (to enable it being wrapped around a pipe) are paramount to achieving the insulation sought, one layer samples were made at varying proportions of tyre shred fibre residue, MDI, polyol and water. These are presented in Table 4.5 with the TSFR:MDI:Polyol proportion kept constant and varying only the water which is the reactant causing the release of CO_2, hence controlling foaming.

In forming the layers, it is noted (see Table 4.5) that the foam height expansion was above 3cm, reaching as much as 9cm when 20g of water were added. For the measurements of properties and sound absorption, each of the samples were cut at the 3cm height.

Table 4-5. The main measured properties of polyurethane insulation which is produced by different chemical formulas. 3cm samples

Filler: MDI: Polyol: water /g	Height Expansion/ cm	Porosity Ω	Flow resistivity σ	Density ρ	Tortuosity α_∞
75:60:15:5	3.0	31.37	120737	95.87	5.67
75:60:15:10	4.0	70.23	89930	32.69	3.21
75:60:15:15	6.5	82.87	17854	16.38	2.11
75:60:15:20	9.0	89.52	11265	14.85	1.42

We observe from this table, the significant changes in porosity with water amounts, 5g producing a low porosity of 31% and 20g a porosity of 89.5%. The porosity of 5g sample was deemed not to be suitable and 2 and 3-layers fabrications were made in combinations of the 3 porosities obtained 70%, 83% and 89.5% guided by the sound absorption each of these 1 layer, 2 layers and 3 layers could provide.

4.5.2 Validation of the new sound insertion loss measuring method

Having fabricated the insulating layers, the next challenge was to measure their sound absorption properties. The recommended method according to ISO 16556 is the use of a reverberation chamber which both expensive, time consuming, requiring a long pipe and much insulation. Another challenge and objective of the research was thus to find a much simpler method, but one which would reproduce standard data as those obtained with the reverberation chamber

method. The method was described in the experimental chapter; here the data tested against standard data and underpinned have been presented with a finite element model. The standard data are those obtained on System B in a reverberation chamber. In the finite element model, the insertion loss is predicted using the differential model equations applied to the geometry of the measuring system used in this study, (see Figure 4.24) with an impact applied to the inside of the pipe (see Appendix C).

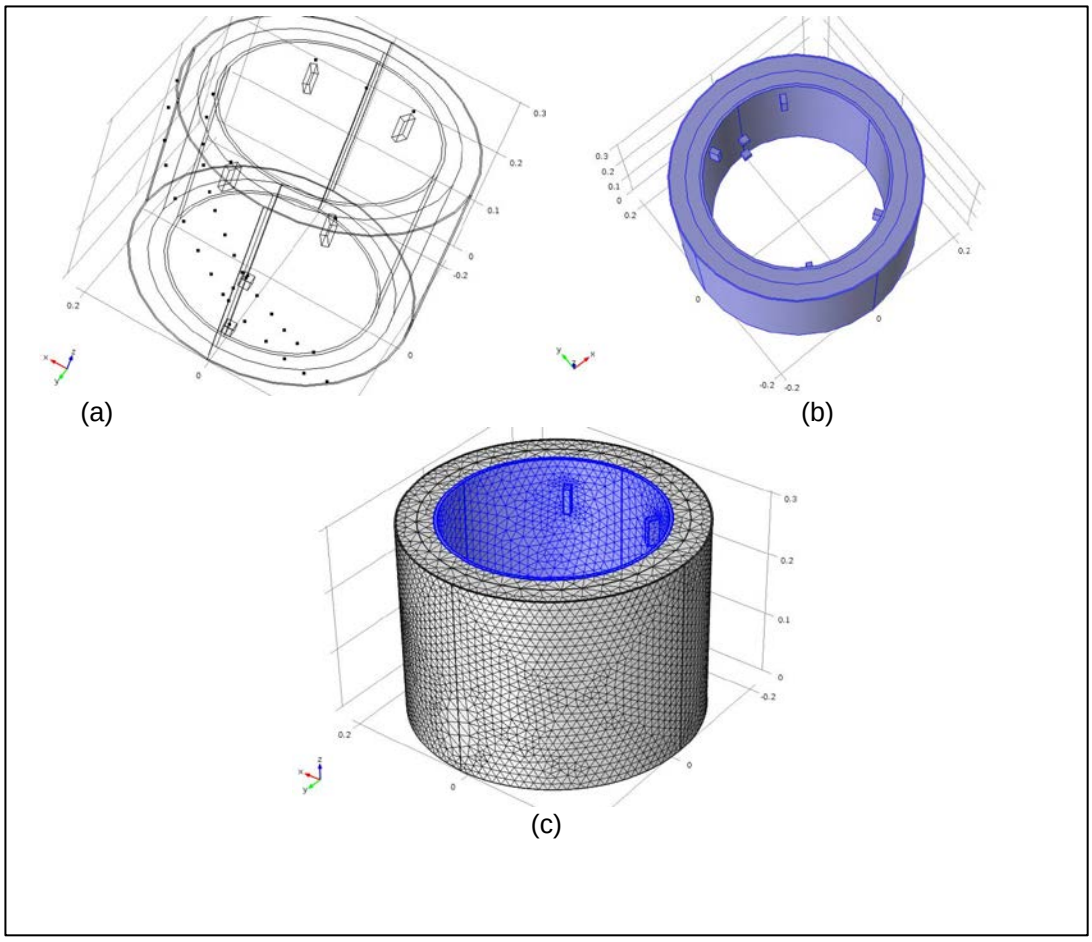

Figure 4.24. The model geometry adopted in COMSOL: (a) positions of the measurement of the source sound, input to the model; (b) representation of the three pipe insulation layers; (c) finite element mesh composed of tetrahedral elements.

Figure 4-25 presents a validation of this calibration method comparing sound absorption of System B measured in a reverberation chamber, in the method developed here and those predicted theoretically. The fit is remarkably excellent.

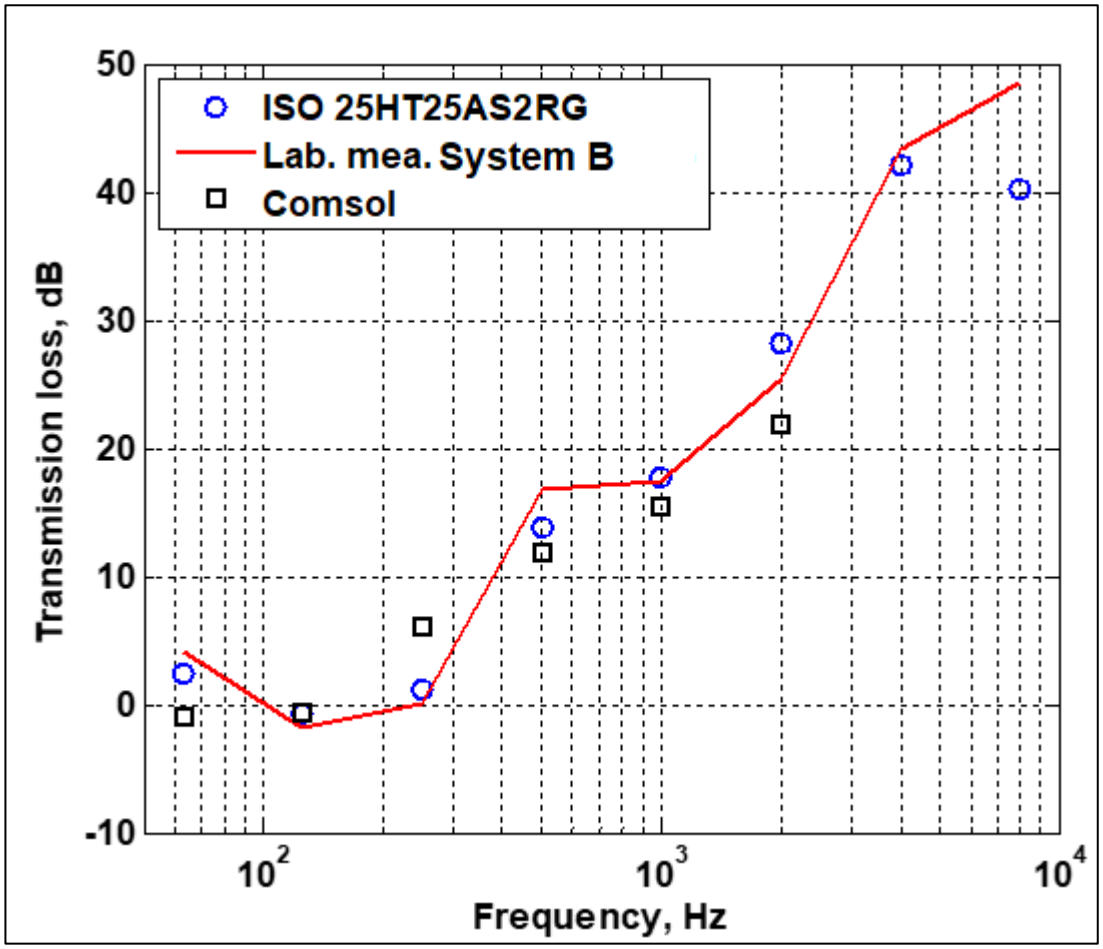

Figure 4.25. Test on system B. A comparison of the measured and predicted octave band transmission losses for insulation new systems: circles represent ISO 15665 test, squares represent COMSOL predictions, Line represents new laboratory test results.

4.5.3 Transmission loss of 3 layers stratified insulation developed

Having validated the calibration method, the performances of the 3 layers stratified insulation developed was now measured in an effort to optimise it, to

obtain the most performing combination of porosities. Such sound absorption performances are shown in Figure 4.26 below showing the highest performing combination to be 89.5%/83%/70% giving transmission losses in excess 50db at 500Hz and larger, up to 65db.

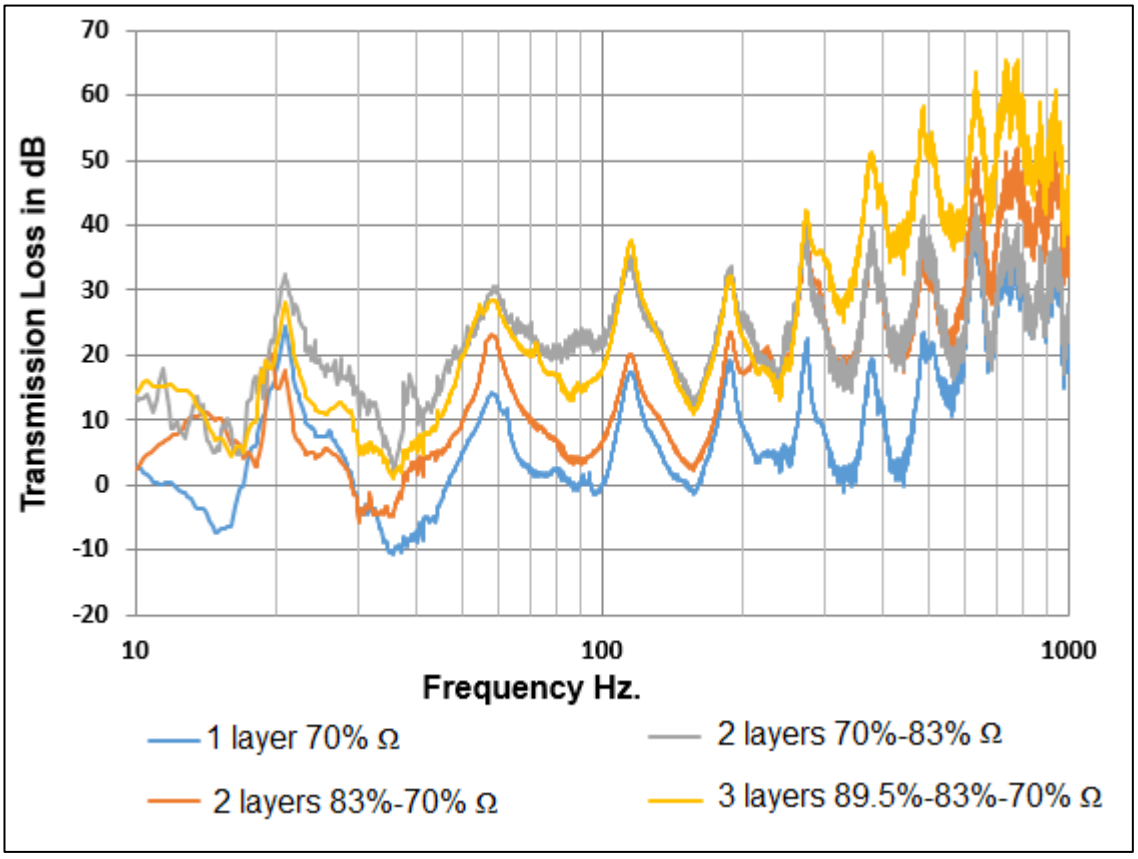

Figure 4.26. The transmission loss of multilayer insulation on the pipe with three different sequences.

4.5.4 Comparison with commercial pipe cladding System B

As mentioned earlier, the “acid” test is if the insulation made with this waste competes with the very best available in the market, Armacell System B. The comparison is made in Figure 4.27 and includes insertion losses measured for the 1-layer at 70% porosity, 2 layers 83%/70% and 3 layers 89.5%/83%/70%.

The structures formed in this research clearly compete well and outperform the best commercial standard System B.

Note that Figure 4.27 also brings together the earlier calibration comparison made in Figure 4.25. The data obtained from the proposed laboratory experiment and from the standard ISO 15665 test agree within ±2 dB in the frequency range below 8 kHz. In the 8 kHz octave band, an 8 dB discrepancy between these data sets can be observed. The transmission loss at this frequency is relatively high (above 40 dB). As a result, a relatively poor signal-to-noise ratio is likely to be attained at the time when either the ISO 15665 sound pressure level or the laboratory laser vibrometer measurements were taken.

As for modelling results, the COMSOL model is able to predict qualitatively the behavior of the measured data. The agreement between the model and the measured data is within 2-5 dB in the frequency range of 63 - 1000 Hz. This is an important frequency range where the acoustic performance of the insulation is often limited and attempts are made to improve it by combining several layers of insulation. A above and below this range the discrepancy between the measurement and prediction is within 10 dB. The proposed model does not account for the complex poroelastic behavior of the open and closed cell foams which are used in insulation System B. Therefore, the observed degree of discrepancy between the model and measured data is expected.

These two comparisons show that the model captures within ±5% the position of the resonance maxima in the velocity level spectra. The model underpredicts by 10-15 dB the vibration velocity level on the outer skin of the pipe insulation in the frequency range below 200 Hz. Above this frequency, the model

agrees with the measured data within 2-5 dB. The model is able to predict the narrow band vibration velocity level on the internal surface of the pipe within 2-3 dB in the frequency range below 1000 Hz. Above this frequency, the discrepancy between the model and measured vibration velocity spectrum becomes significant.

Note that the data in Figure 4.27 obtained in the method develop in this study were for experiments repeated 5 times for all 14 positions so that the average of the 5 sets was taken with a standard deviation less than 1dB, as shown in figure 4.28.

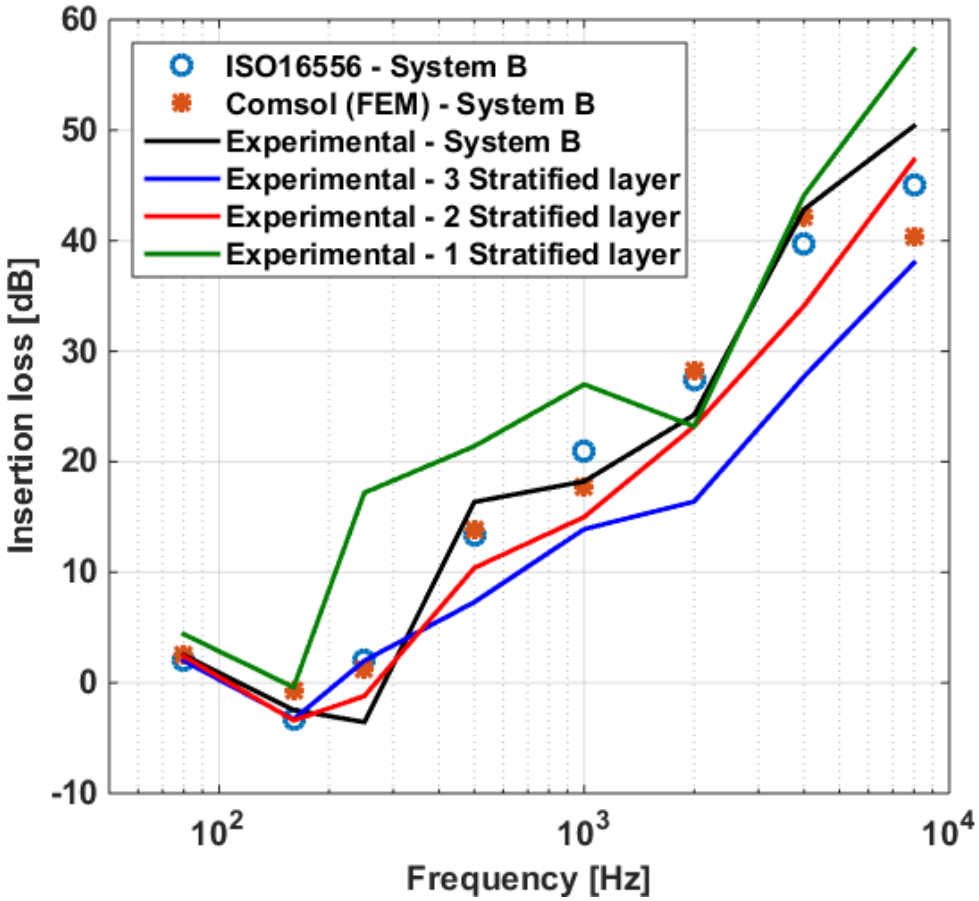

Figure 4.27. The insertion loss of system B insulation by three different methods with three stratified materials with different internal layers.

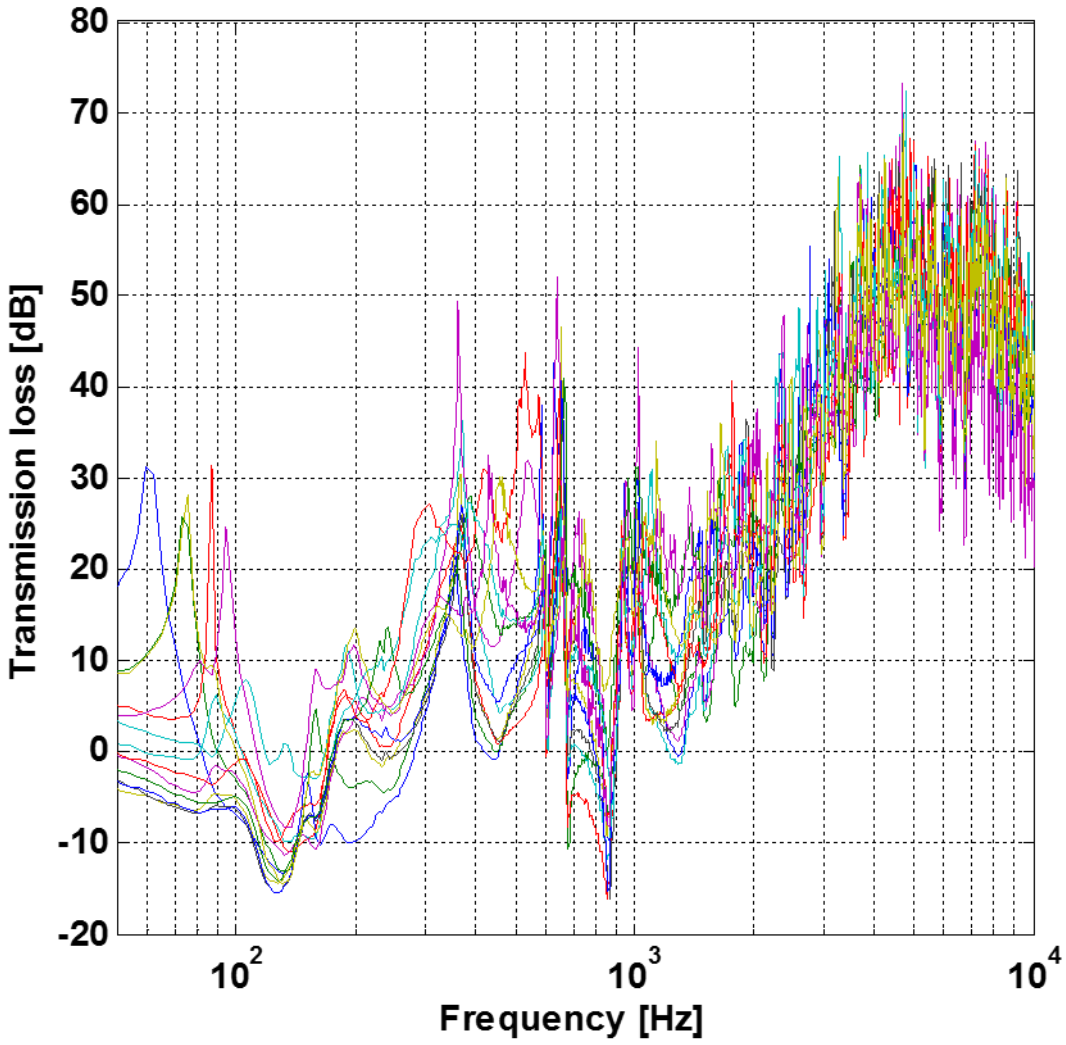

Figure 4.28.Insertion loss results of 14 points together for one test with high frequency range between 0 and 10,000 Hz.

4.5.5 Conclusions

Stratified structures with a gradient of porosity have been formed and have shown excellent acoustic performance when compared with the very best commercial 3-layers insulation Armacell System B. The key characteristic is the porosity gradient which here was optimal at 89.5%/83%/70%, achieved simply by controlling the amount of water added to the compounded tyre shred residue and 2 components PU. Moreover, a simpler method for measuring transmission loss of pipe cladding was developed. It is cheaper as it uses a short section of pipe (30cm) with the noise induced using a small activated brass pendulum and does not require a reverberation chamber.

CHAPTER FIVE

CONCLUSIONS AND RECOMMENDATIONS

5.1 Conclusions

This research, stimulated by the need to up-cycle elastomeric waste rather than dumped them into our environment, provides the scientific and technological intelligence to develop acoustic and thermal insulation materials with performance similar or better than those currently available in the market. The starting waste elastomer here was tyre shred fibre residue (TSFR), essentially the last dust in the recycling of end of life tyres. These residues essentially are the fibre remnant of tyre shredding containing minute quantities (but offensive if released to the environment) of rubber. The materials developed from this waste were then turned, using binders, into porous structures suitable as (i) under-layer, (ii) cavity wall and (iii) pipe cladding insulation.

The strategy utilised in this development was the control of porosity using:

- SBR binder which is non-foaming.
- PU foaming binder.

With SBR, the control of porosity is clearly dependent on the SBR/Tyre Shred Residue Fibre ratio. Acoustic absorption and heat insulation in this instance could also be enhanced by loading the SBR/TSFR with rubber or bumper crumb, another source but more valuable elastomeric waste. The size of these crumb will play a role as well the properties of the rubber making the bumper and the

tyre. These parameters were tested together with measuring acoustic and heat insulation performance to optimise formulations of under-layer insulation.

With the PU binder, the creation of porosity is straighter forward as the PU reaction with water (used to wet the TSFR) will generate CO_2 gas that will form pores. Such porosity can be left to proceed at atmospheric pressure or manipulated and expanded by employing vacuum and those were parameters manipulated to produce cavity wall insulation.

With PU binder, at atmospheric condition, layers could also be produced of varying porosity depending on the extent of the PU foaming reaction, i.e. on the amount of water (the reactant necessary to produce CO_2). Thus depending on the PU/TSFR/Water, porosity could be controlled and successive layers could be deposited on top of another to create a multilayer, stratified porosity structure, most suitable for pipe cladding application in noisy pipe lines (those transporting LNG for example in offshore installation).

The above thus summarises the work carried out, which included full characterisation of the structures made (porosity, tortuosity and flow resistivity) and a theoretical underpinning using the Johnson-Champoux-Allard model. As this model is widely accepted as being very reliable, it serves as a test of the accuracy of the measurements made in this study (it predicts porosity, tortuosity and flow resistivity) but also enable the calculation of the fundamental additional properties of viscous and thermal lengths.

Thus in conclusion, the research in addition of being of practical interests, it also has academic interests in that, these structures are made now completely characterised for further studies.

Another concurrent output of this research, equally important, is the innovative method of measuring sound absorption developed in this research. It is simple in that it does not require a reverberation chamber and uses a short length of pipes.

Below is a brief summary of each of the product section results and the new acoustic absorption measurement method on pipe cladding technique

5.1.1 Random pore size by SBR binder

This construction is suitable for under-layer application. 40%/60% SBR/TSFR was found to be optimal. Addition of a small quantity (15% w/w) particle size bumper crumb BC larger than 1mm enhanced impact sound insulation. 10 mm thickness provides optimum performance and is very cost effective to produce.

5.1.2 Random pore size by Polyurethane binder under vacuum

Produce an insulation with higher mechanical properties compared with SBR binder. Compared with atmospheric pressure, expansion under vacuum up to five times leading to enhance acoustical performance due to an increase in closed and open cell micro and macro pores).

5.1.3 Stratified materials

Porosity in each layers controlled by amount of water added. Optimal porosity stratification was 90%/83%/70% outperform the top commercial 3-layers insulation Armacell System B.

5.1.4 New Acoustic Absorption Measurement Method on Pipe Cladding

Designed to replace the BS ISO 15665:2003 standard, the advantages being BS ISO 15665:2003 uses a 6-meter long pipe section in a reverberation room (large capital cost) at a typical test cost of £5000 per sample , while the new test uses a 300 mm length pipe and a simple noise absorption set up.

5.2 Recommendations

Finally, no research work is complete and further studies are required, particularly in measuring the mechanical properties of the structures made.

In this research I relied on engineering experience to satisfy the following research outcomes:

1. The under-layer materials made with SBR had sufficient integrity to be easy applied.
2. The cavity wall insulation materials were mechanically superior to be fabricated into panels or blocks for use in cavity wall.
3. The multilayer pipe cladding were sufficiently flexible that they could be wrapped around a pipe.

Thus investigating the use of other binders becomes important. The new binder that could be used should be fibre base such as polystyrene melt binder, which may increase the final product porosity rather than fill the pores thus reducing the sound absorption.

Other important characteristics to assess in future work should be with regard to flammability and the addition of flame retardant additives, as well as additives against mould growth and biological contaminant and water permeability.

References

A. Khan, K. V. H., H. Benkreira and R. Patel (2007) Acoustics of recycled materials. *Proceedings of the institute of acoustics (Cambridge)* 29 (2).

A.Mohamed, K. V. H. a. M. H. (2005) The experimental investigation of the effects of water saturation on the acoustic admittance of sandy soils. *J. Acoust. Soc. Am*.

Abu-Jdayil, B., Mourad, A.-H. and Hussain, A. (2016) Thermal and physical characteristics of polyester–scrap tire composites. *Construction and Building Materials* 105 472-479.

Allard, J. F. (1993) Propagation of Sound in Porous Media:Modelling Sound Absorbing Materials. *Elsevier, Amsterdam*.

Attenborough, K. (1983a) Acoustical characteristics of rigid fibrous absorbents and granular materials. *the Journal of the Acoustical Society of America* 73 (3) 785-799.

Attenborough, K. (1983b) Acoustical characteristics of rigid fibrous absorbents and granular materials. *," J. Acoust. Soc. Am.* 73.

Attenborough, K. (1985) Acoustical impedance models for outdoor ground surfaces. *Journal of Sound and Vibration* 99 (4) 521-544.

Attenborough, K. (1992) Ground parameter information for propagation modeling. *The Journal of the Acoustical Society of America* 92 (1) 418.

Attenborough, K. (1993) Models for the acoustical properties of air-saturated granular media. *Acta Acust.* 1.

Bazley, M. E. D. a. E. N. (1970) Acoustical Properties of Fibrous Absorbent Materials. *Appl. Acoust* 3.

Benkreira, H., Khan, A. and Horoshenkov, K. V. (2011) Sustainable acoustic and thermal insulation materials from elastomeric waste residues. *Chemical Engineering Science* 66 (18) 4157-4171.

Biot, M. A. (1956) Theory of propagation of elastic waves in a fluid-saturated porous solid. II. Higher frequency range. *The Journal of the acoustical Society of america* 28 (2) 179-191.

Bond, D. E. M., Clark, W. W. and Kimber, M. (2013) Configuring wall layers for improved insulation performance. *Applied Energy* 112 (Journal Article) 235.

Brennan, M. J. and To, W. M. (2001) Acoustic properties of rigid-frame porous materials — an engineering perspective. *Applied Acoustics* 62 (7) 793-811.

Brouard, B., Lafarge, D. and Allard, J.-F. (1995) A general method of modelling sound propagation in layered media. *Journal of Sound and Vibration* 183 (1) 129-142.

Champoux, Y. and Allard, J. F. (1991) Dynamic tortuosity and bulk modulus in air-saturated porous media. *Journal of applied physics* 70 (4) 1975-1979.

Chen, A. (2008) Closing in on Zero-Energy Buildings. *Environ Energy Techno Division News* 8 (2).

Delany, M. and Bazley, E. (1970) Acoustical properties of fibrous absorbent materials. *Applied acoustics* 3 (2) 105-116.

Diamant, R. M. E. (1965) *Insulation of Buildings Thermal and Acoustic.* London: iliffe books ltd.

Embleton, T. F. W. (1983) Effective flow resistivity of ground surfaces determined by acoustical measurements. *The Journal of the Acoustical Society of America* 74 (4) 1239.

Fan, K.-S., Lin, C.-H. and Chang, T.-C. (2005) Management and Performance of Taiwan's Waste Recycling Fund. *Journal of the Air & Waste Management Association* 55 (5) 574.

Fellah, Z. E. A., Chapelon, J. Y., Berger, S., Lauriks, W. and Depollier, C. (2004) Ultrasonic wave propagation in human cancellous bone: Application of Biot theory. *The Journal of the Acoustical Society of America* 116 (1) 61-73.

Ghofrani, M., Ashori, A., Rezvani, M. H. and Ghamsari, F. A. (2016) Acoustical properties of plywood/waste tire rubber composite panels. *Measurement* 94 382-387.

Glicksman, L., Schuetz, M. and Sinofsky, M. (1987) Radiation heat transfer in foam insulation. *International Journal of Heat and Mass Transfer* 30 (1) 187-197.

Harmonoise (2003) *D17 Engineering method for road traffic and railway noise*

Horoshenkov, K. and Swift, M. (2001) The effect of consolidation on the acoustic properties of loose rubber granulates. *Applied Acoustics* 62 (6) 665-690.

Horoshenkov, K. V. (1998) Padé approximants for the acoustical properties of rigid frame porous media with pore size distributions. *The Journal of the Acoustical Society of America* 104 (3) 1198.

J.-F. Allard, e. a. (1994) Evaluation of tortuosity in acoustic porous materials saturated by air. *Rev. Sci. Instrum* 65.

Jimenez-Espadafor, F. J., Becerra Villanueva, J. A., García, M. T., Trujillo, E. C. and Blanco, A. M. (2011) Optimal design of acoustic material from tire fluff. *Materials and Design* 32 (6) 3608-3616.

Johnson, D. L., Koplik, J. and Dashen, R. (1987) Theory of dynamic permeability and tortuosity in fluid-saturated porous media. *Journal of fluid mechanics* 176 379-402.

Korjenic, A., Petránek, V., Zach, J. and Hroudová, J. (2011) Development and performance evaluation of natural thermal-insulation materials composed of renewable resources. *Energy & Buildings* 43 (9) 2518-2523.

Kosten, C. Z. a. C. W. (1949) *Sound Absorbing Materials Elsevier.* Amsterdam:

Kymäläinen, H.-R. and Sjöberg, A.-M. (2008) Flax and hemp fibres as raw materials for thermal insulations. *Building and Environment* 43 (7) 1261-1269.

Langdon, R. v. (1982) Sudney Law Review. *The Sydney Law Review* 10 358.

Lauriks, W. (1989) *Onderzoek van de akoestische eigenschappen van gelaagde poreuze materialen. KULeuven*. PhD. thesis.

Leclaire, P., Umnova, O., Horoshenkov, K. and Maillet, L. (2003) Porosity measurement by comparison of air volumes. *Review of scientific instruments* 74 (3) 1366-1370.

Lee, J. K. and Shang, J. Q. (2013) Thermal properties of mine tailings and tire crumbs mixtures. *Construction and Building Materials* 48 (Journal Article) 636-646.

Leidner, J. (1981) Plastics Waste: Recovery of Economic Value. *MARCEL DEKKER, INC., 270 MADISON AVE., NEW YORK, NY 10016, USA*.

Li, X., Cai, Z., Winandy, J. E. and Basta, A. H. (2010) Selected properties of particleboard panels manufactured from rice straws of different geometries. *Bioresource technology* 101 (12) 4662-4666.

Maderuelo-Sanz, R., Barrigón Morillas, J. M., Martín-Castizo, M., Gómez Escobar, V. and Rey Gozalo, G. (2013) Acoustical performance of porous absorber made from recycled rubber and polyurethane resin. *Latin American Journal of Solids and Structures* 10 (3) 585-600.

Maderuelo-Sanz, R., Martín-Castizo, M. and Vílchez-Gómez, R. (2011) The performance of resilient layers made from recycled rubber fluff for impact noise reduction. *Applied Acoustics* 72 (11) 823-828.

Maderuelo-Sanz, R., Nadal-Gisbert, A. V., Crespo-Amorós, J. E. and Parres-García, F. (2012) A novel sound absorber with recycled fibers coming from end of life tires (ELTs). *Applied Acoustics* 73 (4) 402-408.

Miki, Y. (1990) Acoustic properties of porous materials – Generalization of empirical models. *J. Acoust. Soc. Jap* 11.

Olny, X. and Boutin, C. (2003) Acoustic wave propagation in double porosity media. *The Journal of the Acoustical Society of America* 114 (1) 73-89.

Olny, X. and Panneton, R. (2008) Acoustical determination of the parameters governing thermal dissipation in porous media. *The Journal of the Acoustical Society of America* 123 (2) 814-824.

Oseland, N. and Raw, G. (1991) Room size and adequacy of space in small homes. *Building and environment* 26 (4) 341-347.

P. Leclaire, M. S. a. K. V. H. (1998) Specific area from water-suction porosimetry in application to porous acoustic materials. *J. Appl. Phys* 84.

Panneton, R. and Olny, X. (2006) Acoustical determination of the parameters governing viscous dissipation in porous media. *The Journal of the Acoustical Society of America* 119 (4) 2027-2040.

Pfretzschner, J. and Mª. Rodriguez, R. (1999) Acoustic properties of rubber crumbs. *Polymer Testing* 18 (2) 81-92.

Raleigh, W. (1894) *The English novel: being a short sketch of its history from the earliest times to the appearance of Waverley.* C. Scribner's sons.

Salissou, Y. and Panneton, R. (2007) Pressure/mass method to measure open porosity of porous solids. *Journal of applied physics* 101 (12) 124913.

Seddeq, H. S., Aly, N. M., Marwa A, A. and Elshakankery, M. H. (2013) Investigation on sound absorption properties for recycled fibrous materials. *Journal of Industrial Textiles* 43 (1) 56-73.

Sgard, F. C., Olny, X., Atalla, N. and Castel, F. (2005) On the use of perforations to improve the sound absorption of porous materials. *Applied Acoustics* 66 (6) 625-651.

Sienkiewicz, M., Kucinska-Lipka, J., Janik, H. and Balas, A. (2012) Progress in used tyres management in the European Union: a review. *Waste Management* 32 (10) 1742-1751.

Sobral, M., Samagaio, A. J. B., Ferreira, J. M. F. and Labrincha, J. A. (2003) Mechanical and acoustical characteristics of bound rubber granulate. *Journal of Materials Processing Technology* 142 p. 427.

Stinson, M. R. (1991) The propagation of plane sound waves in narrow and wide circular tubes, and generalization to uniform tubes of arbitrary cross-sectional shape. *The Journal of the Acoustical Society of America* 89 (2) 550-558.

Stinson, M. R. and Champoux, Y. (1992) Propagation of sound and the assignment of shape factors in model porous materials having simple pore geometries. *The Journal of the Acoustical Society of America* 91 (2) 685-695.

Swift, M., Horoshenkov, K., Leclaire, P., Hothersall, D., Fujiwara, K. and Torihama, H. (2000) On the effect of the bending vibration on the acoustic properties of thin poroelastic plates. *The Journal of the Acoustical Society of America* 107 (3) 1786-1789.

Swift, M. J., Bris, P. and Horoshenkov, K. V. (1998) Acoustic absorption in re-cycled rubber granulate. *Applied Acoustics* 57 203-212.

Swift, M. J., Bris, P. and Horoshenkov, K. V. (1999) Acoustic absorption in re-cycled rubber granulate. *Applied Acoustics* 57 (3) 203-212.

Tiuc, A.-E., Vermeşan, H., Gabor, T. and Vasile, O. (2016) Improved sound absorption properties of polyurethane foam mixed with textile waste. *Energy Procedia* 85 559-565.

Turgut, P. and Yesilata, B. (2008) Physico-mechanical and thermal performances of newly developed rubber-added bricks. *Energy & Buildings* 40 (5) 679-688.

Vitamvasova E, V. S., Gerza D, Bris P (1996) A noise and vibration protection by mixed polymer waste. In *Inter noise '96.* 1835-1839.

Yamamoto, T. (1988) Acoustic wave propagation through porous media with arbitrary pore size distributions. *The Journal of the Acoustical Society of America* 83 (5) 1744.

Zhang, R., Feng, J., Cheng, X., Gong, L., Li, Y. and Zhang, H. (2014) Porous thermal insulation materials derived from fly ash using a foaming and slip casting method. *Energy and Buildings* 81 (Journal Article) 262-267.

Zhou, X.-y., Zheng, F., Li, H.-g. and Lu, C.-l. (2010) An environment-friendly thermal insulation material from cotton stalk fibers. *Energy & Buildings* 42 (7) 1070-1074.

Zwikker, C. and Kosten, C. W. (1949) *Sound absorbing materials.* Elsevier.

Appendices

Appendix A:

These figures represent some of random cell pore size materials formula optimisation

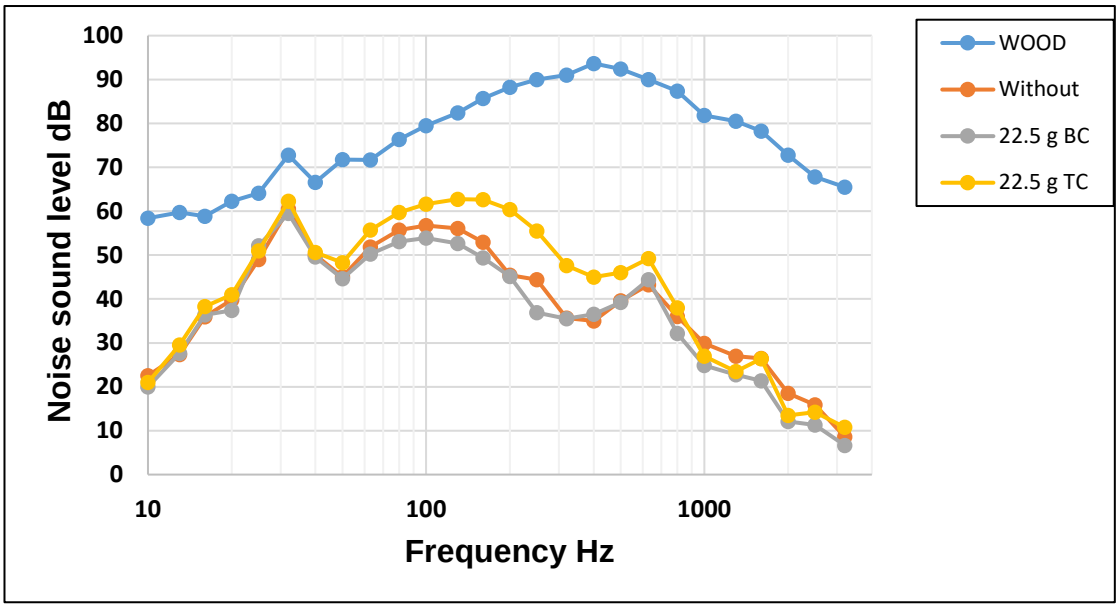

Figure A- 1. The effect of adding 22.5 grams of different kinds of crumb rubber on the acoustical properties of underlay materials

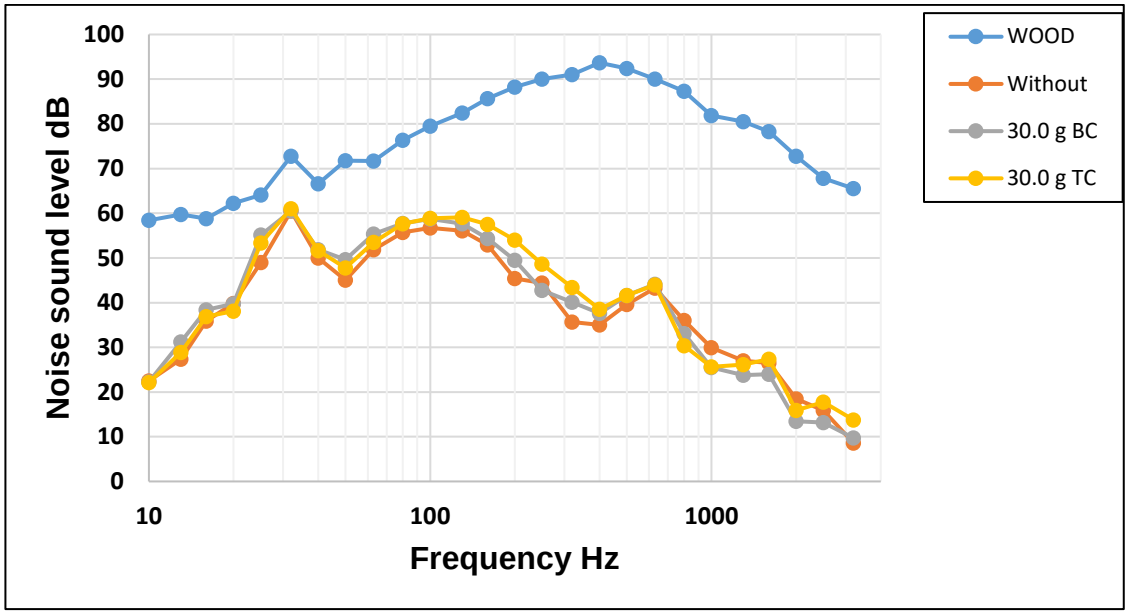

Figure A- 2. The effect of adding 30 grams of different kinds of crumb rubber on acoustical performance of underlay materials.

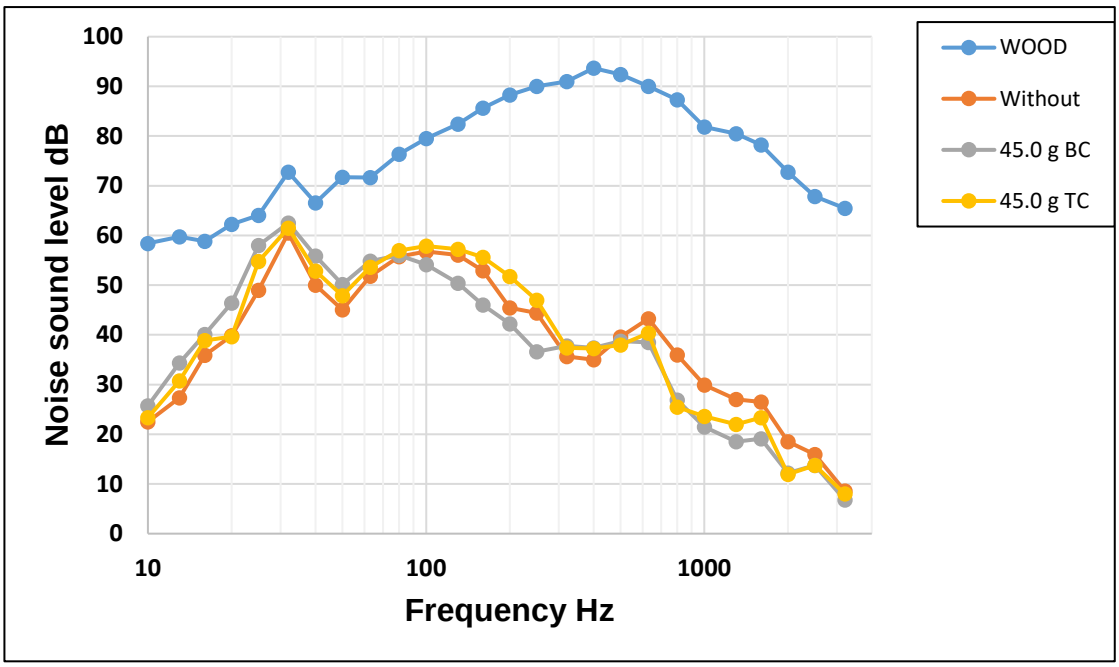

Figure A- 3. The effect of adding 45 grams of different kinds of crumb rubber on acoustical performance of underlay materials.

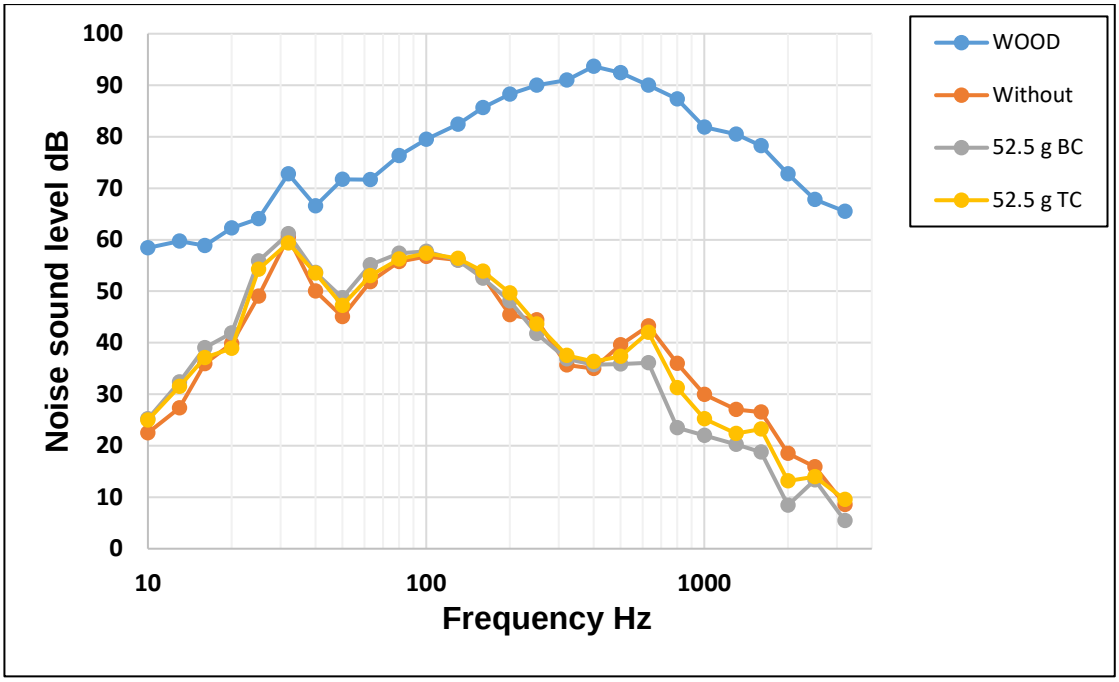

Figure A- 4. The effect of adding 52.5 grams of different kinds of crumb rubber on acoustical performance of underlay materials.

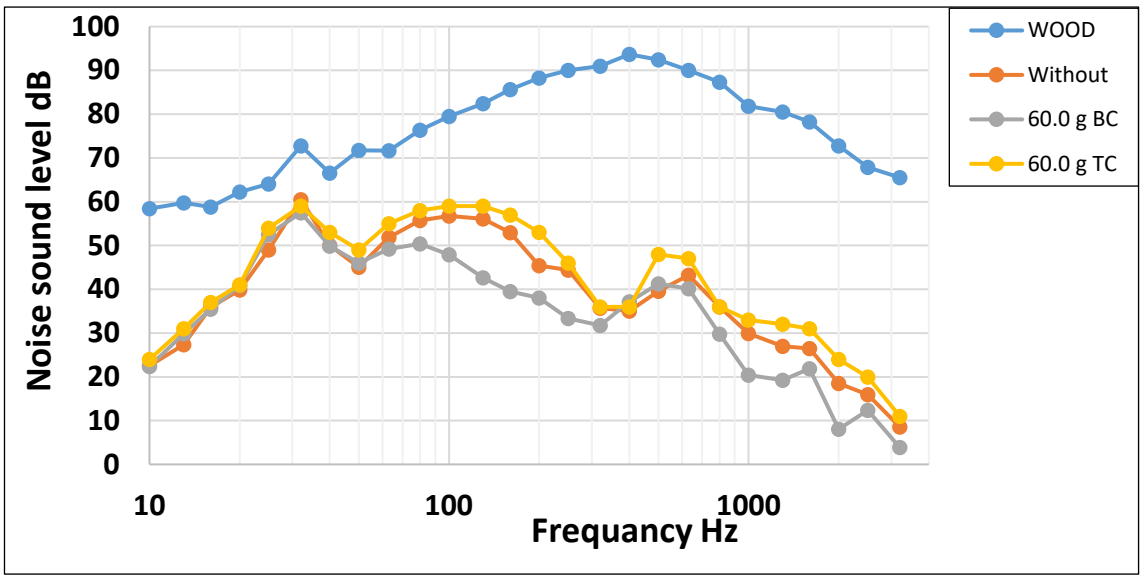

Figure A- 5. The effect of adding 60 grams of different kinds of crumb rubber on acoustical performance of underlay materials.

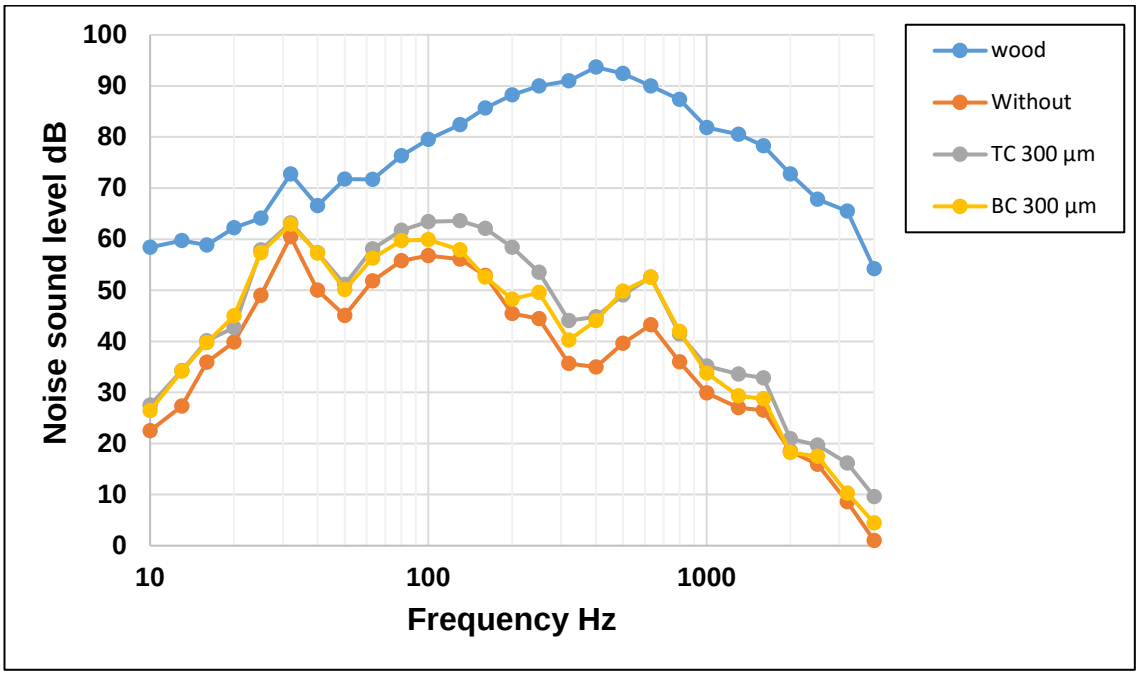

Figure A- 6. The effect of crumb rubber kinds for the same size 300µm on acoustical performance of underlay materials.

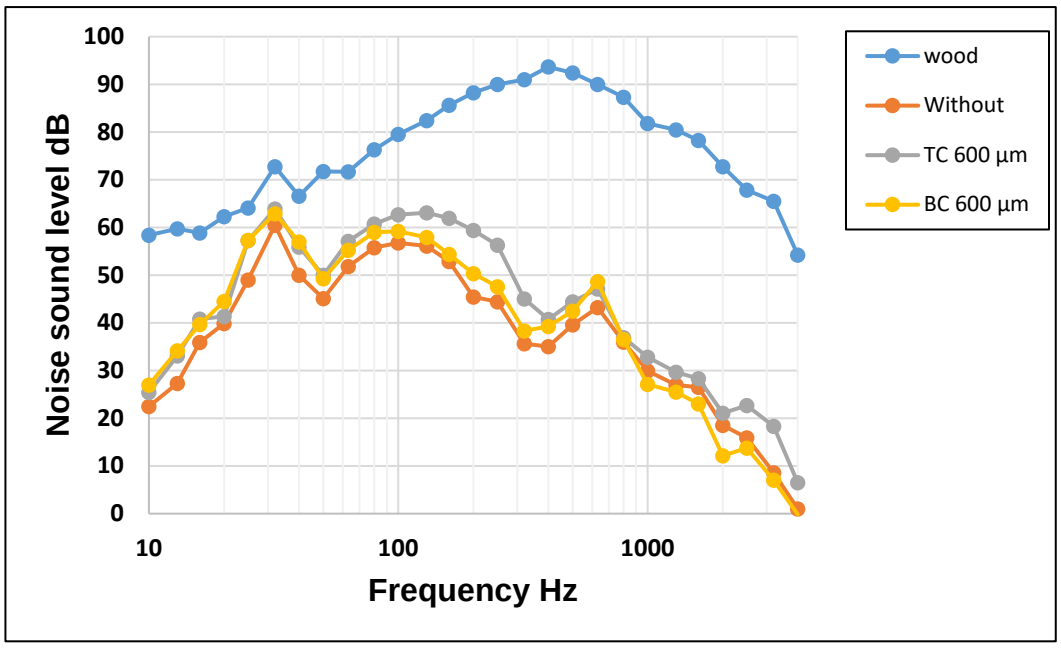

Figure A- 7. The effect of crumb rubber kinds of the same size 600 µm on acoustical performance of underlay materials.

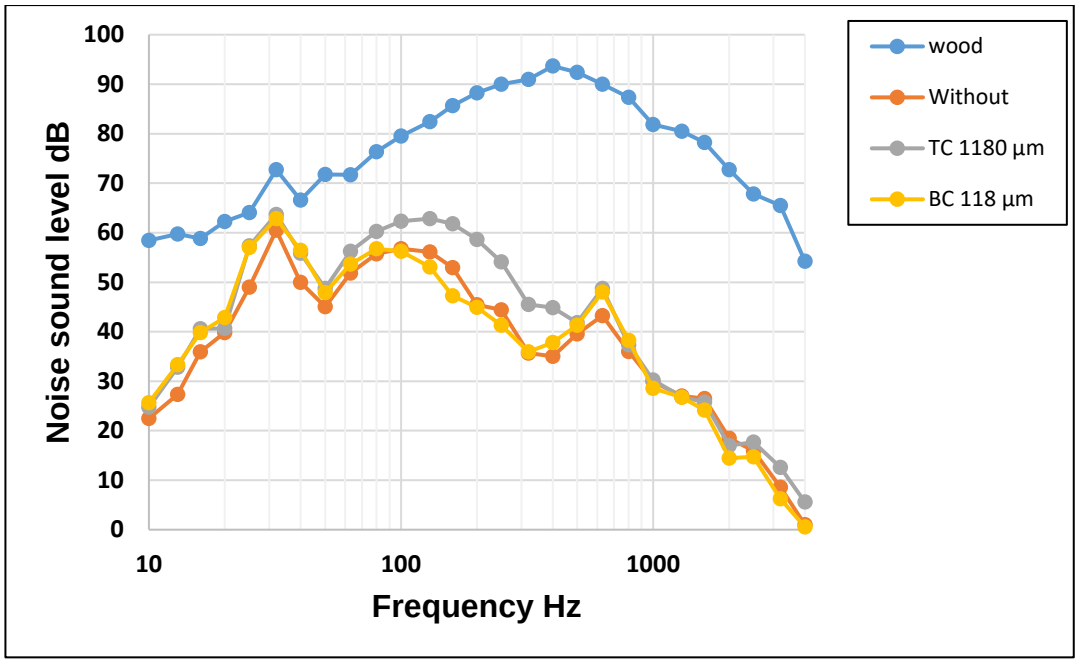

Figure A- 8. The effect of crumb rubber kinds for the same size 1180 µm on acoustical performance of underlay materials.

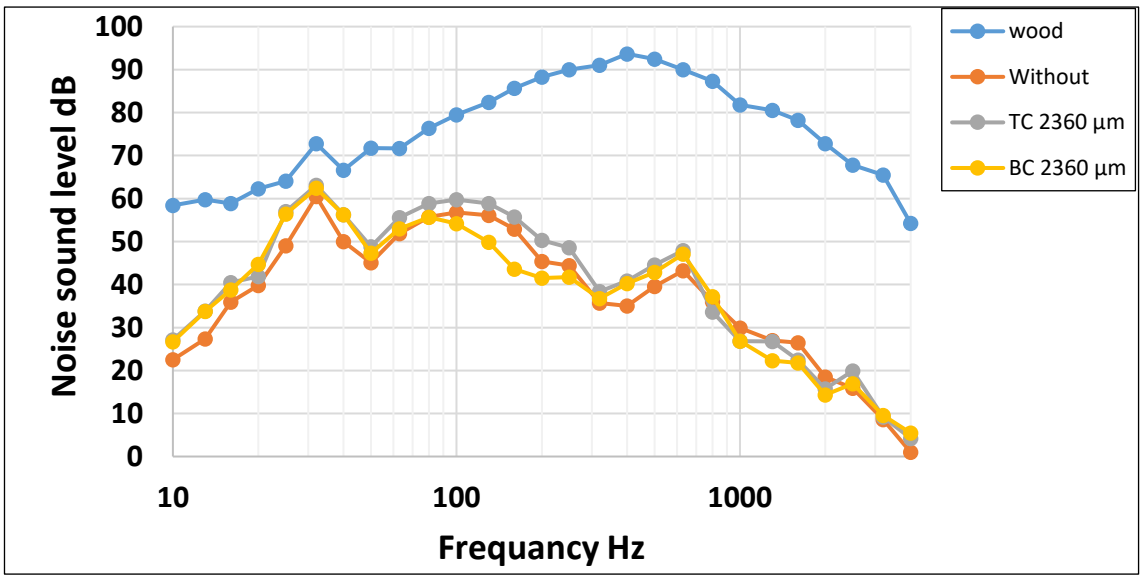

Figure A- 9. The effect of crumb rubber kind for the same size 2360 µm on acoustical performance of underlay materials.

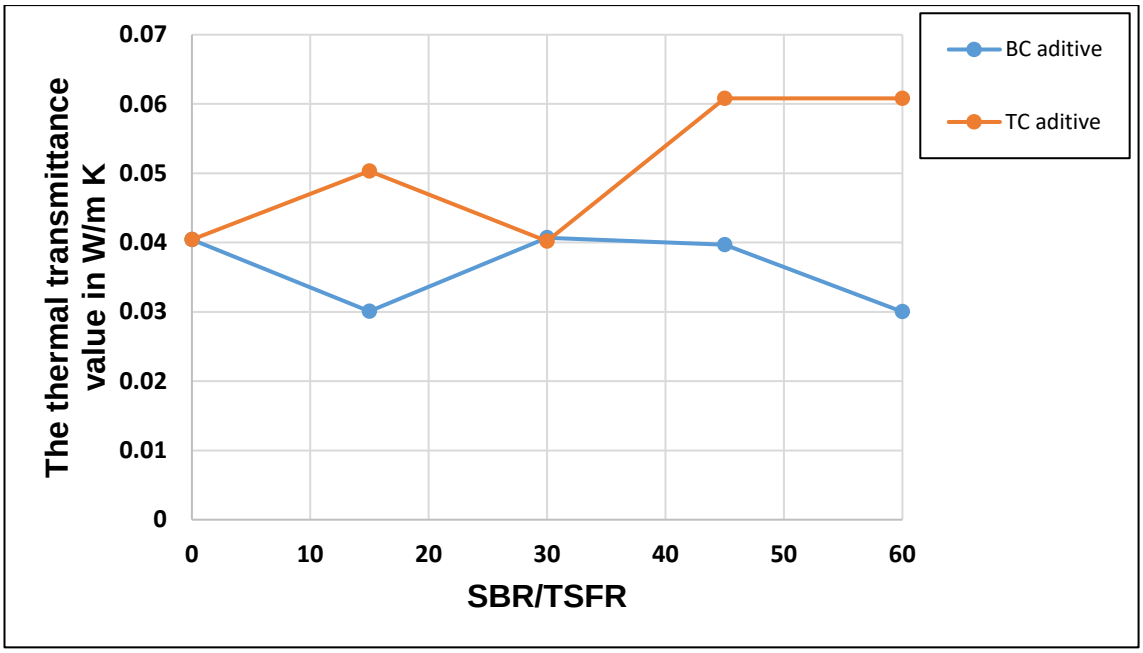

Figure A- 10 The effect of crumb rubber kind on thermal condactivity of SBR/TFSR underlay materials.

Appendix B

This section contains values of acoustical and non-acoustical parameters of atmospheric and vacuumed insulation materials according to JSA model, with figures of each 30 mm thickness slid of produced samples. These samples have been labelled from the base side as the 1st slid and the second 30 mm thickness slid is the 2nd etc. The tables contain the values of predicted and measured acoustical and non-acoustical insulation parameters according to JSA model for each applied pressure value.

B1: These results of the atmospheric insulation samples.

Table B-1 the experimental and predicted of non-acoustical parameters values of atmospheric polyurethane insulation sample

Slabs of Atm Press	σ (exp.) (Pa.s/m^2)	σ (pred.) (Pa.s/m^2)	ϕ (exp.)	ϕ (pred.)	α_∞ (exp.)	α_∞ (pred.)	Density (Kg/m^3)	Thickness (m)	Λ (µm) (predicted)	Λ' (µm) (predicted)
1st	34400	92,777	0.74	0.935	1.162	1.11	127	0.03	6.9	343.9
2nd	27894	58,958	0.75	0.874	1.158	1.742	121	0.03	20.4	20.4
3rd	22342	50,014	0.75	0.873	1.152	2.349	118	0.03	43.4	43.4
4th	19785	44,266	0.76	0.899	1.148	2.859	114	0.03	41.5	236.3

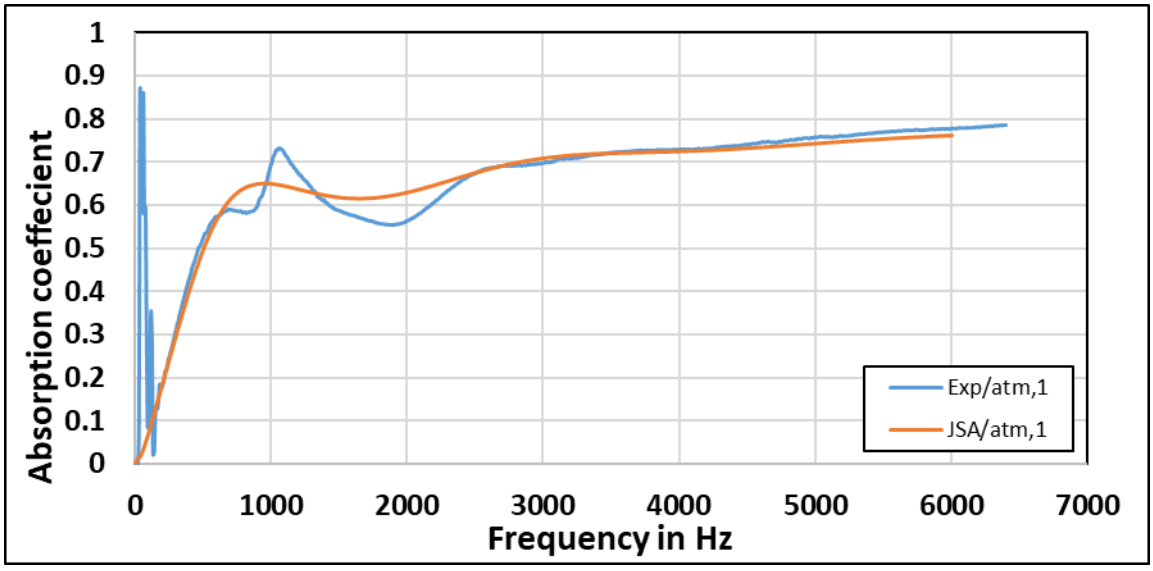

Figure B1- 1. The experimental and theoretical absorption curves of the 1st 30 mm thickness slab of atmospheric pressure sample.

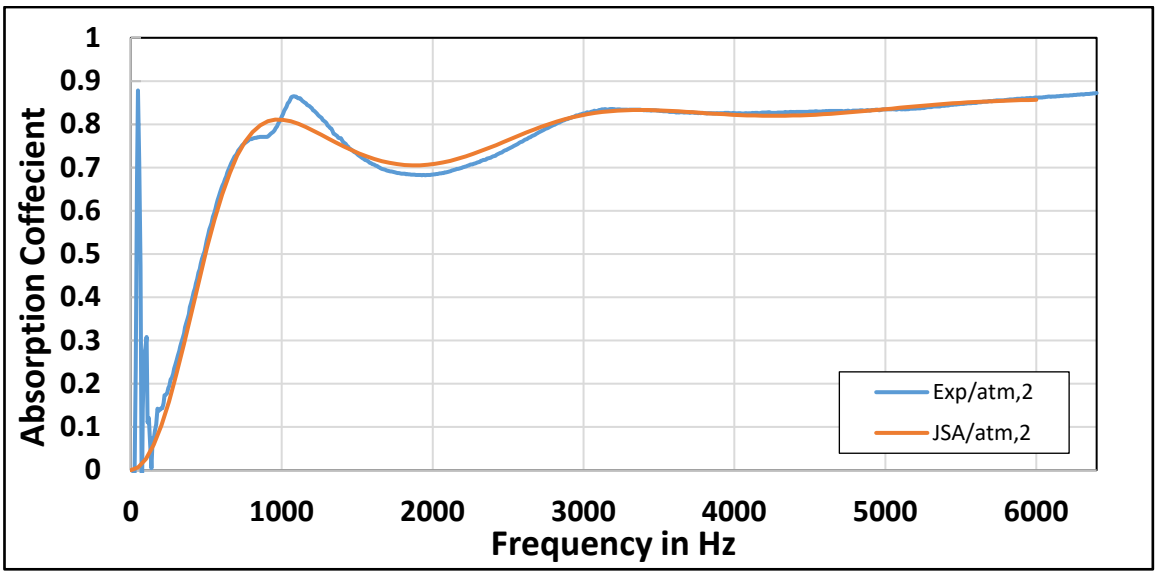

Figure B1- 2. The experimental and theoretical absorption curves of the 2nd 30 mm thickness slab of atmospheric pressure sample.

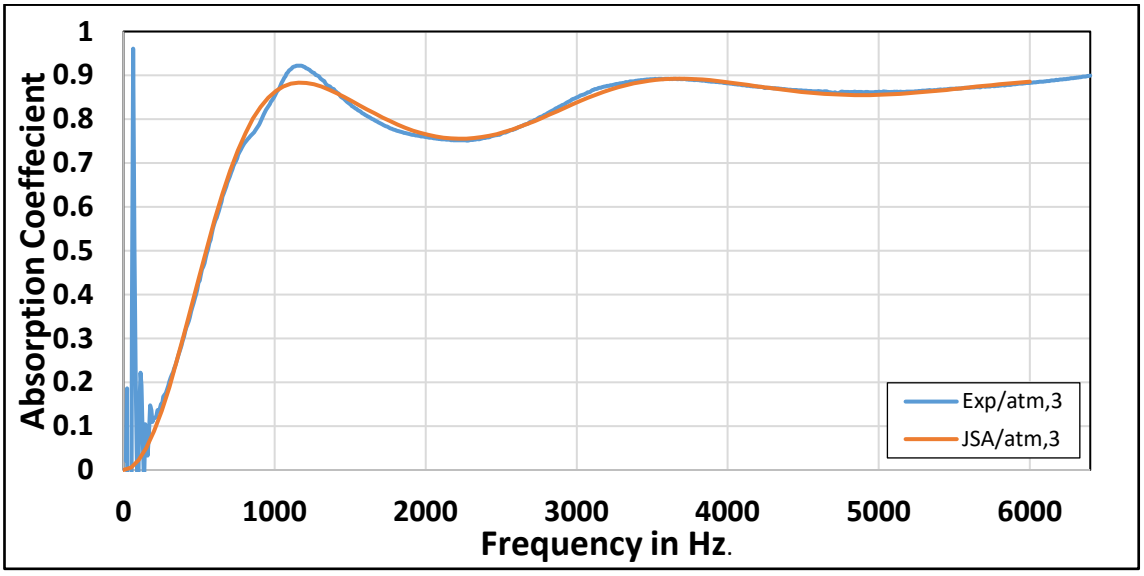

Figure B1- 3. The experimental and theoretical absorption curves of the 3rd 30 mm thickness slab of atmospheric pressure sample.

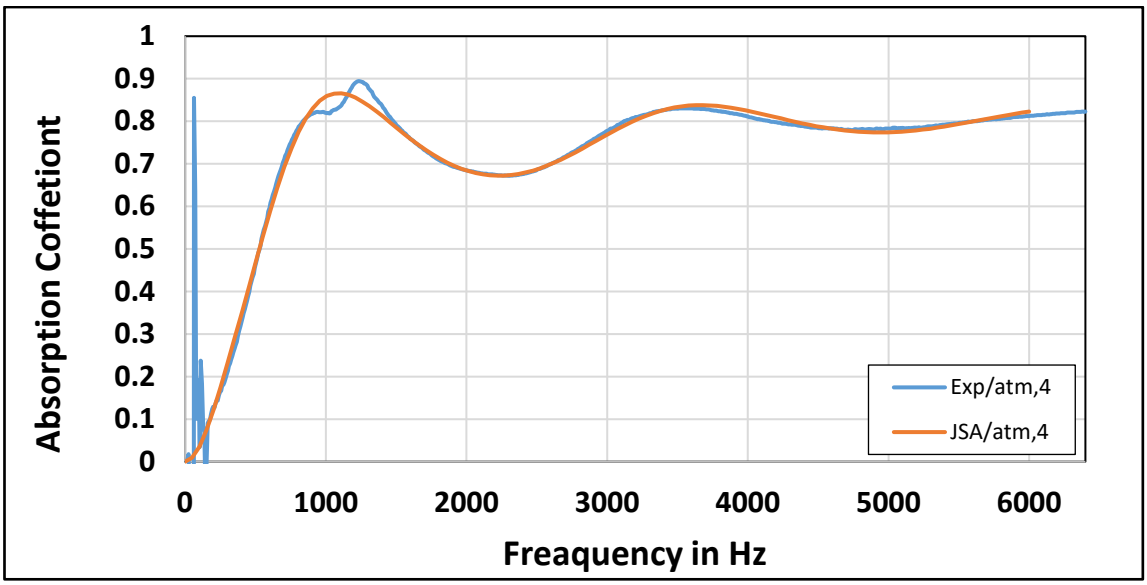

Figure B1- 4. The experimental and theoretical absorption curves of the 4th 30 mm thickness slab of atmospheric pressure sample.

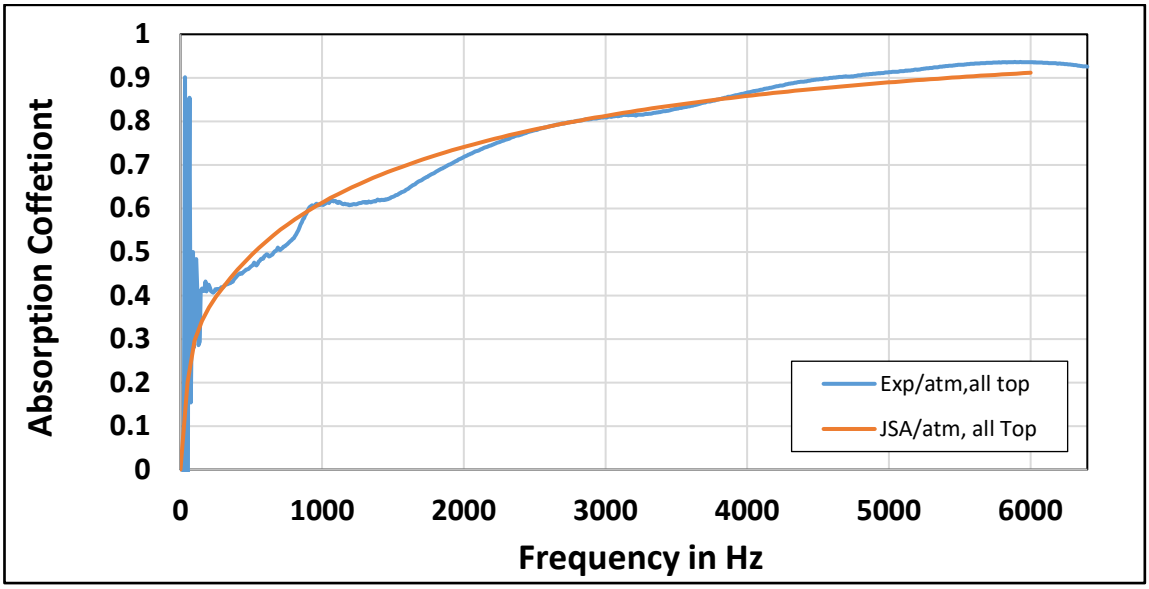

Figure B1- 5. The experimental and theoretical absorption curves of the 120 mm thickness of atmospheric pressure sample, the direction of the wave with the same pores growing direction

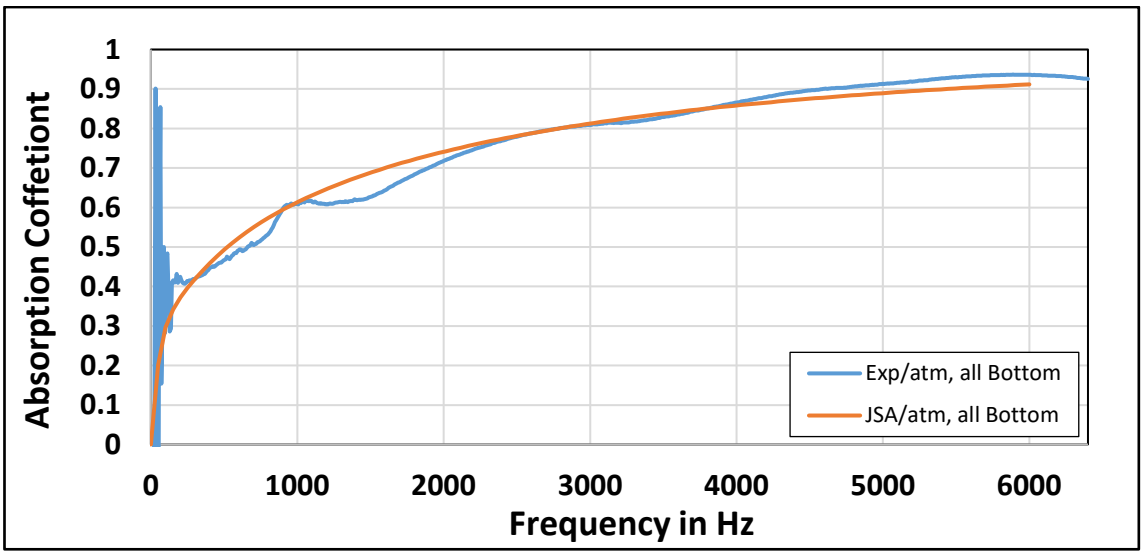

Figure B1- 6. The experimental and theoretical absorption curves of the 120 mm thickness of atmospheric pressure sample, the direction of the wave with the obverse pores growing direction

B2: These results of the -5 in Hg vacuumed insulation samples.

Table B-2. The experimental and predicted non-acoustical properties of -5 in Hg vacuumed polyurethane insulation.

Slabs of -5inHg	σ **(exp.) (Pa.s/m^2)**	σ **(pred.) (Pa.s/m^2)**	ϕ **(exp.)**	ϕ **(pred.)**	α_∞ **(exp.)**	α_∞ **(pred.)**	**Density (Kg/m^3)**	**Thick. (m)**	Λ **(µm) (pred.)**	Λ' **(µm) (pred.)**
1st	27647	1,937	0.912	0.999	2.468	2.319	112.25	0.03	69.9	505.9
2nd	23765	2,205	0.915	0.999	2.26	2.423	105.92	0.03	93.9	462.1
3rd	21972	3,145	0.945	0.96	2.689	2.296	105.74	0.03	105.4	344.7
4th	18745	6,510	0.925	0.999	2.551	2.436	105.67	0.03	113.7	381.8

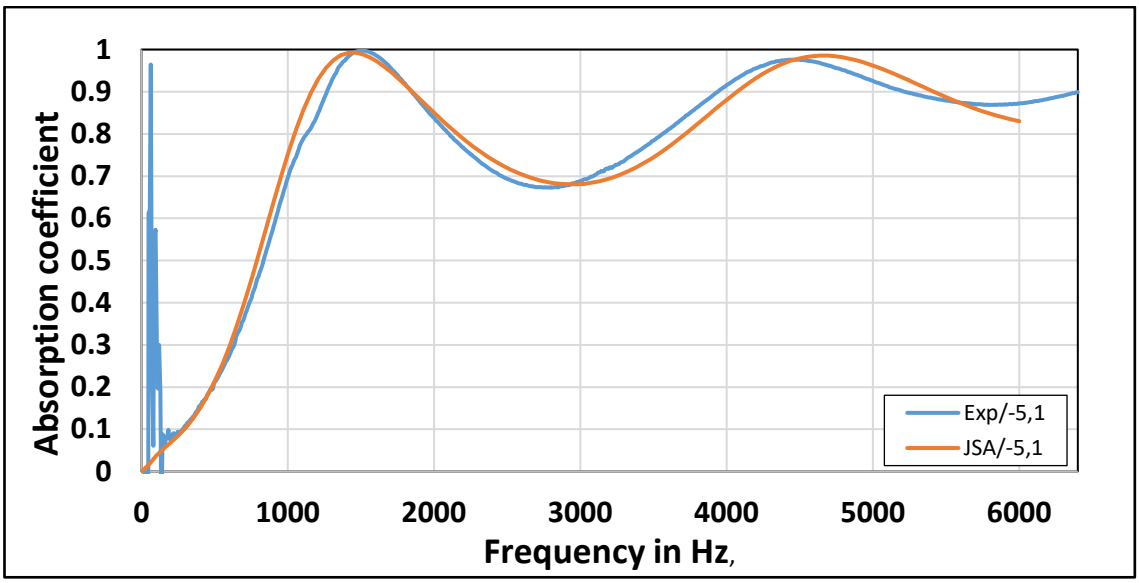

Figure B2- 1. The experimental and theoretical absorption curves of the 1st 30 mm thickness slab of -5 in Hg vacuumed pressure sample.

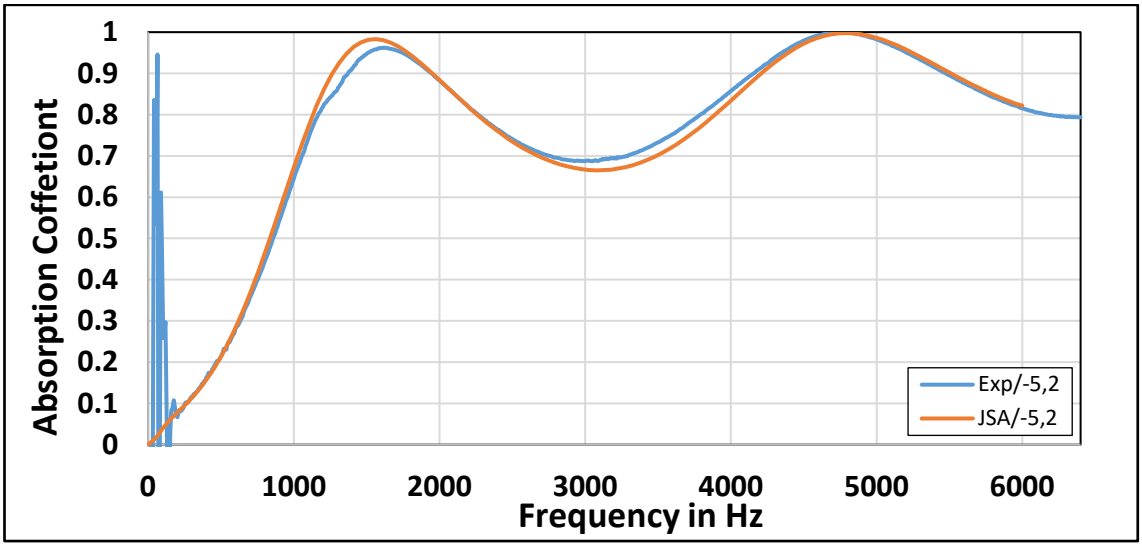

Figure B2- 2. The experimental and theoretical absorption curves of the 2nd 30 mm thickness slab of -5 in Hg vacuumed pressure sample.

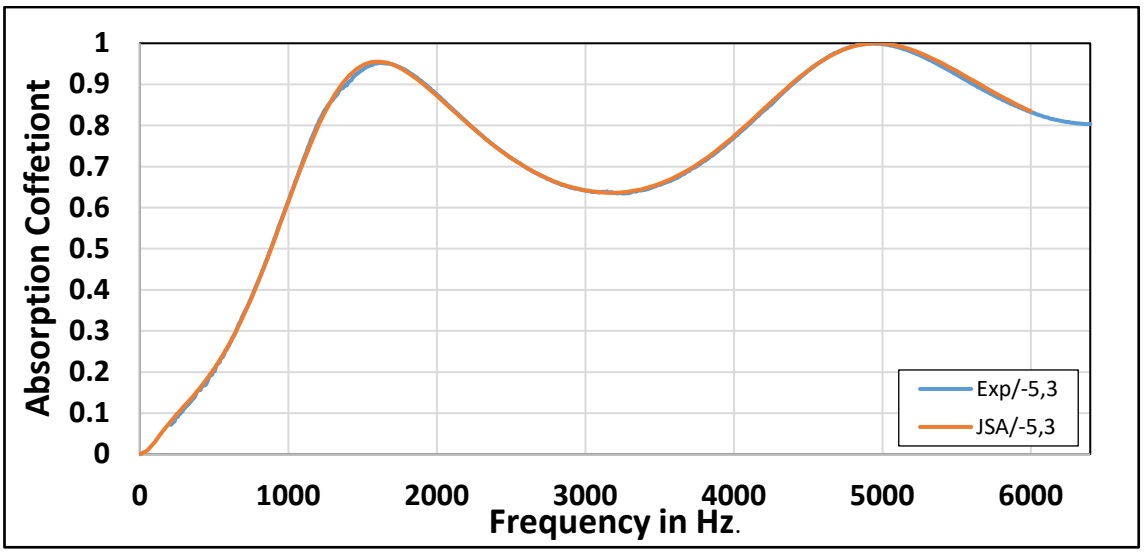

Figure B2- 3. The experimental and theoretical absorption curves of the 3rd 30 mm thickness slab of -5 in Hg vacuumed pressure sample.

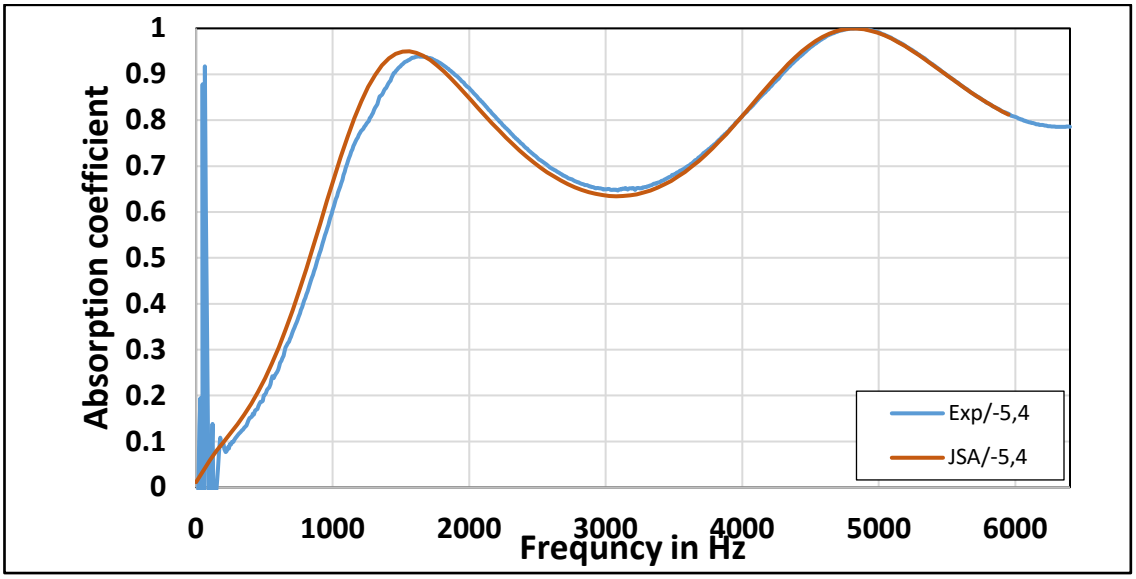

Figure B2- 4. The experimental and theoretical absorption curves of the 4th 30 mm thickness slab of-5 in Hg vacuumed pressure sample.

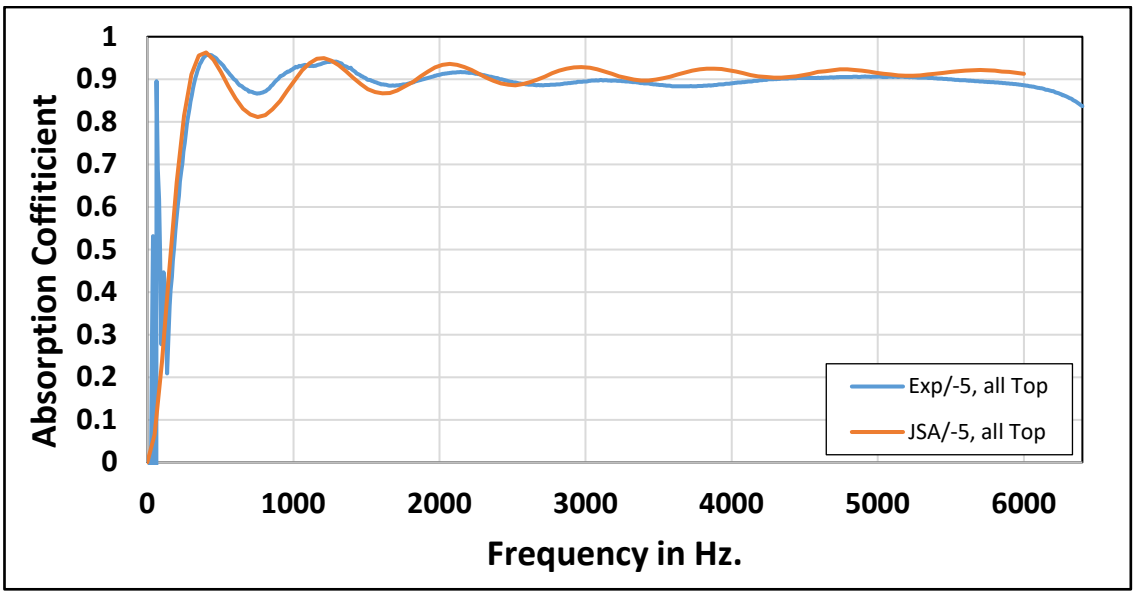

Figure B2- 5. The experimental and theoretical absorption curves of the 120 mm thickness of -5 in Hg vacuumed pressure sample, the direction of the wave with the same pores growing direction.

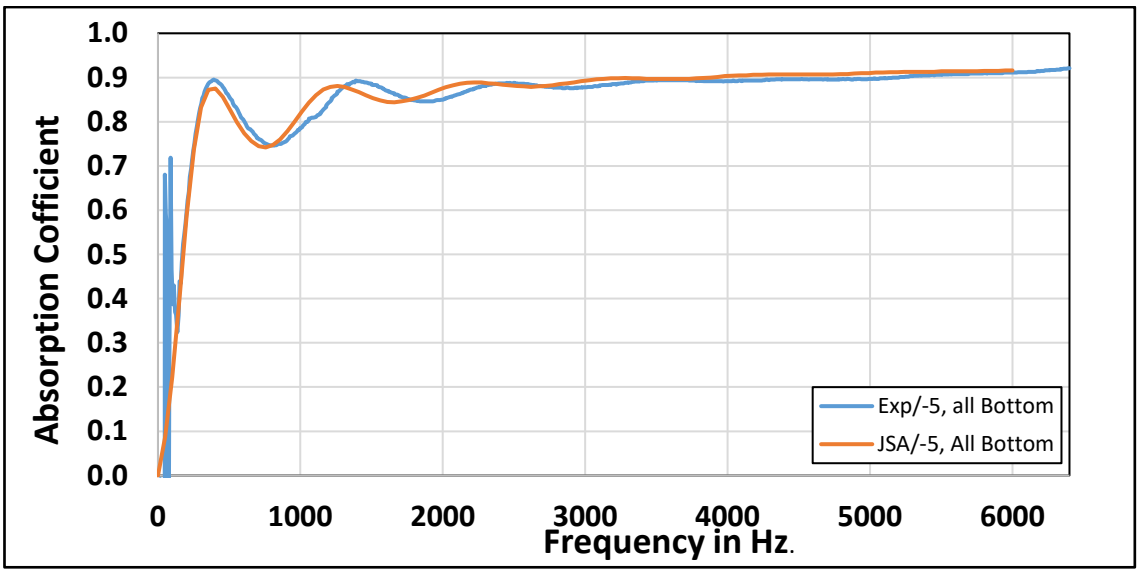

Figure B2- 6. The experimental and theoretical absorption curves of the 120 mm thickness of -5 in Hg vacuumed pressure sample, the direction of the wave with the obverse pores growing direction.

B3: These results of the -10 in Hg vacuumed insulation samples.

Table B-3. The experimental and predicted non-acoustical parameters of -10 in Hg vacuumed polyurethane insulation samples.

Slabs of -10inHg	σ **(exp.) (Pa.s/m^2)**	σ **(pred.) (Pa.s/m^2)**	ϕ **(exp.)**	ϕ **(pred.)**	α_∞ **(exp.)**	α_∞ **(pred.)**	**Density (Kg/m^3)**	**Thick. (m)**	Λ **(µm) (pred.)**	Λ' **(µm) (pred.)**
1st	27545	4,866	0.917	0.939	3.044	2.175	98.93	0.03	83.1	391.1
2nd	17566	4,229	0.919	0.999	2.277	2.12	92.46	0.03	129.7	425.6
3rd	16435	5,474	0.921	0.95	2.087	1.936	92.06	0.03	137.5	438.7
4th	14884	3,506	0.927	0.999	2.133	1.873	91.83	0.03	132.6	432.5

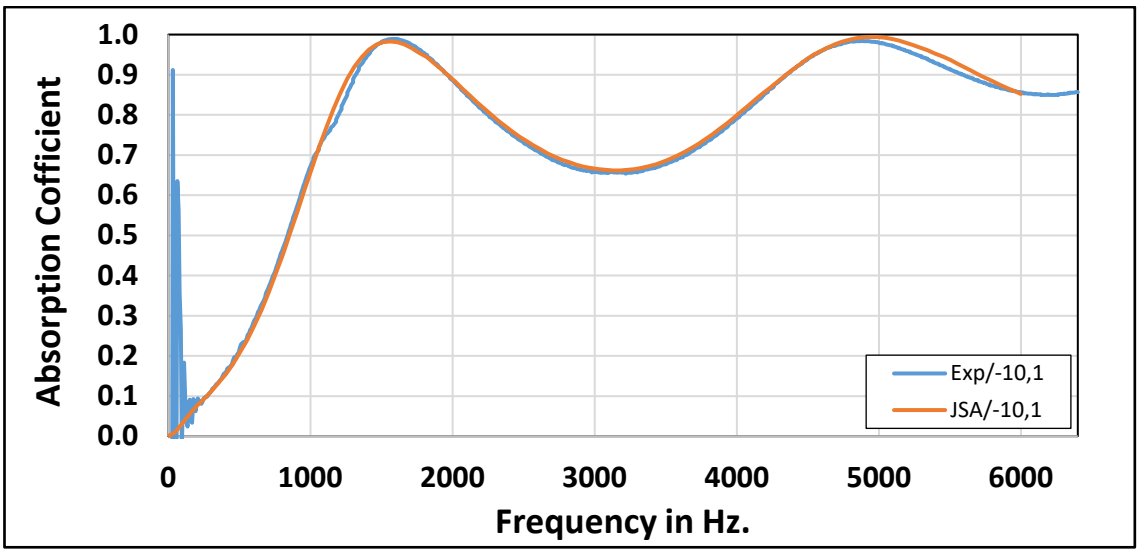

Figure B3- 1. The experimental and theoretical absorption curves of the 1st 30 mm thickness slab of-10 in Hg vacuumed pressure sample.

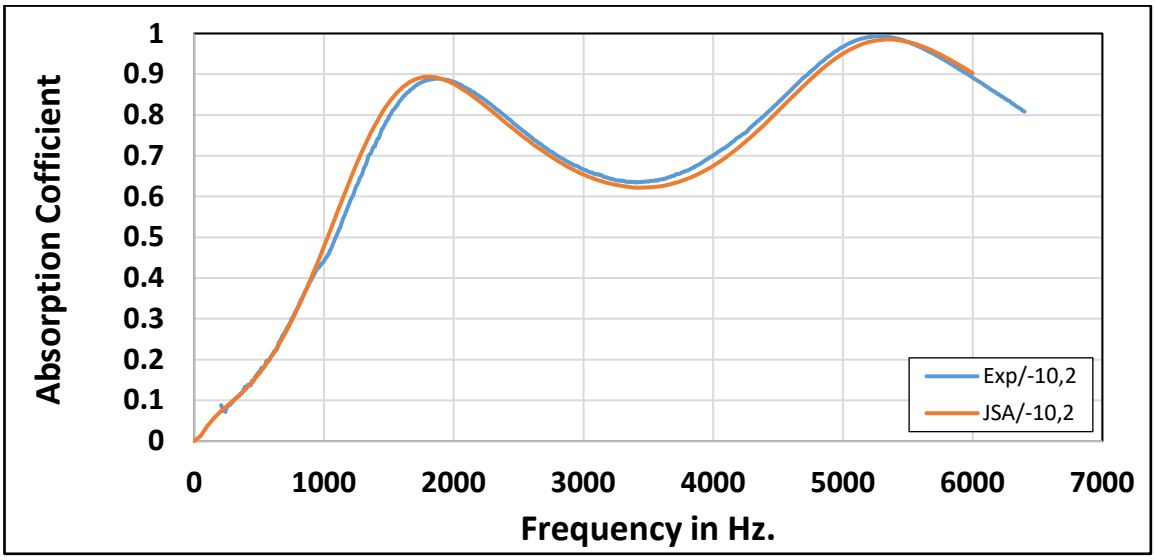

Figure B3- 2. The experimental and theoretical absorption curves of the 2nd 30 mm thickness slab of -10 in Hg vacuumed pressure sample.

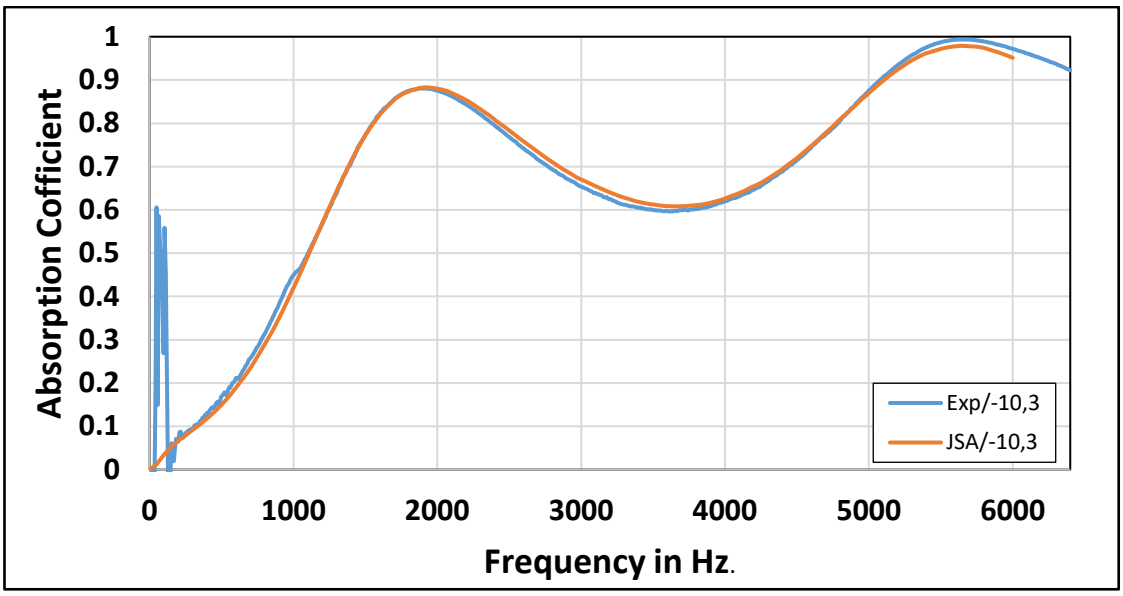

Figure B3- 3. The experimental and theoretical absorption curves of the 3rd 30 mm thickness slab of -10 in Hg vacuumed pressure sample.

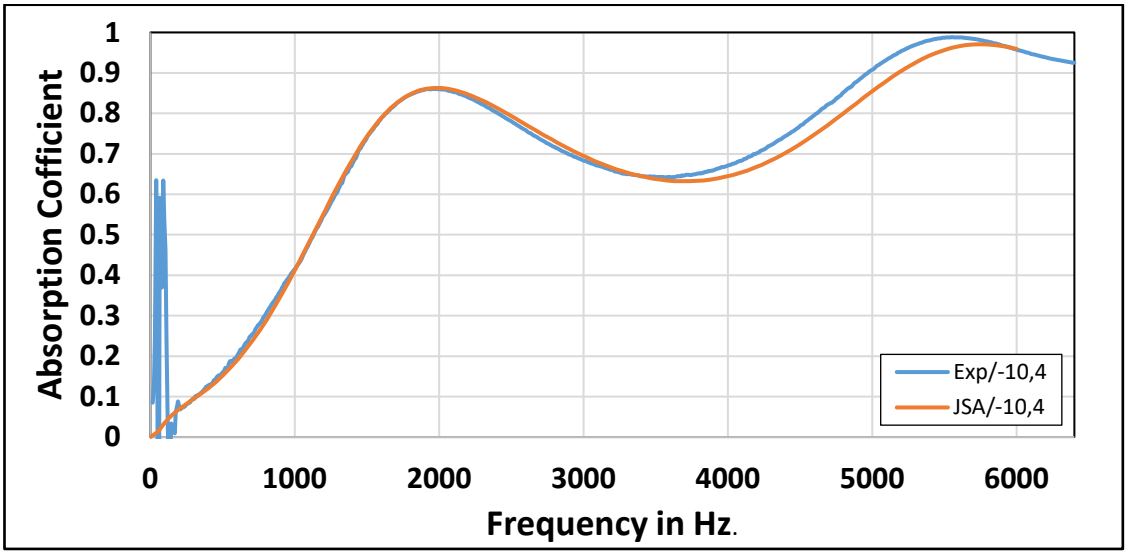

Figure B3- 4. The experimental and theoretical absorption curves of the 4th 30 mm thickness slab of -10 in Hg vacuumed pressure sample.

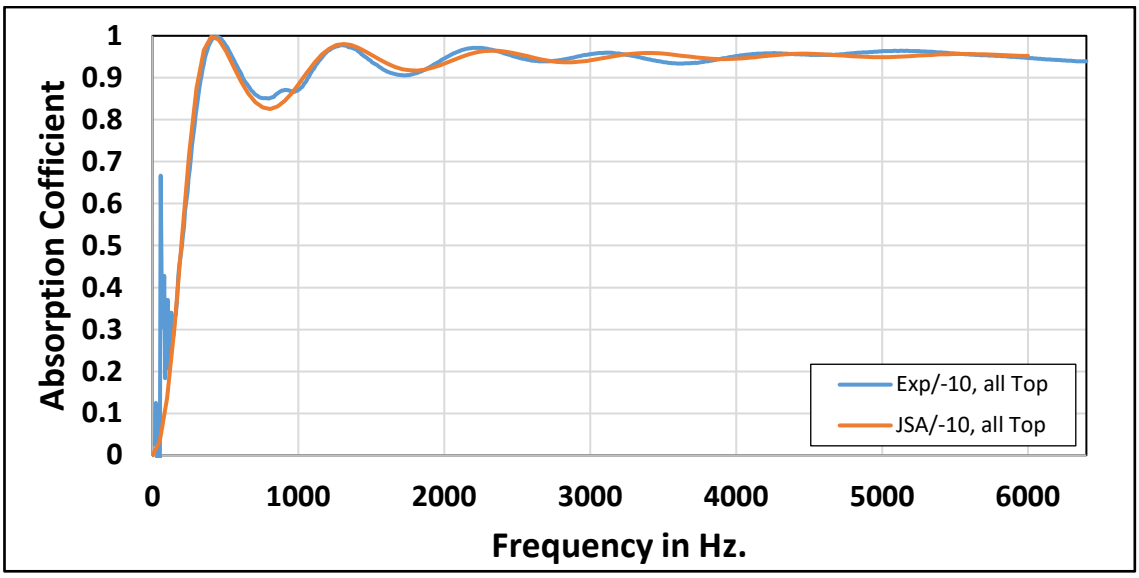

Figure B3- 5. The experimental and theoretical absorption curves of the 120 mm thickness of -10 in Hg vacuumed pressure sample, the direction of the wave with the same pores growing direction.

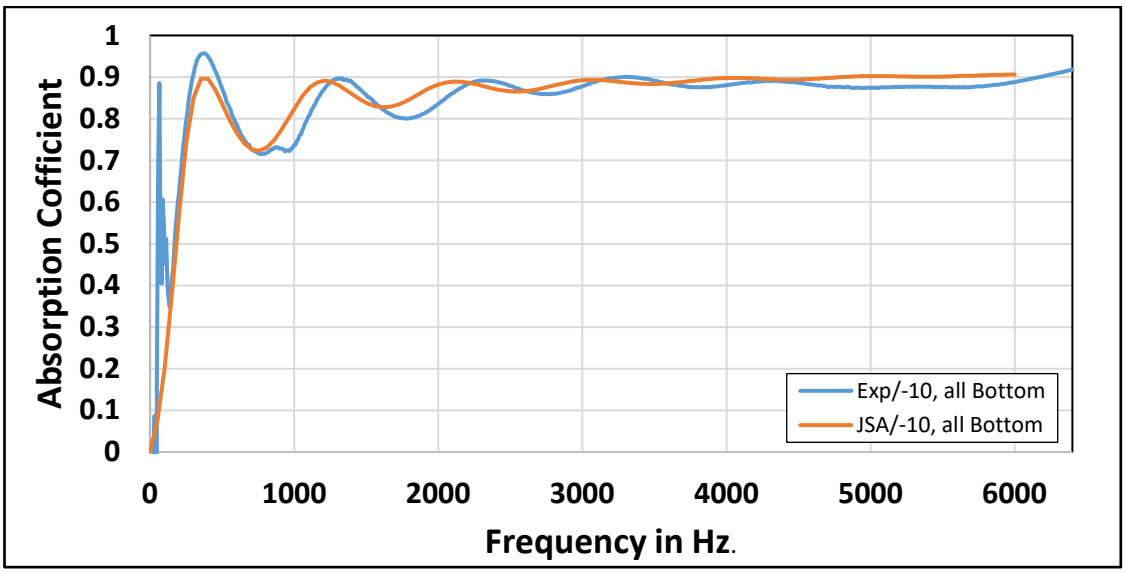

Figure B3- 6. The experimental and theoretical absorption curves of the 120 mm thickness of -10 in Hg vacuumed pressure sample, the direction of the wave with the obverse pores growing direction.

B4: These results of the -15 in Hg vacuumed insulation samples.

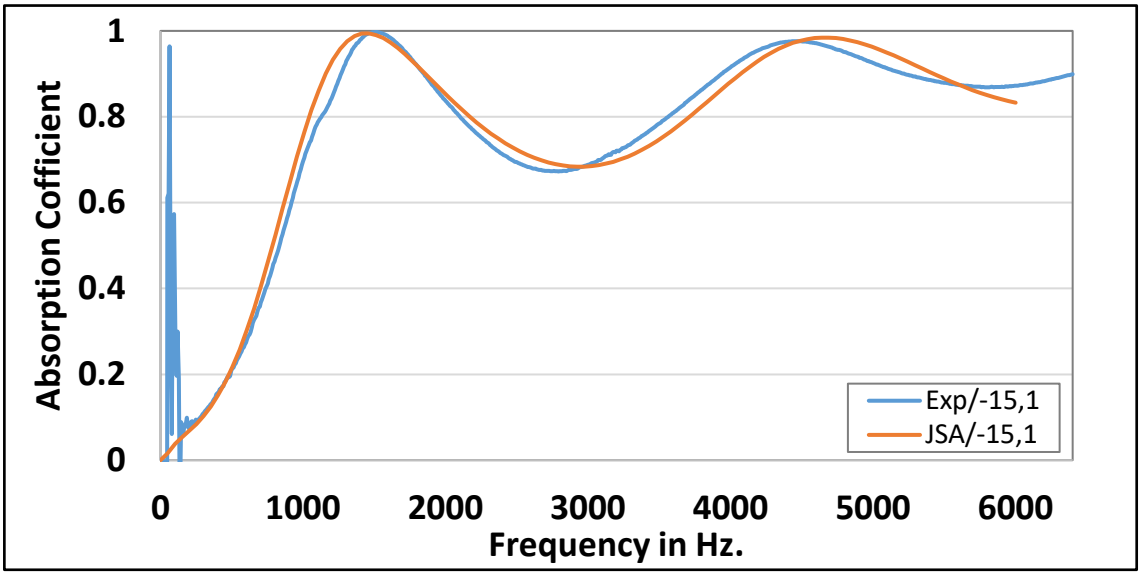

Figure B4- 1. The experimental and theoretical absorption curves of the 1st 30 mm thickness slab of-15 in Hg vacuumed pressure sample.

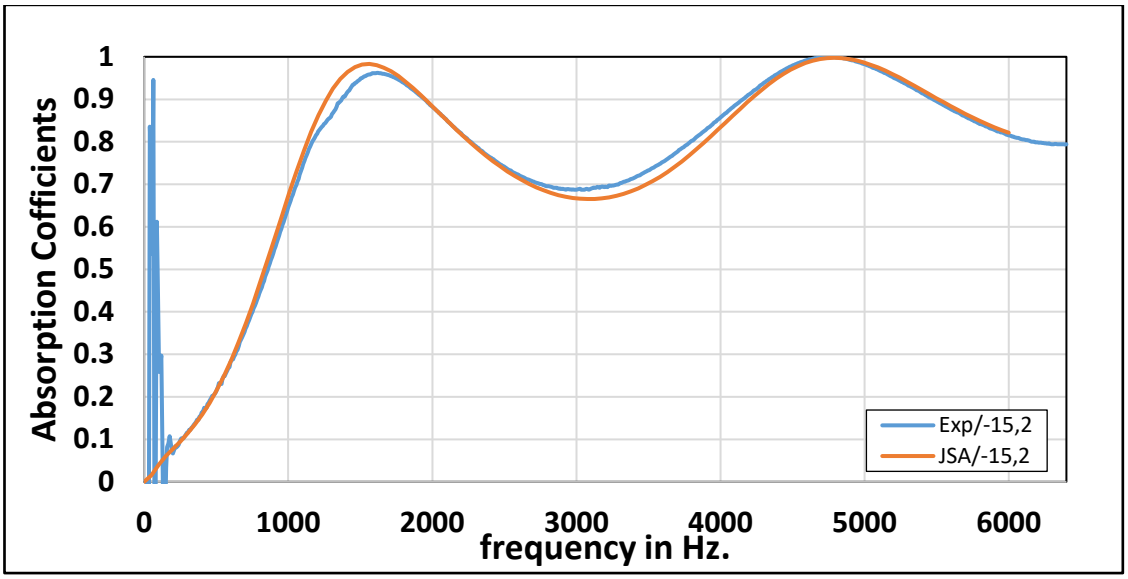

Figure B4- 2. The experimental and theoretical absorption curves of the 2nd 30 mm thickness slab of-15 in Hg vacuumed pressure sample.

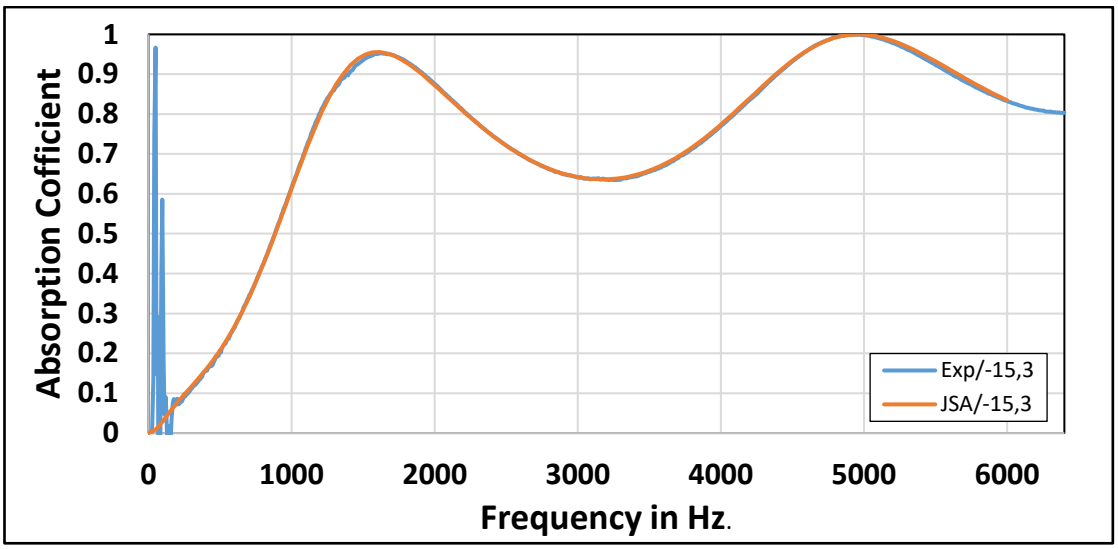

Figure B4- 3. The experimental and theoretical absorption curves of the 3rd 30 mm thickness slab of-15 in Hg vacuumed pressure sample.

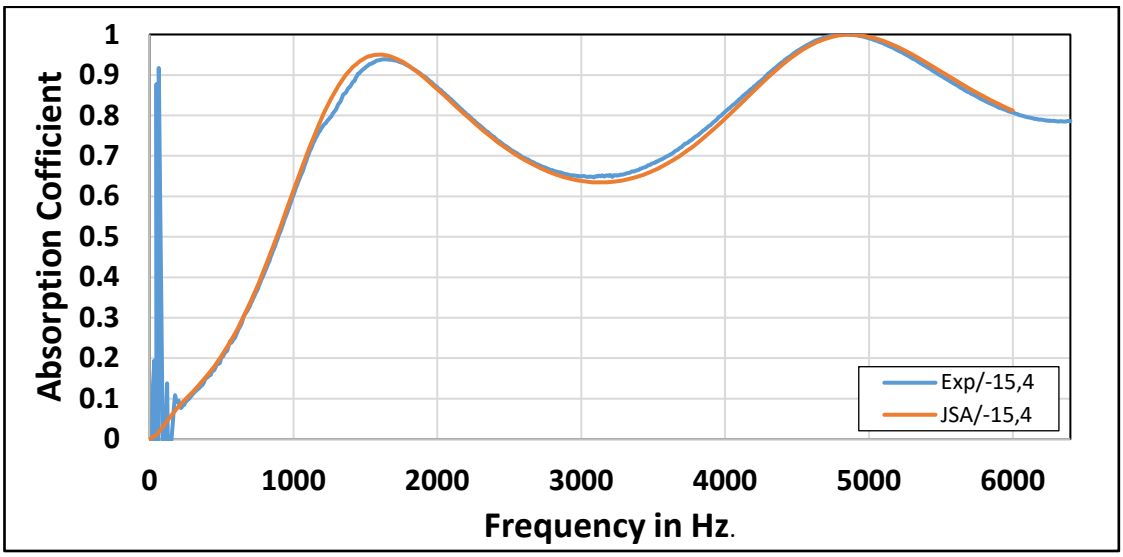

Figure B4- 4. The experimental and theoretical absorption curves of the 4th 30 mm thickness slab of-15 in Hg vacuumed pressure sample.

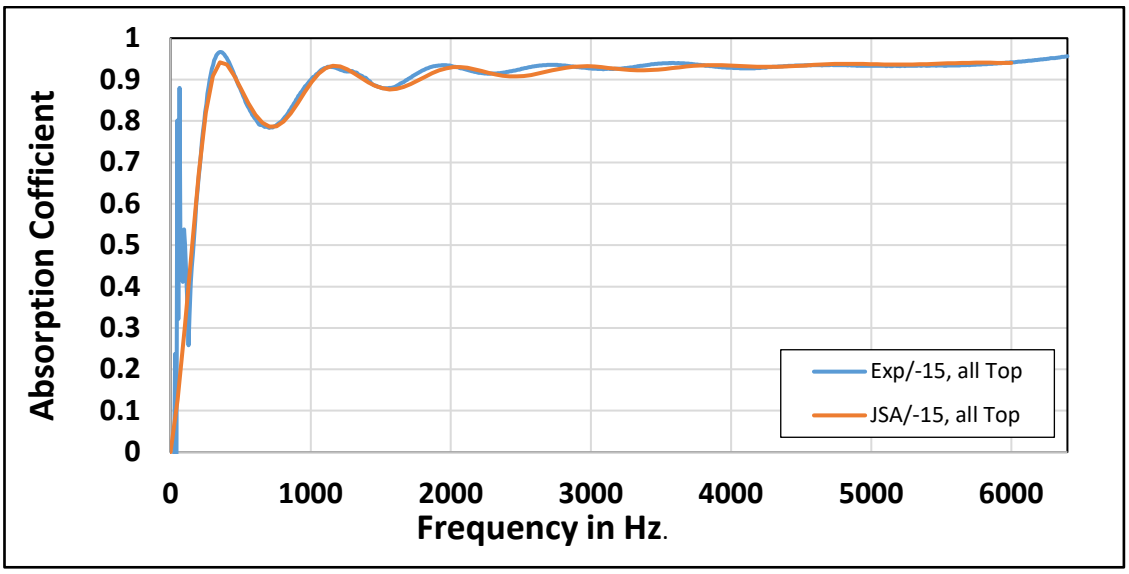

Figure B4- 5. The experimental and theoretical absorption curves of the 120 mm thickness of -15 in Hg vacuumed pressure sample, the direction of the wave with the same pores growing direction.

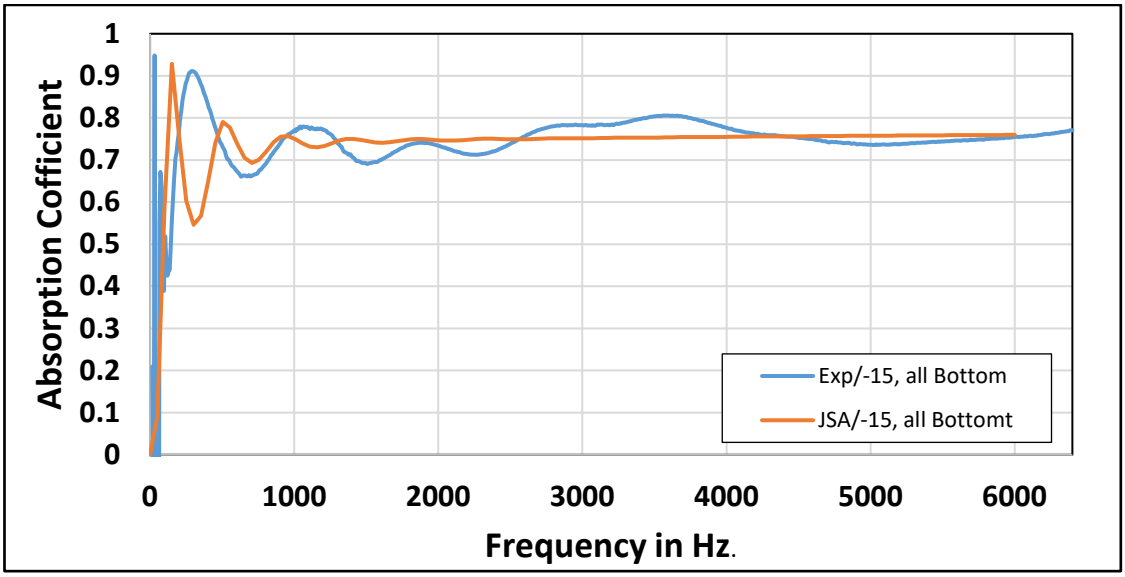

Figure B4- 6. The experimental and theoretical absorption curves of the 120 mm thickness of -15 in Hg vacuumed pressure sample, the direction of the wave with the obverse pores growing direction

B5: These results of the -20 in Hg vacuumed insulation samples.

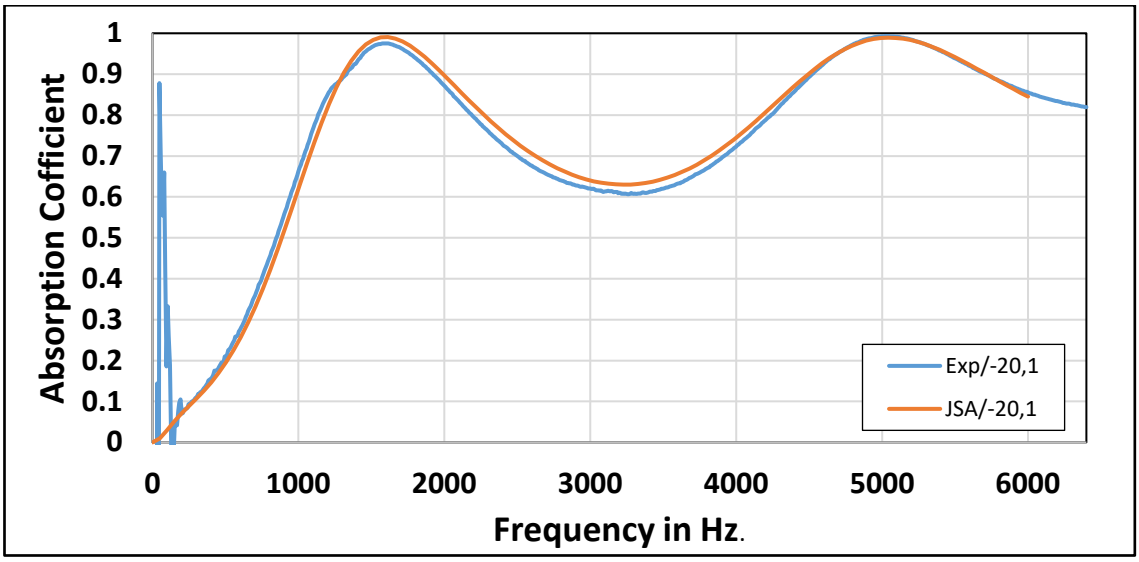

Figure B5- 1. The experimental and theoretical absorption curves of the 1st 30 mm thickness slab of -20 in Hg vacuumed pressure sample.

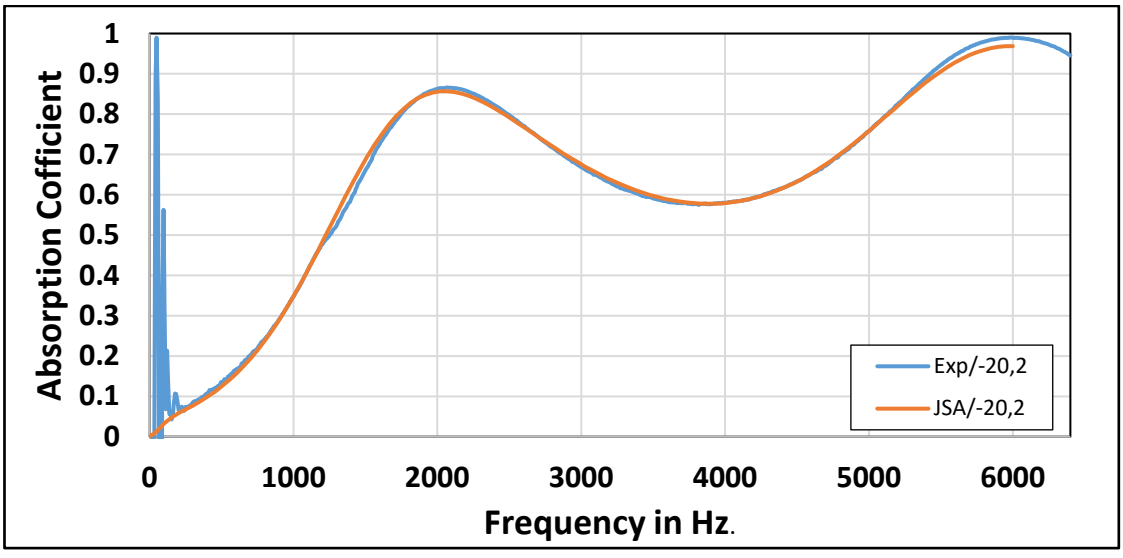

Figure B5- 2. The experimental and theoretical absorption curves of the 2nd 30 mm thickness slab of -20 in Hg vacuumed pressure sample.

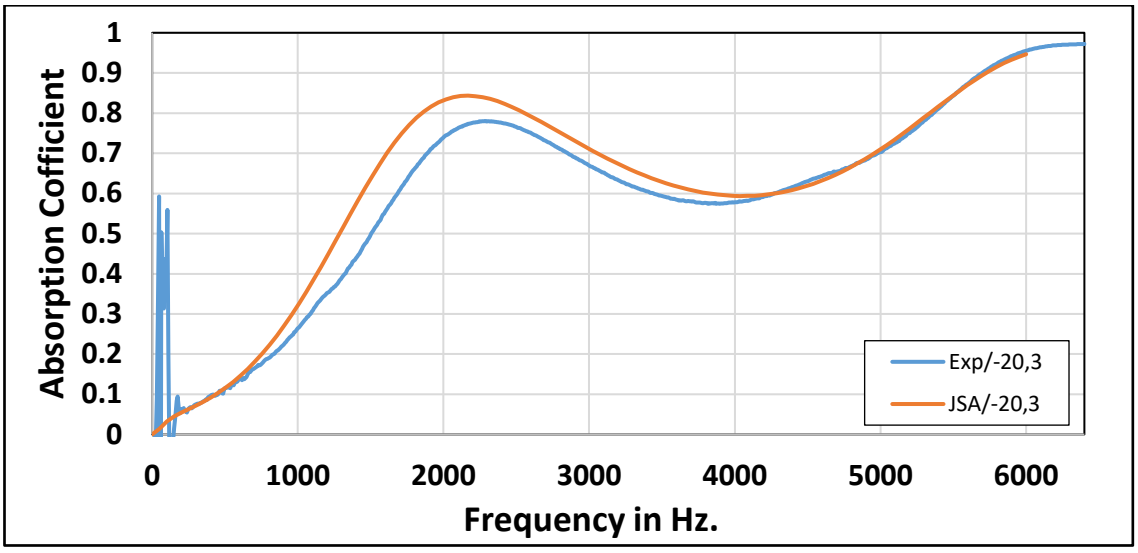

Figure B5- 3. The experimental and theoretical absorption curves of the 3rd 30 mm thickness slab of -20 in Hg vacuumed pressure sample.

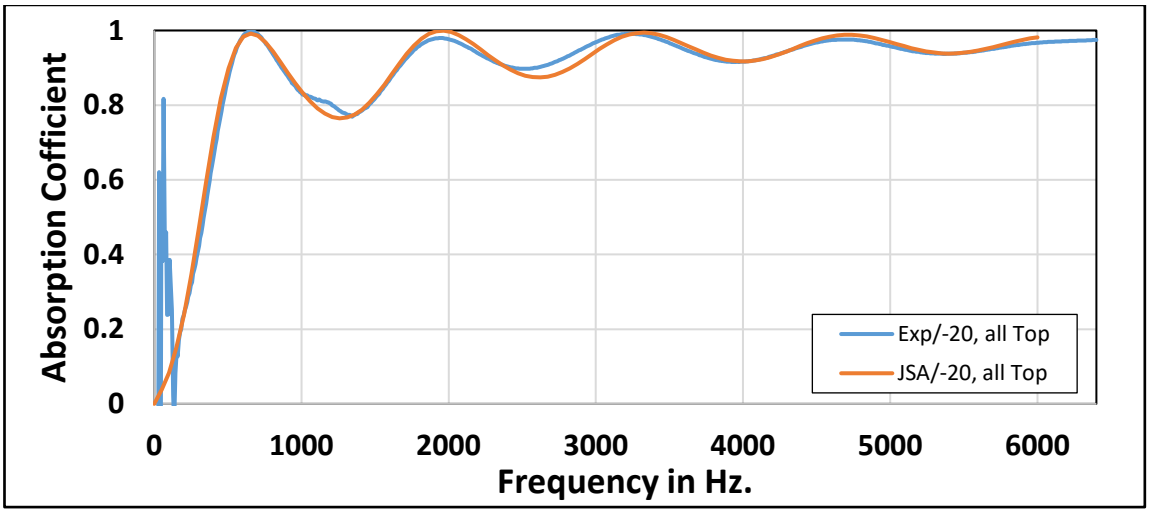

Figure B5- 4. The experimental and theoretical absorption curves of the 120 mm thickness of -20 in Hg vacuumed pressure sample, the direction of the wave with the same pores growing direction.

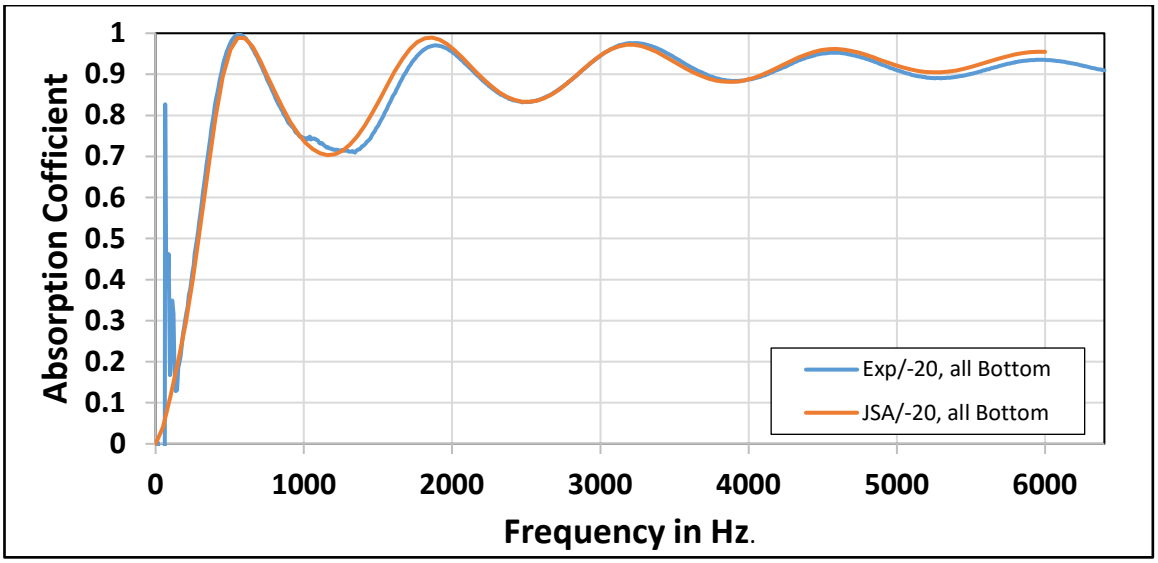

Figure B5- 5. The experimental and theoretical absorption curves of the 120 mm thickness of -20 in Hg vacuumed pressure sample, the direction of the wave with the obverse pores growing direction.

B6: These results of the -25 in Hg vacuumed insulation samples.

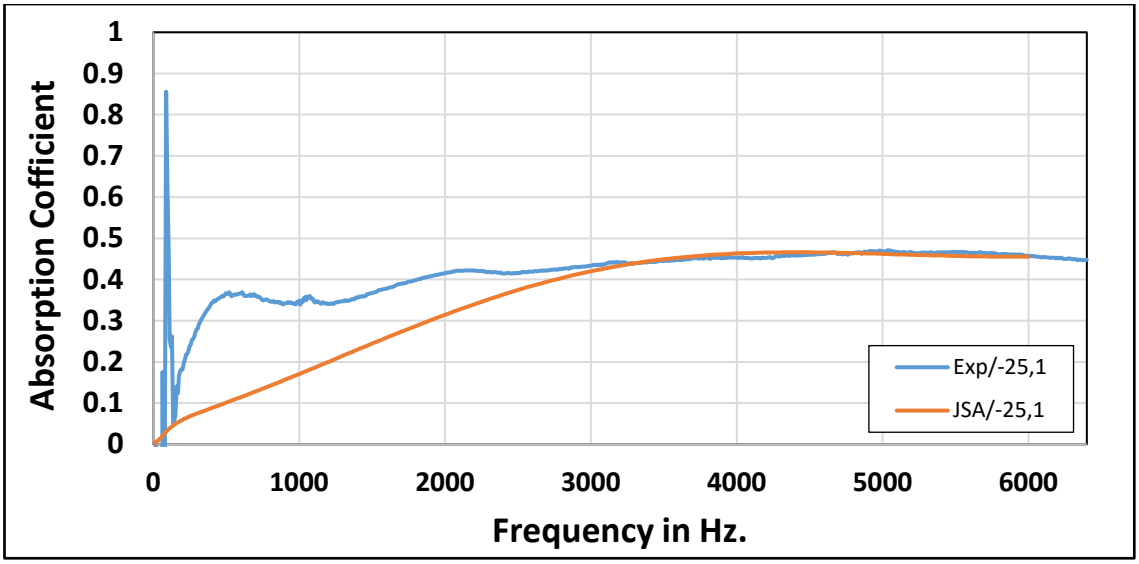

Figure B6- 1. The experimental and theoretical absorption curves of the 1st 30 mm thickness slab of -25 in Hg vacuumed pressure sample.

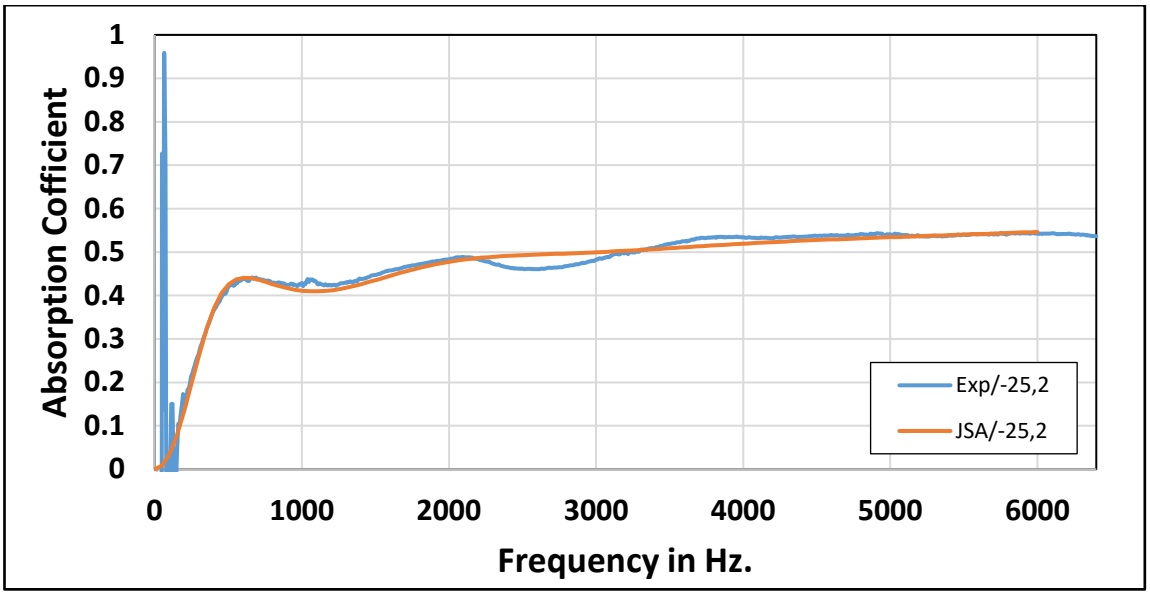

Figure B6- 2. The experimental and theoretical absorption curves of the 2nd 30 mm thickness slab of -25 in Hg vacuumed pressure sample.

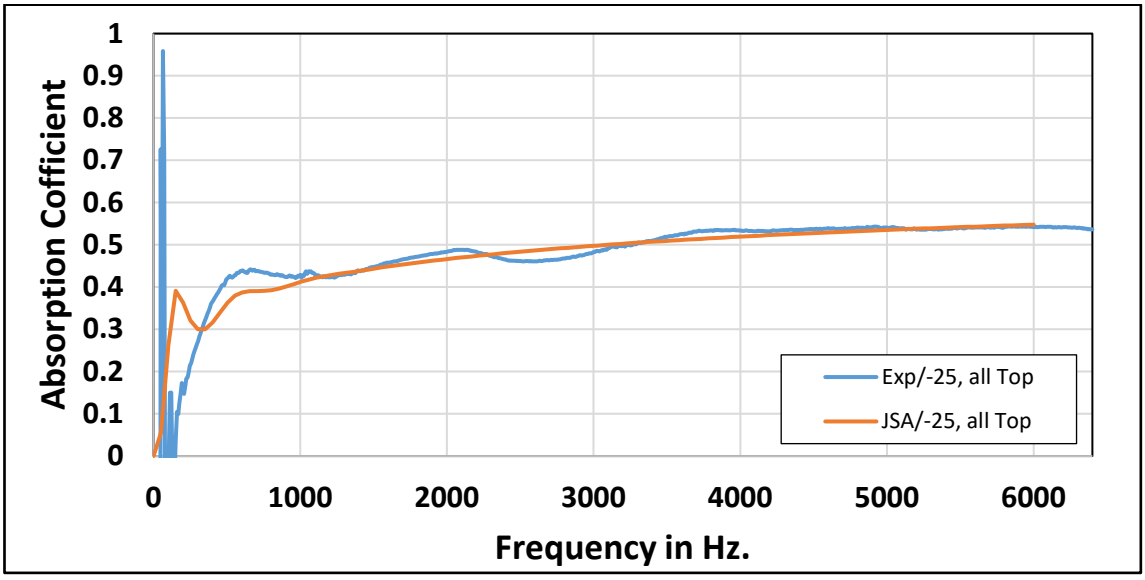

Figure B6- 3. The experimental and theoretical absorption curves of the 120 mm thickness of -25 in Hg vacuumed pressure sample, the direction of the wave with the same pores growing direction.

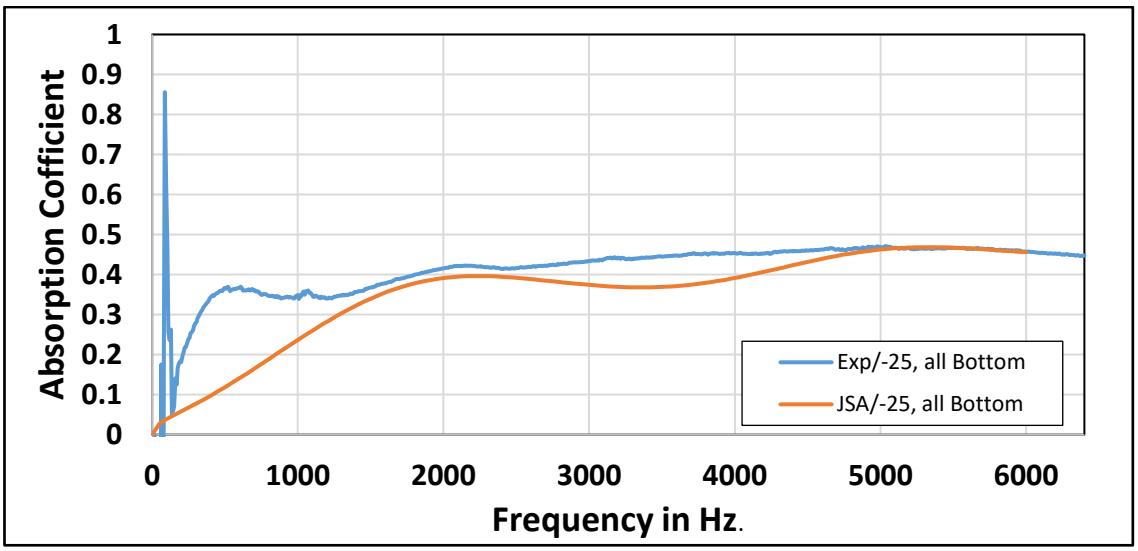

Figure B6- 4. The experimental and theoretical absorption curves of the 120 mm thickness of -25 in Hg vacuumed pressure sample, the direction of the wave with the obverse pores growing direction.

APPENDEX C

Steel _ Present in tables

Property	Name	Value	Unit
Density	rho	7850[kg...	kg/m³
Isotropic structural loss factor	eta_s	0	1
Young's modulus	E	160e9[Pa]	Pa
Poisson's ratio	nu	0.33	1

ArmaFlex

Property	Name	Value	Unit
Young's modulus	E	0.25e+6	Pa
Poisson's ratio	nu	0.3	1
Density	rho	84	kg/m³
Isotropic structural loss factor	eta_s	0.2	1

Armasound 240

Property	Name	Value	Unit
Density	rho	240	kg/m³
Young's modulus	E	1.97e+6	Pa
Poisson's ratio	nu	0.3	1
Isotropic structural loss factor	eta_s	0.2	1

Armacheck

Property	Name	Value	Unit
Young's modulus	E	0.5e+6	Pa
Poisson's ratio	nu	0.4	1
Density	rho	1610	kg/m³
Isotropic structural loss factor	eta_s	0.2	1

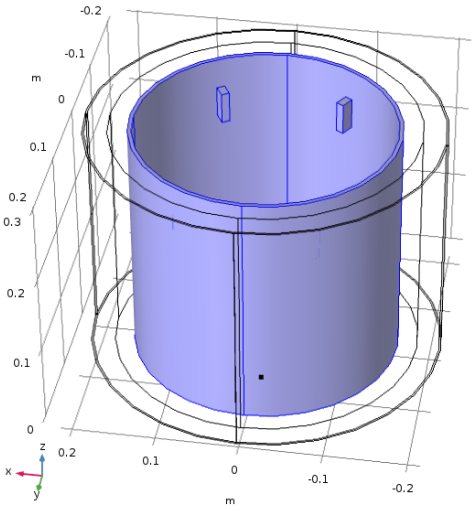

Structural steel

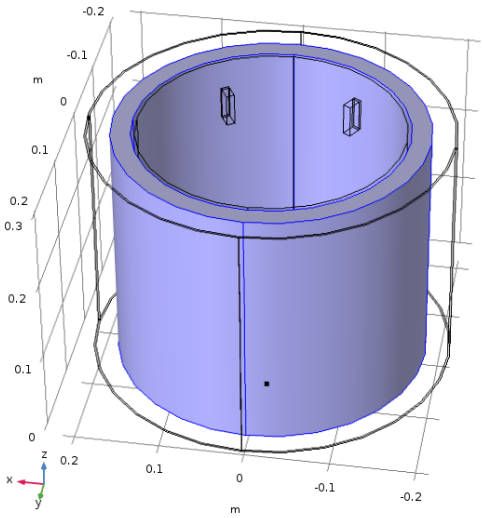

Armaflex

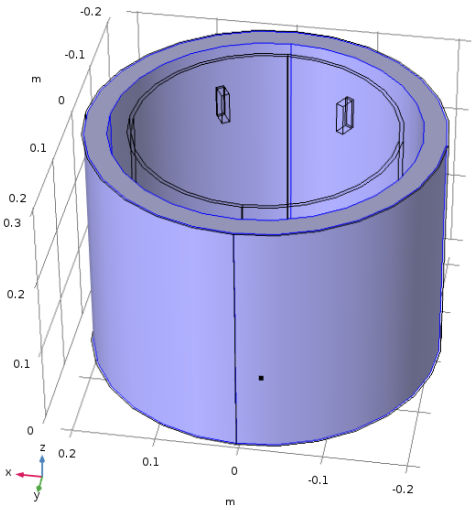

Armasound 240

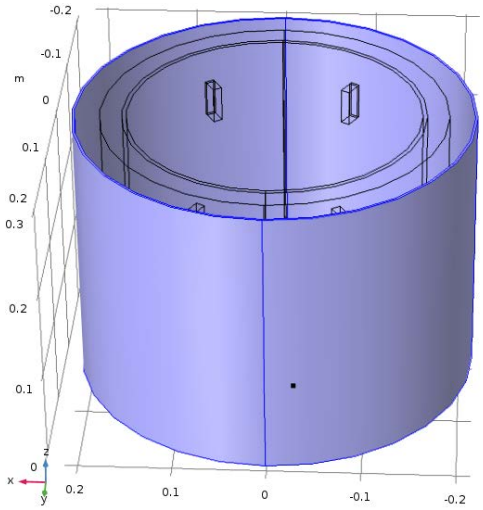

ArmaCheck

Figure C- 1. The cylinderical section of steel pipe and three diferent layers of system B insulation materials

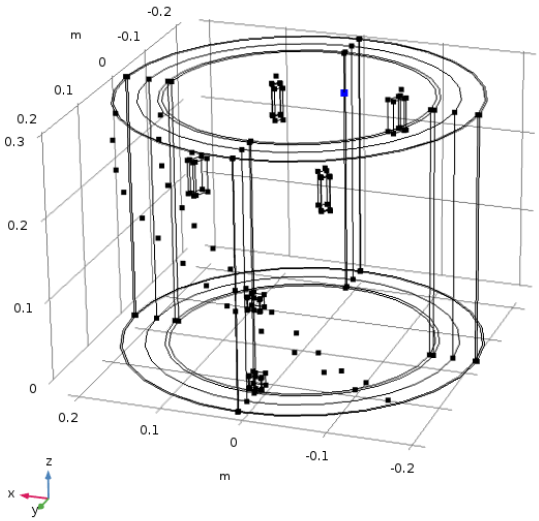

Load point (3N)

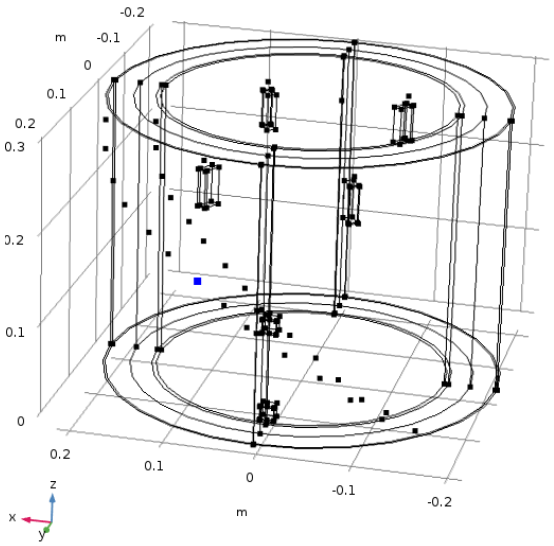

Receiver point (laser)

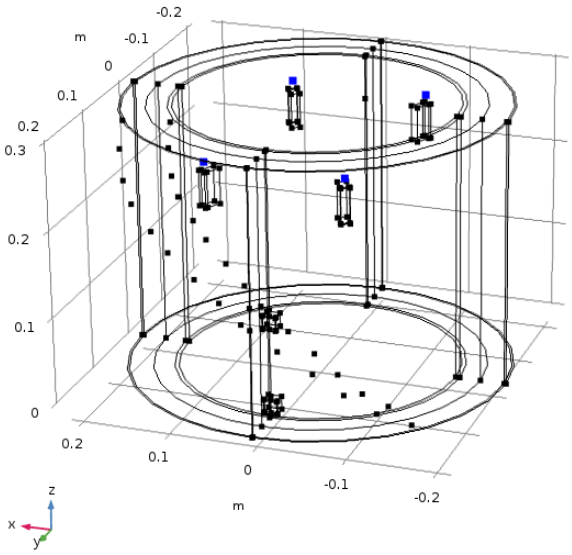

Spring foundations (4points)